

Electronic Thesis and Dissertation Repository

8-16-2021 10:00 AM

Inherently Porous Atomically Thin Membranes for Gas Separation


Harpreet Atwal, *The University of Western Ontario*

Supervisor: Boutilier, Michael S.H., *The University of Western Ontario*

A thesis submitted in partial fulfillment of the requirements for the Master of Engineering Science degree in Chemical and Biochemical Engineering

© Harpreet Atwal 2021

Follow this and additional works at: <https://ir.lib.uwo.ca/etd>

 Part of the [Membrane Science Commons](#), [Nanoscience and Nanotechnology Commons](#), [Polymer Science Commons](#), and the [Transport Phenomena Commons](#)

Recommended Citation

Atwal, Harpreet, "Inherently Porous Atomically Thin Membranes for Gas Separation" (2021). *Electronic Thesis and Dissertation Repository*. 8050.

<https://ir.lib.uwo.ca/etd/8050>

This Dissertation/Thesis is brought to you for free and open access by Scholarship@Western. It has been accepted for inclusion in Electronic Thesis and Dissertation Repository by an authorized administrator of Scholarship@Western. For more information, please contact wlsadmin@uwo.ca.

Abstract

Membranes made from atomically thin materials promise hundreds of times higher production rates than conventional polymer membranes for separation applications. Graphene is impermeable to gases but becomes selectively permeable once pores are introduced into it but creating trillions of nanopores over large areas is difficult. By instead choosing an inherently porous two-dimensional material with naturally identical pores repeated at high density, we may circumvent this challenge. In this work, I explored the potential of two candidate materials, 2D polyphenylene and graphdiyne. I synthesized cyclohexane-m-phenylene, a monomer of 2D polyphenylene. I then develop an atomic force microscopy technique for measuring the permeance of nanoscopic areas of materials and perform the first gas permeance measurements of graphdiyne and demonstrate molecular sieving. Efforts to scale-up employ continuum transport equations for simple modeling so I developed analytical approximations for the rate of mass transfer rate by advection-diffusion in creeping flow through an orifice plate.

Keywords

membranes for gas separation, two-dimensional materials, atomically thin materials, porous graphene, graphdiyne, molecular sieving, transport models

Summary for Lay Audience

Gas separation membranes are widely used in industrial applications for hydrogen separation, helium separation/recovery, acid gas treatment, oxygen enrichment, and much more. Current commercially available membranes require high temperatures or pressures to operate at their optimal conditions, which increases the cost of production. These membranes also suffer from a tradeoff between permeance (easy flow of the desired species through the membrane) and selectivity (ability to reject undesired species), which means that when a membrane is highly selective, the flow through the membrane is slow, and vice versa. In this work, I explore atomically thin two-dimensional materials as gas separation membranes that can not only reduce energy consumption and cost but also provide maximum achievable permeance with high selectivity. This is possible as materials like graphene are a single atom thick, and their thinness imposes minimal resistance to fluid flow enabling high production rates and resolving the major performance limitation of conventional polymer membranes. As they can support holes the size of smaller molecules, they act as a molecular sieve which allows smaller molecules to pass through while completely blocking larger molecules.

While there is a strong interest in graphene as a separation membrane material, the lattice structure is very densely packed and does not allow the passage of gases or liquids. Engineers need to use special methods to generate nanometer-scale pores in graphene sheets to make them selectively permeable. However, creating trillions of sub-nanometer holes for large-scale application has proven difficult. My project aims to develop atomically thin membranes that solve this problem by replacing the graphene layer with an intrinsically porous 2D polymer. Such materials naturally have a high density of sub-nanometer pores repeated exactly over their entire surface area, circumventing the pore creation challenge in graphene. In this work, I successfully synthesized a building block for porous graphene. I also developed a measurement setup that allowed the first experimental measurements of fluid flow through sub-nanometer pores of Graphdiyne (2D polymer). Furthermore, I developed correlations for simple transport modeling that did not exist before. This project is a major step towards developing macroscopic, selectively permeable 2D polyphenylene membranes for industrial applications.

Co-Authorship Statement

All chapters were written by Harpreet Atwal and were edited by Michael Boutilier.

All experimental work was conducted by Harpreet Atwal, except for making silicon wafers with pre-defined micrometer cavities, which were made by Anika Wong.

Acknowledgments

First and foremost, I would like to express my gratitude to Dr. Michael Boutilier for giving me the opportunity to join his group and take part in an exciting research project. I am eternally grateful for his support and mentorship throughout my graduate studies. Next, I would like to extend my appreciation to Dr. Johanna Blacquiere, who got me through the chemistry aspect of my research. I appreciate the time she took to help me out when the experiments became difficult.

A big thanks to Benjamin Bridge for being an amazing mentor and guiding me with my chemistry experiments (I will never forget the excitement and fear of working with t-BuLi). To all the Blacquiere group: Meagan, Kyle, Devon, Matt, and David, thank you for being so helpful. Much appreciation for Mat Williams for running a good NMR facility, Todd Simpson, and Tim Goldhawk for their support at the Nanofabrication facility.

I want to thank Anika Wong for being an incredible lab member/friend and sharing this crazy ride with me. Next, I must acknowledge Niles Lopez for his unwavering support throughout my studies and for being there for me on my good and bad days. Special thanks to Anthony Johnson, Vincent Kong, Lanting Qian, and Avneet Atwal for being so caring and checking up on me often. To my friends and family, thank you for all your love and encouragement.

Table of Contents

Abstract.....	ii
Summary for Lay Audience.....	iii
Co-Authorship Statement.....	iv
Acknowledgments.....	v
List of Tables	x
List of Figures	xi
List of Schemes.....	xvi
List of Appendices	xvii
List of Abbreviations	xviii
Chapter 1.....	1
1 Introduction.....	1
1.1 Commercially Available Gas-Separation Membranes.....	2
1.1.1 Polymers	3
1.1.2 Inorganic Membranes	4
1.1.3 Mixed-Matrix Membranes	5
1.1.4 Carbon Nanotubes as Membranes	7
1.2 Two-Dimensional-Material Membranes.....	7
1.2.1 Inorganic	9
1.2.2 Hybrid	11
1.2.3 Organic.....	12
1.2.4 Carbon.....	13
1.3 Intrinsically Porous Atomically Thin Membranes.....	15
1.3.1 Porous Graphene (2D Polyphenylene).....	15
1.3.2 Graphdiyne (Graphyne-2).....	17

1.4	Fundamentals of membrane-based gas separation.....	19
1.4.1	Permeance and Permeability.....	19
1.4.2	Selectivity	20
1.4.3	Transport Mechanisms.....	20
1.4.4	Gas Transport through Nanoporous Atomically Thin Membranes	21
1.5	Industrial Applications of Gas Separation Membranes	24
1.6	Thesis Goals and Objectives.....	25
1.7	References.....	27
	Chapter 2.....	33
2	General Experimental Techniques and Equipment.....	33
2.1	Organic synthesis	33
2.1.1	Glove Box and Schlenk Line	33
2.2	Methods of Characterization.....	34
2.2.1	Nuclear magnetic resonance (NMR) Spectroscopy and Mass Spectrometry (MS).....	34
2.2.2	Scanning electron microscopy (SEM)	35
2.2.3	Atomic Force Microscopy (AFM)	36
2.3	References.....	38
	Chapter 3.....	40
3	Developing 2D Polyphenylene Membranes	40
3.1	Introduction.....	40
3.2	Synthesis of Hexaiodo-substituted cyclohexa-m-phenylene (CHP).....	40
3.2.1	Synthesis of 1,3-dibromo-5-(trimethylsilyl)benzene	41
3.2.2	Synthesis of 1,3-diiodo-5-(trimethylsilyl)benzene	44
3.2.3	Synthesis of 3-bromo-5-(trimethylsilyl)phenylboronic acid	45

3.2.4	Synthesis of 5,3''-dibromo-3,5',5''-tris-trimethylsilyl-1,1';3',1''-terphenyl (m-terphenyl derivative)	47
3.2.5	Synthesis of 5,5',5'',5''',5''''',5''''''-hexatrimethylsilylhexa-m-phenylene	49
3.2.6	Synthesis of 5,5',5'',5''',5''''',5''''''-hexaiodohexa-m-phenylene	56
3.3	Discussion and Future Directions	59
3.4	References.....	62
Chapter 4	65
4	Developing Graphdiyne Membranes	65
4.1	Introduction.....	65
4.2	Centimeter-Scale GDY Membranes in a Flow Cell	66
4.2.1	Experimental Design and Methods.....	66
4.2.2	Results and Discussion	71
4.3	Single-Flake GDY Analysis using AFM	73
4.3.1	Experimental Design and Methods.....	74
4.3.2	Results and Discussion	81
4.4	Conclusion and Future Directions	87
4.5	References.....	89
Chapter 5	91
5	Mass Advection-Diffusion in Creeping Flow Through an Orifice Plate	91
5.1	Abstract.....	91
5.2	Introduction.....	91
5.2.1	Numerical Solution	97
5.2.2	Leading Order Solution.....	101
5.3	Non-Zero Thickness Orifice Plates.....	103
5.4	Computational Fluid Dynamics (CFD).....	104

5.4.1	ANSYS Fluent	104
5.4.2	OpenFOAM	106
5.5	Finite Volume Solution with Cylindrical Symmetry	109
5.5.1	Approximate Sherwood Number Expression	112
5.6	Conclusion	113
5.7	References	114
6	Conclusion and Future Directions.....	118
6.1	CHP synthesis	118
6.2	Molecular sieving through GDY	118
6.3	Mass advection-diffusion in creeping flow through an orifice plate	119
6.4	Closing	120
	Appendices.....	121
	Curriculum Vitae	130

List of Tables

Table 1.1: Synthesis methods, and characteristics of 2D graphdiyne and 2D polyphenylene nanosheets cited in literature.	19
Table 4.1: Selectivity values comparing the calculated Knudsen ratios with the obtained values for bare 10 nm PCTEM and GDY on 10 nm PCTEM. Numbers in orange are selectivity values lower than bare 10 nm PCTEM whereas blue are values higher than bare 10 nm PCTEM.	72
Table 4.2: Kinetic diameters ¹⁶ , calculated slope (volumetric flow rate), initial bulge volume and gas flow rate of each tested gas.	84
Table 5.1: Sh vs. Pe computed for a series expansion truncated after the $n = 20$ term. Pe is read from the first row and column and the Sh value is recorded in the corresponding cell of the table.	101
Table 5.2: Total flow rates obtained from the simulation for increasing grid refinement (# of finite volumes) and the calculated percent error with respect to the Sampson equation.	108

List of Figures

- Figure 1.1:** Classification of membranes based on their pore size, with the specified particles that are blocked by each membrane. Republished with permission of Royal Society of Chemistry, from Ref. [12]; permission conveyed through Copyright Clearance Center, Inc. 2
- Figure 1.2:** A typical hollow fiber membrane. Obtained from Ref. [16]..... 3
- Figure 1.3:** Graphical representation of selectivity and permeability for polymeric and inorganic membranes, and when combined to form a mixed-matrix membrane, complement one another to form a better membrane. Reproduced from Ref. [21]..... 5
- Figure 1.4:** Illustration of gas separation via mixed-matrix membrane, where polymer (light yellow) makes up the matrix and inorganic nanofillers (e.g., zeolites) are incorporated into this matrix. Reproduced with permission from Ref. [24]. Copyright 2019, American Chemical Society. 6
- Figure 1.5:** Examples of the various 2D nanosheet materials used for preparing gas separation membranes. Republished with permission of Royal Society of Chemistry from Ref. [28]; permission conveyed through Copyright Clearance Center, Inc..... 8
- Figure 1.6:** Structure of layered double hydroxide crystals, where the brucite-like layers are made up of stacked metal hydroxides and the water molecules along with compensating anions located in the interlayer gallery. Republished with permission of Royal Society of Chemistry from Ref. [28]; permission conveyed through Copyright Clearance Center, Inc..... 11
- Figure 1.7:** Schematic illustration of possible ways to prepare graphene, graphene oxide and reduced graphene oxide. Reprinted from Ref. [42], Copyright 2019, with permission from Elsevier..... 13
- Figure 1.8:** Scanning tunneling microscopy (STM) image of the synthesized 2D polyphenylene polymer network on a silver substrate, where the structure of the CHP backbone can be easily recognized. Republished with permission of Royal Society of Chemistry from Ref. [46]; permission conveyed through Copyright Clearance Center, Inc. 17
- Figure 1.9:** Illustration that highlights the difference between graphene, graphyne, and graphdiyne, which is simply the number of carbynes present between hexagonal benzene rings. Obtained from Ref. [55]..... 18
- Figure 1.10:** Various membrane transport mechanisms as the pore size of a membrane increases, where d_g is the gas molecular diameter, and λ is the gas mean free path. Relationships between Q (flux), D (diffusivity), S (sorption coefficient), m (molecular mass) and μ (viscosity) is provided as needed for the four transport mechanisms.

Reprinted by permission from Springer Nature and Copyright Clearance Center: Springer Nature, Nature Nanotechnology, Ref. [9], Copyright 2017..... 21

Figure 1.11: Illustrates the steric and activated regime mechanisms for gas transport. Reprinted by permission from Springer Nature and Copyright Clearance Center: Springer Nature, Nature Nanotechnology, Ref. [9], Copyright 2017..... 23

Figure 1.12: Pyramid illustration highlighting the expansion of applications in hydrogen energy. Obtained from Ref. [66]..... 25

Figure 2.1: A typical Schlenk line set-up. Image was obtained from Ref. [2]. 33

Figure 2.2: ^1H NMR spectrum for chloroethane, showing chemical shifts that correspond to the two proton signals. Note deshielding of protons near the electronegative chlorine atom. Reproduced from Ref. [6]. 34

Figure 2.3: (left) A schematic illustration of mass spectrometry. Obtained from Ref. [8] (right) Results obtained from a MS spectrum. Reprinted from Ref. [9], Copyright 1999, with permission from Elsevier. 35

Figure 2.4: a) Schematic illustration of SEM showing the origin of electron beam, backscatter, and secondary electron detector. Image was obtained from Ref [13]. b) Diagram of gallium ions milling the surface of a sample, and the production of secondary electrons which can be used for imaging. Reproduced from Ref. [13]. 36

Figure 2.5: AFM scanning setup showing the how the laser light travels from the light source, bounces off the AFM probe and then hits the photodiode. Reproduced from Ref. [15]. 37

Figure 3.1: (top) ^1H NMR spectra of **1** using procedure by Gong et al.¹¹, showing multiple impurities and minimal product **(bottom)** ^1H NMR spectra of purified **1** using a modified version of Ye et al.¹², where •• are signals from aryl group, • TMS protecting group and ★ chloroform solvent peak. 43

Figure 3.2: ^1H NMR spectra of purified **2**, signal indication: •• aryl group, • TMS protecting group and ★ dichloromethane solvent peak. 44

Figure 3.3: ^1H NMR spectra of cleaned **3**, signal indication: ••• aryl group, • boronic acid, • TMS protecting group and ★ acetone solvent peak. 46

Figure 3.4: Catalytic cycle for a general Suzuki cross-coupling reaction, which was used for the synthesis of the m-terphenyl derivative. Obtained from Ref. [18]. 48

Figure 3.5: A. ^1H NMR spectra of purified **4**, signal indication: ••• aryl group, ••TMS protecting group and ★ acetone solvent peak. B. and C. ^1H NMR spectra of undesired eluents obtained during column chromatography. 48

Figure 3.6: A. General reaction scheme for a Yamamoto coupling reaction used in the synthesis of hexatrimethylsilylhexa-m-phenylene. Republished with permission of Royal Society of Chemistry from Ref. [20]; permission conveyed through Copyright Clearance Center, Inc. B. Important intermediate steps in Yamamoto coupling, where Ph is a phenyl group. Reprinted from Ref. [21], Copyright 1992, with permission from Elsevier.	51
Figure 3.7: A. ¹ H NMR spectra in CDCl ₃ showing the formation of boronic acid species, signal indication • aryl group, ••TMS protecting group, • boronic acid, and ★ solvent. B. ¹ H NMR spectra in CD ₂ Cl ₂ after stirring overnight (less impurities) C. ¹ H NMR spectra in CD ₂ Cl ₂ after stirring for two days (more impurities).....	53
Figure 3.8: (top) ¹ H NMR spectra of the boronic ester species, signal indication ▲ water, ••TMS protecting group, and • boronic ester (bottom) ¹ H NMR spectra of boronic acid species, where • is boronic acid.	54
Figure 3.9: (top) ¹ H NMR spectra of the boronic ester species without molecular sieves, where the dashed line shows very little product formation. (bottom) ¹ H NMR spectra of the boronic ester species with molecular sieves, shows more product formation. Signal indication • boronic acid, and • boronic ester.	54
Figure 3.10: (top) ¹ H NMR spectra of the alternative synthesis route using Suzuki coupling. (bottom) ¹ H NMR spectra of the main synthesis route using Yamamoto coupling and the successful formation of 5. Signal indication •• aryl group, and • TMS protecting groups.	55
Figure 3.11: (top) SEM image of the particle analyzed. (bottom) Elemental spectrum obtained from the X-ray detector with the weight and atomic % values for each element present in the inset.	58
Figure 3.12: Schematic of the resistive thermal evaporation technique. Reprinted from Ref. [31], Copyright 2013, with permission from Elsevier.	60
Figure 3.13: Reaction mechanism for the formation of PPN sheets using TCB and Na spheres. Reprinted with permission from Ref. [33]. Copyright 2019, American Chemical Society.....	61
Figure 4.1: Measurement setup for gas flow through Graphdiyne (yellow), which covers a 10 nm-diameter hole in inflated graphene (grey) over a cavity in a silicon wafer (blue).	66
Figure 4.2: A. Chemical structure of GDY. Reprinted with permission from Ref. [4]. Copyright 2018, Taylor & Francis. B. SEM image of GDY powder on a silicon wafer..	67
Figure 4.3: SEM image of GDY flakes and tape residue on copper foil.	68
Figure 4.4: Frequency of various GDY flake sizes seen on a silicon wafer via AFM after GDY ultrasonication treatment, with the highest being in the 10-25 nm range.	69

Figure 4.5: Diagram of the flow cell. Created by Samuel Gomez Suarez. 1. The membrane holder. 2. and 3. Pressure transducers that display absolute pressure upstream and downstream the membrane. 4. Cylinder (volume of 150 mL). 5. Holds the flow cell in place. 6. Valve that reduces the downstream volume. 7. And 8. Valves connected to the vacuum pump. 9. Vacuum pump. 10. Gas cylinders. 11. Valve connected to the gas supply.....	70
Figure 4.6: Measured permeance for bare 10 nm PCTEM (blank) vs. molecular weight for He, Ar, N ₂ , CH ₄ and SF ₆	71
Figure 4.7: Measured permeance for GDY on 10 nm PCTEM vs. molecular weight for He, Ar, N ₂ , CH ₄ and SF ₆	71
Figure 4.8: Normalized permeance (GDY Permeance/Blank Permeance) vs. molecular weight for He, Ar, N ₂ , CH ₄ and SF ₆	72
Figure 4.9: SEM image of PMMA-supported Graphene layers on silicon wafer.	75
Figure 4.10: SEM image of PMMA-free graphene layers on silicon wafer.....	76
Figure 4.11: A. SEM image of four-layered graphene on a silicon wafer with six pre-defined 5 μm cavities. B. SEM image of a 10 nm hole in graphene on a 5 μm cavity in the silicon wafer.....	78
Figure 4.12: AFM images of an inflated membrane (top) 3D surface plots. (bottom) Height, Amplitude, Phase and Z-sensor retrace.....	79
Figure 4.13: SEM images obtained at 1 kV of the silicon wafer after GDY deposition A. Pore D15. B. Graphene-dense area of interest (hard to see GDY) C. D. and E. Thin graphene coverage with visible GDY flakes (white arrow).....	80
Figure 4.14: 3D surface plots (obtained from AFM) of the burst membrane.....	81
Figure 4.15: Membrane deflation data for a 3-layered graphene stack over time with measured height profiles inset.	82
Figure 4.16: Gas deflation data obtained after charging the fabricated membrane with various gases. Note that air (100 kPa) and CH ₄ (20 kPa) are from different pores while SF ₆ and N ₂ (both at 20 kPa) are from the same pore, D15.	84
Figure 4.17: Measured gas flow rates through GDY. Arrows indicate that the markers are the lower bound, as the permeance was above the resolvable range.	84
Figure 5.1: Atomically thin membranes. a. Illustration of water and solute molecules in the vicinity of a ~1 nm graphene pore. b. and c. Scanning electron micrograph showing ~ 30 nm pores in few-layer graphene. Pores indicated with white arrows. Images were obtained with a Zeiss LEO 1530 field emission scanning electron microscope at 1 kV	

accelerating voltage. **d.** Hole in an infinitesimally thick plate with cylindrical and oblate-spheroidal coordinates shown. 93

Figure 5.2: Concentration field computed numerically by truncating the series expansion after the $n = 20$ term. **a** Concentration field for various Péclet numbers. **b** Concentration profiles along the z axis. 98

Figure 5.3: Expansion coefficients and convergence. **a** Calculated expansion coefficient plotted along the z axis for the first 4 terms in the series expansion truncated after the $n = 20$ term. **b** Maximum absolute value of each expansion coefficient over all r and z for different Péclet numbers, showing the diminishing contribution of higher order terms. . 99

Figure 5.4: Sherwood number dependence on Péclet number of an infinitesimally thick orifice plate. Markers show numerical calculation for a series expansion truncated after the $n = 20$ term. Solid curve shows the analytical approximation obtained by truncating the series expansion to one term (Eq. 5.18). The dotted lines show the three cases that represent the approximate expression. 102

Figure 5.5: Mass transfer rate through an orifice plate of non-zero thickness. **a** Mean flow rate vs. aspect ratio computed by finite volume simulations (markers) compared to the approximate expression of Dagan et al.²⁸ (Eq. 5.19, solid curve). Inset shows a sketch of the orifice plate geometry. **b** Sherwood number dependence on Péclet number for various hole aspect ratios. Markers show finite volume simulation results whereas curves show the approximate fit from Eq. 5.22 for the same aspect ratios. 103

Figure 5.6: Ansys Fluent **a.** Geometry (wireframe mode) of the system consisting of inlet, outlet, and planar interface. **b.** Meshed geometry **c.** Meshed geometry with outlet removed. 105

Figure 5.7: A quiver plot (MATLAB) of velocity field in the r and z direction as obtained from ANSYS. 106

Figure 5.8: Drawing of cross-section in the plane of the wall showing the different regions of the mesh that can be refined non-uniformly. 108

Figure 5.9: Paraview images of the meshed geometry. **i.** Featured edges **ii.** Meshed surface **iii.** Wireframe. 109

Figure 5.10: Flow fields and concentration fields from finite volume simulations for non-zero thickness plates of various aspect ratios. **a** Local flow speed ($|v|$) normalized by average flow speed through the pore. Solid curves show streamlines. **b** Concentration field. 111

Figure 5.11: Dimensions and coordinate system definition for advection-diffusion in a long pipe. 113

List of Schemes

- Scheme 1:** Synthesis of hexaiodo-substituted cyclohexa-m-phenylene (CHP). 41
- Scheme 2:** Alternate reaction scheme to synthesize hexatrimethylsilylhexas-m-phenylene by converting some of 4 to a boronic ester and then cross-coupling the two. 52
- Scheme 3:** Silver-promoted aryl-aryl coupling of iodobenzene to biphenyl. Republished with permission of Royal Society of Chemistry from Ref. [1]; permission conveyed through Copyright Clearance Center, Inc. 59

List of Appendices

Appendix 1: Schlenk line setup for the first reaction.	121
Appendix 2: (left) Undesired brown oil formation during the first reaction. (right) Rotovap setup.....	121
Appendix 3: (left) Separation of impurity from the desired product after 24 hr in the fridge. (middle and right) Desired product 1 with white needle-like crystals.....	122
Appendix 4: Desired product 2 (yellow crystalline material) after silica column.....	122
Appendix 5: (left) Synthesis of 3 prior to workup. (right) White amorphous solid 3 after workup.	122
Appendix 6: A. Synthesis of 4 after addition of the Pd catalyst (yellow) B. Colorless solid 4 after workup C. Degassing setup (bubbling with argon gas) and pressure release via the blue needle	123
Appendix 7: A. Synthesis setup for 5 where aluminum foil ensures absence of light. B. Thin Layer Chromatography (TLC) plate of the product showing two additional impurities. C. Isolation of the desired product using column chromatography.....	123
Appendix 8: Synthesis setup for 6 in a glove box - covered with black tape to ensure absence of light.	123
Appendix 9: Copyright Licenses	124

List of Abbreviations

$(\text{CD}_3)_2\text{CO}$	Deuterated acetone
^{13}C	Carbon
^1H	Proton
AFM	Atomic force microscopy
APS	Ammonium persulfate etchant
BPY	2,2'-bipyridine
CD_2Cl_2	Deuterated dichloromethane
CDCl_3	Deuterated chloroform
CFC	Closed fluid cell
CFD	Computational fluid dynamics
CHP	Cyclohexa-m-phenylene
CNTs	Carbon nanotubes
Cod	1,5-cyclooctadiene
COF	Covalent organic framework
CV	Control volume
DFT	Density functional theory
DI	Distilled water
EDS or EDX	Energy dispersive x-ray spectroscopy
FIB	Focused ion beam

GDY	Graphdiyne
GO	Graphene oxide
GS	Gas separation
HCl	Hydrochloric acid
IE	Ion-exchange
IPA	Isopropanol
KD	Kinetic diameter
LDH	Layered double hydroxides
Li_2SiF_6	Lithium hexafluorosilicate
M/Z	Mass-to-charge
MD	Molecular dynamics
MF	Microfiltration
MMM	Mixed-matrix membrane
MOF	Metal-organic framework
MS	Mass spectrometry
MW	Molecular weight
MWNT	Multiwalled carbon nanotubes
N-BuLi	N-butyllithium
$\text{Ni}(\text{cod})_2$	bis(cyclooctadiene)nickel (0)
NMR	Nuclear magnetic resonance

OpenFOAM	Open-source field operation and manipulation
PC	Polycarbonate
PCTEM	Polycarbonate track etch membrane
Pd	Palladium
PDMS	Polydimethylsiloxane
Pe	Peclet
PI	Polyimide
PIMs	Polymers with intrinsic porosity
PMMA	Poly (methyl methacrylate)
PPNs	2D polyphenylene networks
RO	Reverse Osmosis
SEM	Scanning electron microscopy
SF ₆	Sulfur hexafluoride
Sh	Sherwood number
Si	Silicon
SWNT	Single-walled carbon nanotube
T-BuLi	T-butyllithium
TCB	Trichlorobenzene
TMD	Transition metal dichalcogenides
TMS	Trimethylsilyl

UF Ultrafiltration

X Halogen

Chapter 1

1 Introduction

Separation converts a mixture into two or more product mixtures, where at least one of the resulting products is enriched or purified. The process utilizes differences in chemical or physical properties (such as size, mass, or chemical affinity) between the constituents of the mixture¹. Some major separation techniques include chromatography, distillation, evaporation, and filtration². Membranes then emerged as a means for separation – separating materials via pores or gaps in a molecular structure where the pore size determines the degree of selectivity³. Depending on the pore size, the membranes may be classified as Ultrafiltration (UF), Microfiltration (MF)⁴, Ion-exchange (IE), or Reverse Osmosis (RO)⁵ as shown in Fig 1.1. Separation in membranes is driven by gradients in pressure, concentration, temperature, or electric potential. They are a great option for separation as they offer easy operation, low maintenance, scalability, high selectivity, and energy efficiency^{6,7}. Therefore, they have applications in water, food, chemical processing, and the medical sector, with some major applications in water desalination and natural gas purification⁸. An ideal membrane allows easy flow of the desired species (high permeance) and rejects undesired species (high selectivity) while being easy to produce, exhibiting high thermal stability, having high chemical/mechanical strength, and being resistant to fouling^{6,7,9}.

Though membrane technology has seen remarkable progress, certain challenges remain – for example, the trade-off between selectivity and permeability; fouling control and mitigation; and operation under harsh conditions⁹. To overcome these challenges, scientists have explored a variety of membrane structures and materials such as polymers (e.g., polyethylene), inorganic (e.g., silica), nanomaterials (e.g., carbon nanotubes), and polymer-inorganic ‘mixed matrix membranes’¹⁰. These materials can utilize favorable membrane structures, have anti-fouling properties, or intrinsic porosity that provide high permeability and selectivity that may pave the way for the future of separation technology^{9,11}.

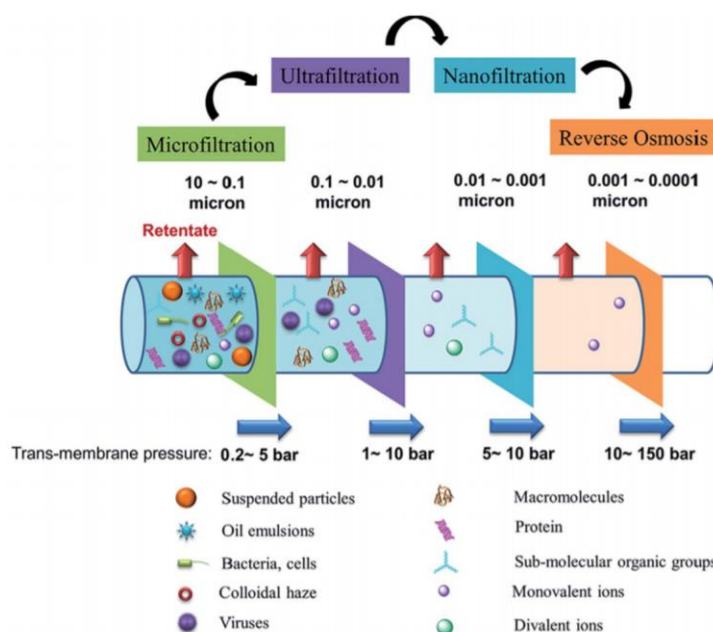


Figure 1.1: Classification of membranes based on their pore size, with the specified particles that are blocked by each membrane. Republished with permission of Royal Society of Chemistry, from Ref. [12]; permission conveyed through Copyright Clearance Center, Inc.

1.1 Commercially Available Gas-Separation Membranes

Though over 40 years old, the membrane gas separation (GS) industry proceeds to grow at a significant rate, accelerating the development of highly selective and permeable membranes. Membrane GS is a pressure-driven process with major applications in hydrogen recovery, oxygen enrichment, and carbon-dioxide (CO₂) removal¹¹. The first-ever industrial membrane GS system, known as Monsanto's Prism gas separator, was built during the 1980s. The Prism unit was developed to extract hydrogen from waste gas streams from refineries and petroleum plants, saving hydrogen and allowing it to be recycled for other use¹³. Membrane-based separations are an attractive option in GS applications as the process does not require heat-saving 90% of the cost associated with heat generation in processes like distillation and absorption. Other advantages of membrane GS include a smaller environmental footprint, simplicity in having no moving parts, and continuous operation^{6,11}. This section reviews the main membranes that have been used for years, as well as ongoing research involving new materials and membrane structures for enhanced performance.

1.1.1 Polymers

Most of the membranes employed commercially are polymeric, where a solution permeates the membrane via the solution-diffusion transport mechanism¹¹. In the solution-diffusion model, the permeant dissolves in the membrane material, diffuses across, and then desorbs from the membrane. This model is applied to transport in dense membranes with no natural pores. One of the important features of polymers is their “spinnability”, the ability to be made into hollow fiber membranes (Fig. 1.2) – where each hollow module consists of thousands of fibers¹⁴. This is important for scalability and cost-efficiency as the high membrane area to module volume ratio results in high productivity per unit volume. Unfortunately, polymer membranes cannot endure high temperatures (>250 °C) or aggressive chemical environments. Also, many of these polymers swell when exposed to even low amounts of hydrocarbons or carbon-dioxide with high partial pressure, resulting in membrane damage beyond repair. For these reasons, pre-treatment selection and condensate handling are important decision factors necessary for proper operation of membranes of this kind. When compared to other porous materials, polymeric membranes offer high selectivity and low throughput due to their low free volume while still experiencing the same trade-off limit between permeance and selectivity¹⁵.

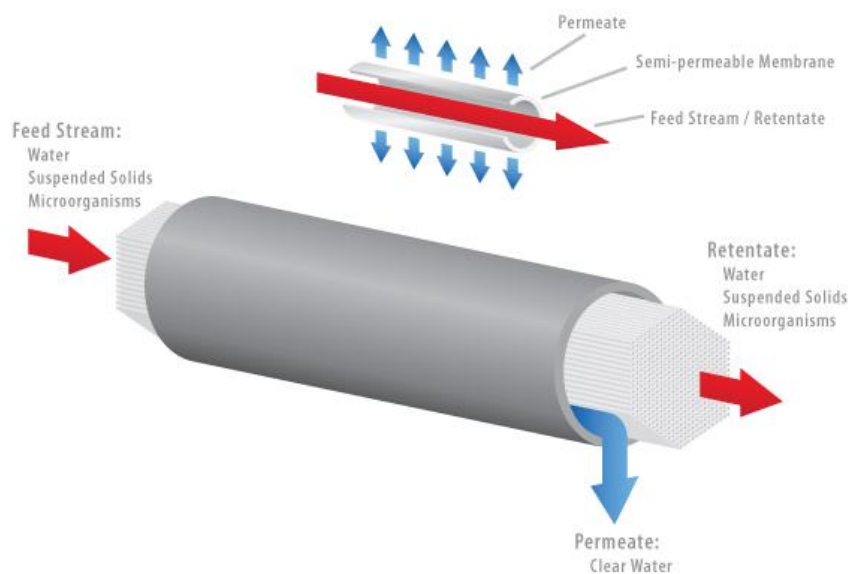


Figure 1.2: A typical hollow fiber membrane. Obtained from Ref. [16].

For GS membranes, the main polymers used are classified as either rubbery or glassy. Rubbery polymers are amorphous polymers kept above their glass transition temperature (T_g), whereas glassy polymers form when the temperature is below T_g . There is a relatively large free-volume above T_g caused by voids between highly mobile polymer chains, while below T_g , the free-volume decreases resulting in inadequate space for large-scale movement of the polymer backbone¹¹.

Rubbery polymers have high permeability, and their selectivity depends on the difference in the condensability of gas species. For example, polydimethylsiloxane (PDMS) has high permeability and high selectivity for condensable gases making it an attractive option for vapor separation¹⁷. Glassy polymers offer high gas selectivity and good mechanical properties where permeance depends on molecular diameter – lower diameter is more permeable. However, glassy polymers normally have a lower fraction of free volume than rubbery polymers. To function as membranes, medium to high free volume polymers (e.g., polyimides) must be used because the voids are needed to transport gas or liquid¹⁸. Both polymer categories have their advantages and thus have been in the industry for decades, yet the search for an ideal membrane goes on.

Recently, synthesized polymers with intrinsic microporosity (PIMs) have been developed by making a backbone with no conformational freedom while preventing effective packing¹⁹. PIMs represent a new class of microporous material (pore sizes smaller than 2nm) generated by polymer chemistry to offer good solubility, easy processability, and control over surface functionalities and properties. PIMs have pores large enough for gas molecules to pass through by Knudsen or surface diffusion (discussed in depth in section 1.4) rather than solution-diffusion, providing high permeability. They are reported to have competitive permeance and selectivity to commercial CO_2/CH_4 separation membranes^{11,19}.

1.1.2 Inorganic Membranes

Inorganic membranes (e.g., zeolites, silica, carbon) can endure high temperatures, withstand aggressive chemicals, and have outstanding mechanical robustness over their polymeric counterparts¹¹. However, they are not as readily used in the industry because of their downsides, which include brittleness, low membrane area to module volume ratio,

high manufacturing cost (about 100-1000 times greater than polymeric membranes), low permeability for highly selective dense membranes (e.g., metal oxides), and difficulty sealing at temperatures above 600°C. Inorganic membranes can be categorized into porous and non-porous – otherwise known as dense – inorganic membranes, where dense membranes are primarily applied for selective separation of hydrogen and oxygen²⁰. At present, interest and exploration in inorganic membranes continue to grow since they offer not only better selectivity but also thermal and chemical stability. The focus is on silica, zeolites, and carbon materials as they display molecular sieving properties, which is desirable for gas separation applications^{11,20}. Challenges faced by polymeric and inorganic membranes can be addressed successfully to some degree via mixed-matrix membranes that incorporate inorganic materials into a polymeric matrix.

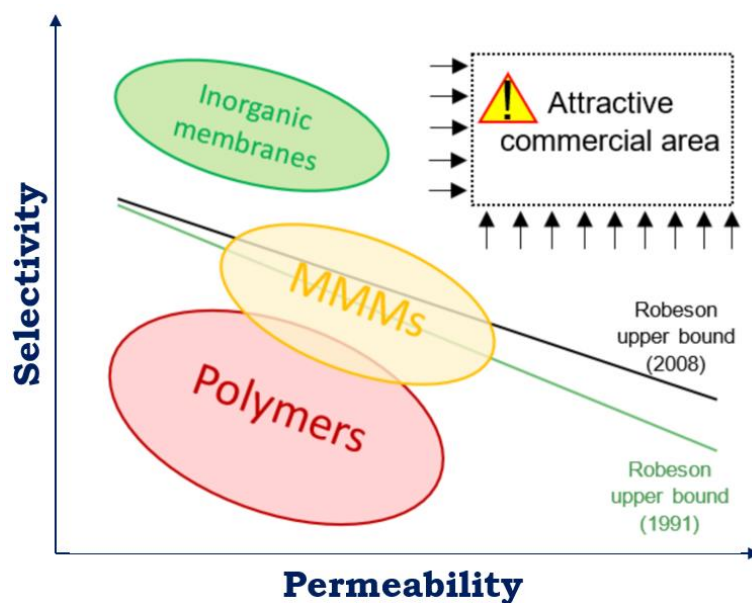


Figure 1.3: Graphical representation of selectivity and permeability for polymeric and inorganic membranes, and when combined to form a mixed-matrix membrane, complement one another to form a better membrane. Reproduced from Ref. [21].

1.1.3 Mixed-Matrix Membranes

Mixed-matrix membranes (MMMs) are a recognized route to enhance individual material properties of inorganic and polymeric membranes²². In their design, inorganic materials are incorporated into a polymer matrix in the form of microparticles or nanoparticles (Fig. 1.4). As fabrication methods for large-surface area polymeric membranes already exist,

adding an inorganic component is an easy modification. In principle, MMMs offer an economic advantage over inorganic membranes while possessing improved thermal and mechanical properties – stabilizing the polymer under high-temperature conditions and in aggressive chemical environments^{11,22}. To successfully fabricate MMMs, it is important to eliminate interfacial defects between the two phases and ensure compatibility between the nanoparticles and the polymer matrix. Other factors include filler concentration, shape, and dimensions. To this end, Koros et al.²³ proposed a criterion for material selection and preparation to prepare high-performance MMMs. The two key requirements proposed in addition to matching sieve polymer transport properties include molecular adsorption of polymer onto the sieve surface and polymer flexibility during membrane formation.

Since then, many MMMs have been designed and patented, showing that these membranes can enhance flux and selectivity. This improved efficacy is commonly used in CO₂/CH₄ and propylene/propane gas separations. However, some challenges with using MMMs still exist and include control of dispersion of nanoparticles between the matrix (which causes the formation of non-selective voids) and the incompatibility between nanoparticles and the matrix. These issues have to be resolved to improve the long-term stability and selectivity of MMMs^{11,22}.

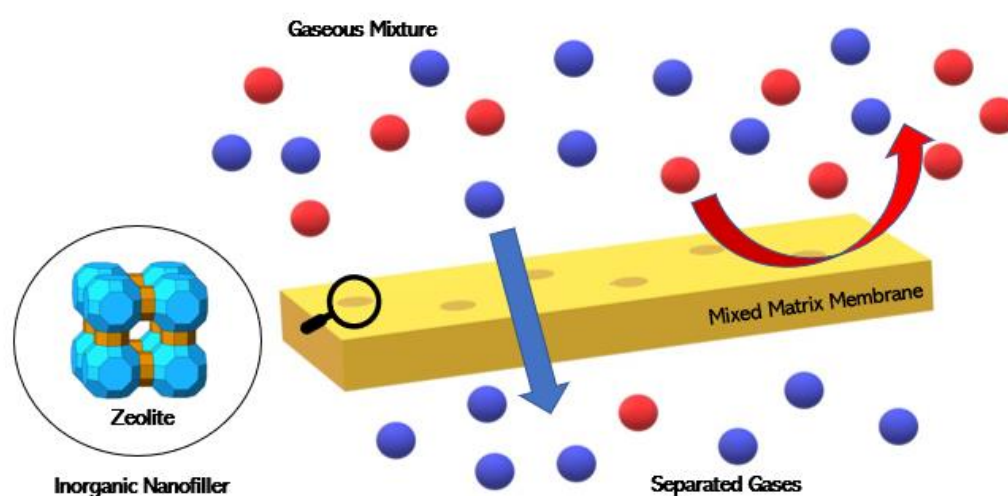


Figure 1.4: Illustration of gas separation via mixed-matrix membrane, where polymer (light yellow) makes up the matrix and inorganic nanofillers (e.g., zeolites) are incorporated into this matrix. Reproduced with permission from Ref. [24]. Copyright 2019, American Chemical Society.

1.1.4 Carbon Nanotubes as Membranes

In recent years, there has been an interest in the advancement of separation membranes made from 1D materials - inorganic nanotubes like boron nitride nanotubes, silicon carbide nanotubes, and carbon nanotubes (CNTs). These materials were initially integrated as additives that can improve selectivity, mechanical strength, and fouling resistance in polymeric membranes as they present a large surface area, tunable chemistry, and an interconnected open pore structure¹¹.

The possibility of using CNTs as membranes arose from molecular dynamics (MD) simulations that predicted that gas transport inside a single-walled carbon nanotube (SWNT), with a diameter of 1nm, was orders of magnitude faster than any other known materials with nanometer-scale pores²⁵. Their uniqueness stems from atomic-scale pores, the high rigidity of the graphene plane, and the non-polar sp^2 carbon network. Multiwalled carbon nanotubes (MWNT) with diameters of 6-7nm have also been verified to transport liquids orders of magnitude faster than can be accounted for by no-slip hydrodynamics^{11,25}. Despite their extremely fast transport of both gas and water, selectivity remains a challenge. Moreover, they are not suitably cost-effective for large-scale applications yet. More research is needed to improve the efficiency of CNT separation membranes²⁵.

1.2 Two-Dimensional-Material Membranes

The discovery of graphene in 2004 directed a great deal of attention towards two-dimensional (2D) materials as a brand-new approach to controlling mass transport. They have been widely explored as separation technologies, owing to the atomic thickness that allows them to be the thinnest possible barrier^{26,27}. In principle, the atomic thickness enables 2D material membranes to have minimal transport resistance and maximum permeation. They can also sustain nanoscale pores in their rigid lattice, allowing selectivity based on molecular size to transport both liquids and gases. Moreover, they display high mechanical strength and chemical robustness, making them ideal membranes tailored to many separation applications^{27,28}. In recent years, various 2D materials have been explored, where the primary classes based on their composition are inorganics (e.g., MXenes, zeolites, layered double hydroxide, and transition metal dichalcogenides), organics (e.g.,

covalent organic framework), carbon (e.g., graphene and graphene oxide), and hybrid (e.g., metal-organic framework)²⁸. In general, fabricated nanosheet membranes used for selective permeation contain a monolayer or a few layers of 2D material that have intrinsically uniform pores (e.g., zeolites) or created pores (e.g., graphene). On the contrary, laminar membranes are formed by putting together 2D material nanosheets such as graphene oxide into laminates with nm/sub-nm interlayer galleries that are used to permit molecular passage²⁸. In this section, each of the different classes of 2D membrane materials and their properties will be discussed in-depth, including the challenges of impeding commercialization.

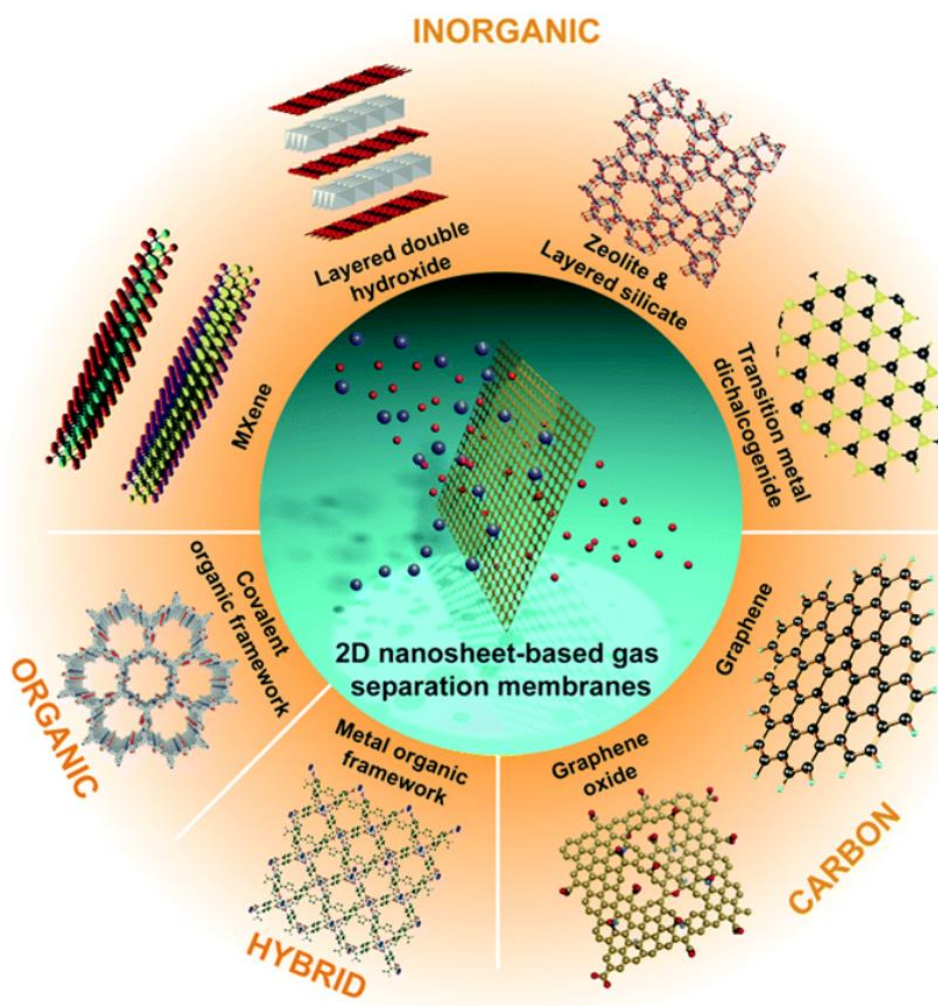


Figure 1.5: Examples of the various 2D nanosheet materials used for preparing gas separation membranes. Republished with permission of Royal Society of Chemistry from Ref. [28]; permission conveyed through Copyright Clearance Center, Inc.

1.2.1 Inorganic

Inorganic materials are the most ideal candidates for gas separation under harsh conditions as they have high thermal and chemical stabilities. Zeolites are one of the most studied inorganic materials, and the newly emerging nanosheets like MXene also make promising candidates for membranes in gas separation^{27,28}.

Zeolites

Zeolites are microporous aluminosilicate minerals that have been widely used in catalysis, commercial adsorption, and separation industries due to their molecular selectivity and high hydrothermal stability^{29,30}. However, the only zeolites that have been commercialized are LTA (Linde Type A), and these hardly display high selectivity due to their inter-crystal pores that form intrinsically in zeolite membranes. With this in mind, fabricating 2D zeolite nanosheets (pore size of 0.25 to 1 nm) can minimize these inter-crystal pores while maintaining their high selectivity and permeation flux via stacking nanosheets to make an ultra-thin molecular sieve membrane. Fabrication of 2D zeolite membranes depends on the availability of a stable suspension of zeolite nanosheets with a uniform thickness free of any unstructured and non-exfoliated contaminants^{27,29}. In addition, further development of deposition techniques is required for the quantitative transfer of suspended zeolite nanosheets onto porous substrates. In recent years, high-purity 2D MFI nanosheets were fabricated and contain 10-member ring pores inside as well as through the layers to provide shape-selective diffusion³⁰. However, these nanosheets have non-selective gaps, which can be reduced by mild secondary solvothermal growth. It is important to note that current 2D zeolite membranes are ~100 nm thick, 10 times thinner than 3D zeolite membranes, but thicker than the emerging graphene-based membranes. However, these membranes are not used in commercial gas separation applications due to their cost of synthesis and low yields of high-quality nanosheets³¹. Nevertheless, zeolites can be readily incorporated into a polymer matrix to form mixed matrix membranes^{28,30,31}.

Transition metal dichalcogenides (TMDs)

Two-dimensional TMDs, also known as 2D MX_2 – where M is a transition metal from group IV, V, or VI (e.g., Titanium) and X is a chalcogen (e.g., Sulfur) – have been widely used in catalysis and energy storage; however, reports on gas separation are rare^{27,32}. They are nonporous materials as the bulk TMD structure consists of X-M-X, where the chalcogens in the hexagonal planes are separated by a plane formed by metal atoms (Fig. 1.5). Therefore, separation can only occur in the channels of adjacent layers and because these layers are weakly held, obtaining atomic thickness becomes easier³³. Despite progress in TMD synthesis of fewer layers, they are not used in gas separation due to greater advancements in graphene and graphene oxide, which is easier to prepare and offers better performance.

MXene and layered double hydroxides (LDHs)

First discovered in 2011, MXenes are ceramics (one of the largest family of 2D materials), and they include transition metals (e.g., Ti_3), nitride (e.g., Ti_4N_3), and carbonitrides (e.g., Ti_3CN). They have already presented their applications in energy storage, medicine, and optoelectronics^{28,34}. Unlike zeolites and TMDs, MXenes can only be obtained by exfoliating their bulk phase MAX, which can be expressed as $\text{M}_{n+1}\text{AX}_n$ – where M is a d-block transition metal, A is a sp element mostly from group IIIA or IVA, and C is either carbon or nitrogen. One of the commonly used exfoliation methods includes hydrofluoric acid, which selectively etches the “A” layer of MAX, leaving loosely packed MXene layers. After which, the layers intercalate via hydrogen interaction or van der Waals, which can then be easily broken further via sonication. In comparison to the preparation of zeolite nanosheets, pure MXene nanosheets can be obtained easily. Current studies have shown considerable advantages in gas separation, though only a few have been reported³⁵. Further investigation of MXene membranes at high pressure and controlling the distance between the adjacent layers is required for commercialization.

Layered double hydroxides (LDH), also known as anionic clays, are composed of positively charged brucite-like ($\text{Mg}(\text{OH})_2$ structure) layers, compensating anions and solvent molecules (Fig. 1.6). The layers are made up of di- and tri-valent metal hydroxide

ions (e.g., Mg^{2+} , Mn^{3+}). Like MXenes and TMDs, LDH membranes also depend on nanochannels between the layers for separation³⁶. Only a few groups have attempted to prepare LDH nanosheet membranes for gas separation and have found applications in hydrogen recovery, though its performance is not superior to free-standing MXene membranes²⁸.

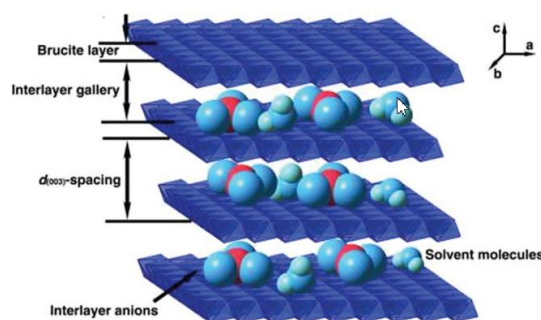


Figure 1.6: Structure of layered double hydroxide crystals, where the brucite-like layers are made up of stacked metal hydroxides and the water molecules along with compensating anions located in the interlayer gallery. Republished with permission of Royal Society of Chemistry from Ref. [28]; permission conveyed through Copyright Clearance Center, Inc.

1.2.2 Hybrid

Like MMMs, hybrid membranes use inorganic-organic crystalline polymers with different transport properties for superior performance and easy processability in membranes. Metal-organic frameworks (MOFs), as well as zeolites imidazolate frameworks (ZIFs), are hybrid crystalline polymers, where the multitopic organic ligands connect the inorganic metallic nodes. MOFs can be varied in size, geometry, and functionality leading to a report of over 20,000 different MOFs in the past decade³⁷. By selecting from the numerous available inorganic/organic building blocks, pores and cavities present in MOFs can be adjusted based on the guest molecular dimensions making MOFs an excellent choice for preparing new molecular sieving membranes. Furthermore, the surface area of these membranes (1000-10,000 m^2/g) exceeds traditional porous materials such as carbons and zeolites, making them ideal candidates for applications in catalysis, energy storage, etc. They have been prepared using both top-down and bottom-up methods; these two methods are commonly used in nanofabrication, where the top-down methods refer to the synthesis

of nanostructures by etching/removal of crystal planes that are present on the substrate, and the bottom-up approach synthesizes nanostructures onto the substrate by stacking atoms on top of the other and eventually lead to crystal plane stacking. In general, 2D MOF nanosheet membranes have shown excellent performance in separations involving H₂/CO₂, CO₂/N₂, and CO₂/CH₄ because of their relatively smaller pore size. However, fabrication of defect-free membranes even at the lab scale remains a challenge, as such free-standing MOF membranes and MOF-supported MMMs are two good approaches for preparing gas membranes with high performance^{26,38}.

1.2.3 Organic

Assembly of 2D organic nanosheets is an emerging field and offers the advantages of large surface area, defined pore sizes for molecular sieving, inherent flexibility, and ease of processing. Conventional chain polymers have already been heavily explored and employed, but the synthesis of 2D organic polymers is still largely unexplored. Intrinsic porous materials exhibit unique properties compared to non-porous materials and are being researched for applications in energy storage and catalysis²⁸. In this context, atomically precise structures, like those present in a covalent organic framework (COF), have become the center of attention in the past decade.

Covalent organic framework (COF)

COFs are a class of crystalline porous organic polymers assembled by connecting organic linkers via strong covalent bonds and promising versatile applications in gas separation, drug delivery, proton conduction, and energy storage²⁸. More than 100 COF structures and twice as many derivatives have been synthesized since the first report of COFs because of their inherent porosity and well-ordered pores that can be easily designed, tuned, and modified³⁹. However, only a few synthesized COFs have been studied as membranes for gas separation applications, primarily mixed 2D COF-polymer membranes. This may be because the pores of most COFs are larger than 1 nm, which is much larger than the kinetic diameter (KD) of gases like hydrogen (2.9 Å), carbon dioxide (3.3 Å), and methane (3.8 Å) – making molecular sieving separation unobtainable. Recently, various post-modifications (such as the addition of ligands with functional groups -OH) have enabled

the formation of small, intercalated pores (0.3-0.5 nm) and free-standing COFs, which have aided high separation selectivity in gases through ultrathin 2D COF-based membranes^{28,39}. More work needs to be done for making large area and deflection-free COF membranes.

1.2.4 Carbon

Graphene and graphene oxide (GO) are organic materials but are placed in the carbon category to differentiate them from other standard polymers and COFs. Both graphene and GO have been widely investigated for applications in energy storage, water desalination, fuel-cell technology, and hydrogen extraction⁴⁰. Graphene (monolayer of graphite) contains sp^2 hybridized carbon atoms arranged in a two-dimensional honeycomb lattice and can be prepared using both bottom-up (e.g., chemical vapor deposition) and top-down exfoliation (e.g., plasma exfoliation). On the other hand, GO is prepared by chemical oxidation and exfoliation of graphite. Further chemical reduction forms reduced graphene oxide⁴¹ (rGO) – as shown in Figure 1.7.

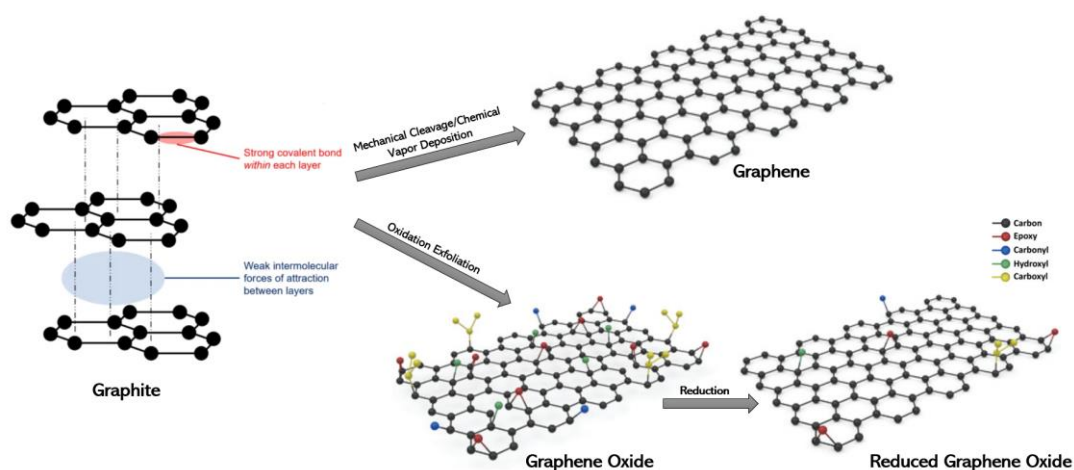


Figure 1.7: Schematic illustration of possible ways to prepare graphene, graphene oxide and reduced graphene oxide. Reprinted from Ref. [42], Copyright 2019, with permission from Elsevier.

Graphene

Graphene membranes have gained tremendous attention as they promise hundreds of times higher production rates than conventional polymer membranes while maintaining the low

operating costs⁹. Being a single atom thick, graphene can support holes the size of small molecules, creating a molecular sieve that allows smaller molecules to pass through while completely blocking larger molecules. Its thinness also imposes minimal resistance to fluid flow enabling high production rates, resolving the major performance limitation of conventional polymer membranes in industrial applications^{9,26,28}. Unfortunately, the lattice structure of graphene is so densely packed that it is inherently impermeable to gases (even as small as hydrogen and helium) and liquids. Numerous methods like focused ion beam irradiation (FIB), microwave combustion, and chemical etching have been used to generate nanometer-scale pores in graphene sheets to make them selectively permeable – made possible by their high mechanical and chemical stabilities⁴⁰. Porous membranes made up of bilayer graphene and hole sizes between 10 nm to 1 μm showed high gas permeance and low selectivity due to non-selective pores⁴³. Although few-layered graphene materials have been prepared, intrinsic defects from chemical vapor deposition and extrinsic defects from graphene transfers to the support are challenges that remain. However, the procedures are still being continually challenged, and drilling techniques are not available in industries or for large-scale applications; thus, a new approach needs to be investigated and developed to maximize the potential of graphene in gas-separation applications.

Graphene Oxide (GO)

GO (oxidized form of graphene) has numerous oxygen-containing groups like hydroxyl, carboxyl, or epoxy. Compared to graphene, GO is easy to manipulate and synthesize as oxidation of graphite is a relatively inexpensive process⁴¹. As GO sheets are nonporous, GO-based membranes are made by stacking nanosheets to create interlayer nanochannels that can separate incoming molecules²⁸. The oxygen-containing groups improve selectivity by interacting with the incoming molecules. Controlling the distance between the adjacent layers is key to producing high-performance GO membranes, which can be done using cations (such as K^+ , Li^+ , Mg^{2+} , Fe^{2+}). Though significant progress has been made and GO membranes display high permeance and selectivity, some challenges persist, such as defects produced from exfoliation, scale-up for industry, and pinholes produced during assembly into laminar membranes⁴¹.

1.3 Intrinsically Porous Atomically Thin Membranes

Membranes made from atomically thin materials promise hundreds of times higher production rates than conventional polymer membranes for gas separation applications such as natural gas purification and carbon dioxide sequestration⁴⁴. These membranes use sub-nanometer pores to separate gas molecules based on size to achieve high purity. However, creating trillions of equally sized pores per square centimetre for large-scale, high performance atomically thin membranes from graphene has proven to be a major obstacle. By instead choosing an inherently porous two-dimensional material that naturally has identical pores repeated at high density over the entire material, it may be possible to circumvent this challenge. The most promising materials with this property are graphdiyne and 2D polyphenylene (also known as porous graphene)⁴⁵. These materials have been synthesized and simulation studies show that their pore size is ideal for gas separation.

In 2009, Bieri et al.⁴⁶ successfully synthesized porous graphene (form of two-dimensional polyphenylene), which structurally resembles graphene but has periodically missing phenyl rings, leading to nearly circular pores (shown in Fig 1.8). In graphdiyne, triangular pores occur because the linkage between the adjacent benzene rings formed by carbon chains are made up of two conjugated C-C triple bonds⁴⁷. At present, theoretical studies by molecular dynamics or first-principle computations have been performed extensively on these porous graphene membranes rather than experimental work for gas separation applications^{48,49}.

1.3.1 Porous Graphene (2D Polyphenylene)

Porous graphene is modified graphene with single-atom wide pores occurring with sub-nanometer periodicity. Using the first-principle density functional theory calculations, Jiang et al.⁴⁸ first simulated gas separation properties of porous graphene with nitrogen functionalized or hydrogen passivated sub-nm pores. The simulated porous graphene showed much higher selectivity and permeance for the separation of hydrogen gas (H₂) from methane (CH₄) than conventional membranes. Later, Li et al.⁴⁹ theoretically evaluated porous graphene as a hydrogen purification membrane relative to CO₂, carbon-monoxide

(CO), and CH₄, using the more realistic porous graphene (2D polyphenylene) – synthesized by Bieri et al.⁴⁶ using the self-assembly of a molecular building block – hexaiodo-substituted cyclohexa-m-phenylene (CHP). They determined that the pores in this material have a hexagonal shape, a width of approximately 2.48 Å, and an energy barrier of 0.61 eV for H₂ to pass through. This energy barrier exists as the KD of H₂ is 2.89 Å, bigger than the pore size in 2D polyphenylene, so the gas molecule cannot pass through the pore freely. The computed diffusion barriers were 2.21 eV, 2.35 eV, and 5.19 eV for CO₂, CO, and CH₄, respectively, based on their larger kinetic diameters. Molecules other than from H₂ have a difficult time passing through the membrane, and thus, the material exhibits remarkably high selectivity of 10²⁶, 10²⁹, and 10⁷⁶ for H₂/CO₂, H₂/CO, and H₂/CH₄, respectively⁴⁴. Blackenburg et al.⁵⁰ also determined the material's hydrogen and helium separation ability in the range of 10³ up to 10²³ – at room temperature with permeance greater than 10⁻⁶ m⁻²s⁻¹ Pa⁻¹. When calculating their energy barriers, dispersion interactions were included yielding 0.37 eV and 0.43 eV for H₂ and He, respectively. These values are about 35% smaller than the values presented by Li et al.⁴⁹. Compared to current silica and carbon membranes with a selectivity of 10 to 10³ for H₂/CH₄ and H₂/CO₂, 2D polyphenylene is an ideal candidate to produce hydrogen and helium with lower operating costs and greenhouse gas emissions than methods currently in use⁵⁰. Porous graphene membranes are a promising material for gas separation applications. Nevertheless, large-scale synthesis is the next big challenge as the current synthesis of 2D polyphenylene is not only long and tedious, but the difficulty of transferring the material from one substrate to another without damaging the material is also a concern⁴⁵.

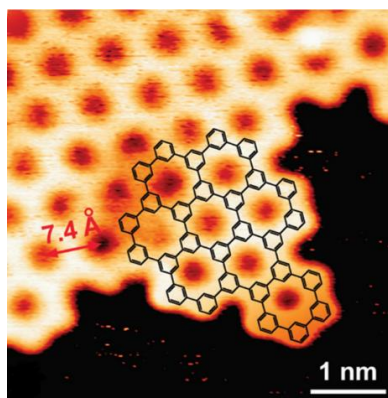


Figure 1.8: Scanning tunneling microscopy (STM) image of the synthesized 2D polyphenylene polymer network on a silver substate, where the structure of the CHP backbone can be easily recognized. Republished with permission of Royal Society of Chemistry from Ref. [46]; permission conveyed through Copyright Clearance Center, Inc.

1.3.2 Graphdiyne (Graphyne-2)

Graphdiyne (also known as graphyne-2) is a member of the graphyne family and has uniformly distributed triangular pores that arise because of its structure and form nanoporous membranes. In 1987, Baughman et al.⁵² first proposed graphyne (an allotrope of carbon), an atom-thick planar sheet with a lattice of hexagonal benzene rings linked by acetylene bonds (H-C≡C-H) in a 2D plane. Here, the number of C-C triple bonds determines the different kinds of graphyne (graphyne-2, graphyne-3, and so on), and the more triple bonds mean a greater pore size, enabling the graphyne family to be used to separate particles of all kinds of sizes⁵¹. However, graphyne itself has not yet been synthesized, and the energy barrier for the permeance of hydrogen is 1.98 eV, making it unsuitable for gas separation applications under normal experimental conditions. Therefore, graphdiyne (graphyne-2) with a slightly bigger pore size of 3.8 Å, and a low energy barrier of 0.1 eV for the permeance of hydrogen (KD of 2.93 Å), is instead investigated as the gas-separation membrane. Under standard temperature and pressure (300K, 100 kPa), gases like CO (KD of 3.76 Å) and CH₄ (KD of 3.83 Å) were computed to have energy barriers of 0.33 and 0.72 eV, respectively. The obtained selectivity was 10³, 10³, and 10⁹ for H₂/CO, H₂/N₂, and H₂/CH₄ respectively⁵³, where graphdiyne does not show significant advantages for small gas molecules (like CO and N₂) but is still superior to

commercially available membranes⁵⁴. Furthermore, the mass flux of H₂ molecules was reported to be on the order of 7-10 g/cm²s.

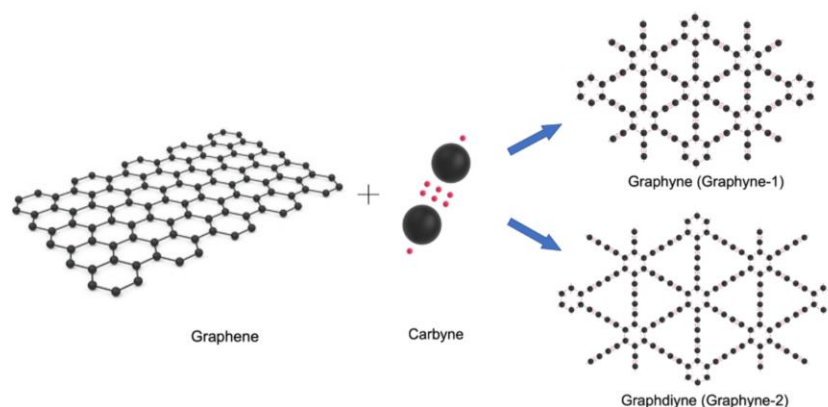

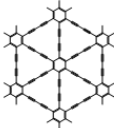


Figure 1.9: Illustration that highlights the difference between graphene, graphyne, and graphdiyne, which is simply the number of carbynes present between hexagonal benzene rings. Obtained from Ref. [55].

Several attempts have been made to synthesize graphdiyne. In 2010, a graphdiyne film with a thickness of 1 μm was prepared on the surface of copper foil using a Glaser coupling reaction, resulting in further studies in order to make graphdiyne with a well-defined structure and thickness of <10 nm. In 2017, graphdiyne nanosheets were produced through carbon-carbon coupling amongst monomers (hexaethynylbenzene-HEB) at liquid/liquid and gas/liquid interface while in the presence of a copper catalyst. As a result, multilayer graphdiyne nanosheets of a thickness of 24 nm (liquid/liquid) and 3 nm (gas/liquid) were prepared. However, the synthesis involves using an unstable and explosive HEB monomer. Moreover, the procedure must be done in an argon atmosphere in the dark, which is difficult in industrial settings⁵⁶. Another approach is exfoliating commercially available graphdiyne powder into a single or a few layers, as flake sizes of 3-5 nm have been reported using these methods. Liquid exfoliation using inorganic salts (i.e., Li₂SiF₆)⁵⁷ and ultrasonication treatment⁵⁸ are two methods reported to disperse the nanosheets present in the dispersion liquid. Computational studies lay the groundwork for future experiments using graphdiyne, as it has good hydrogen separation abilities and can be used as a gas-separation membrane, though experimental data is needed to confirm these findings.

Table 1.1: Synthesis methods, and characteristics of 2D graphdiyne and 2D polyphenylene nanosheets cited in literature.

	STRUCTURE	SYNTHESIS METHODS	PORE SIZE	MONOLAYERS/ SUSPENDED	SELECTIVITY AND PERMEANCE	CONS.	REF.
2D Polyphenylene		Surface-assisted coupling of cyclohexa-m-phenylene (CHP) with metal surfaces like Ag (111) at 745K	<i>Diameter</i> 2.48 Å	Yes/No	<i>Selectivity</i> 10 ⁴ H ₂ /Ne 10 ¹⁷ H ₂ /CO ₂ 10 ²³ H ₂ /NH ₃ 10 ⁴ He /Ne 10 ¹⁷ He /CO ₂ 10 ²³ He /NH ₃ <i>Permeance</i> 10 ⁻⁶ m ⁻² s ⁻¹ Pa ⁻¹	Limited to small area membranes	46 50 59
Graphdiyne (n=2)		Interface-assisted synthesis using hexaethynylbenzene (HEB) and a copper catalyst	<i>Length</i> 5.42 Å	No/Yes	<i>Selectivity</i> 10 ³ H ₂ /CO 10 ³ H ₂ /N ₂ 10 ⁹ H ₂ /CH ₄ <i>Permeance</i> 7-10 g/cm ² s	Unstable and explosive monomer Limited to small area membranes	47 53 60

1.4 Fundamentals of membrane-based gas separation

1.4.1 Permeance and Permeability

Gas permeance is the ability of a material or a membrane to permit the passage of liquids or gases and is a parameter quite often used to evaluate the performance of membranes. It can be defined as the throughput of a permeant through a membrane area in a given time for a particular pressure difference applied between the two sides of the membrane^{28,61}. It can be expressed as:

$$Q = \frac{V}{A\Delta P} \quad (1.1)$$

where Q is expressed in gas permeation units (GPU = 10⁻⁶ cm³ (STP)/cm²sHg), V [cm³ (STP)/s] is the gas flux through the membrane, ΔP is the pressure difference [cmHg] and A is the effective membrane area [cm²]

Gas permeability (P) can be expressed as the product of the permeance (Q) and the thickness of the membrane. It is in units of Barrer [1 Barrer = 10⁻¹⁰cm³ (STP) cm/cm²s cmHg]. It reflects the intrinsic properties of the membrane material and is frequently used

for dense membranes. However, it is not often used for very thin membranes where permeability is not constant with material thickness⁶¹. Permeability for polymeric and porous materials can also be expressed by multiplying the diffusion coefficient (D) and the solubility coefficient/adsorption capacity (S).

1.4.2 Selectivity

Selectivity is the ability of a membrane to permit the passage of desirable species while blocking undesired ones. It is used to assess the separation ability of a membrane. It is defined as the ratio of permeation rates of a fast-moving and a slow-moving gas^{9,61}.

$$\text{Selectivity} = \frac{\text{Permeance of species A}}{\text{Permeance of species B}} \quad (1.2)$$

1.4.3 Transport Mechanisms

The solution-diffusion model describes the transport mechanism in dense membranes with no natural pores and is commonly applied to polymeric gas separation membranes⁶³. In this case, the permeating gas species absorbs into the membrane material and diffuses through the layer by means of a concentration gradient, then desorbs from the membrane. Separation is achieved because different gasses have different solubilities and diffusivities in the membrane material. In general, as gas molecule size increases, the diffusion coefficient decreases. The diffusion coefficient can be increased by improving the polymer chain flexibility and increasing the fractional free volume (space not occupied by polymer molecules)^{9,64}. Changing the structure of the polymer material tends to change the diffusivity of all gas species in the membrane. Consequently, more permeable materials tend to offer lower selectivity, causing a trade-off between permeability and selectivity known as the Robeson limit¹⁵. To overcome this trade-off, alternative separation mechanisms such as chemical affinity and molecular sieving have been explored (e.g., high free-volume polymers). Molecular sieving is the ability of a crystalline material with pores to allow the passage of smaller molecules while sterically impeding larger ones⁹. Membrane gas transport with pore diameters just above the molecular size is primarily governed by Fickian diffusion, surface adsorption, and condensation of gas molecules in the pores of membranes. When considering pore diameters larger than molecular size but

smaller than gas mean free path, Knudsen diffusion governs instead. In Knudsen diffusion, collisions of molecules with the pore wall are more prominent than collisions between molecules. Thus, a molecule with lower molecular mass travels faster and has high permeance compared to a molecule with higher molecular mass²⁸.

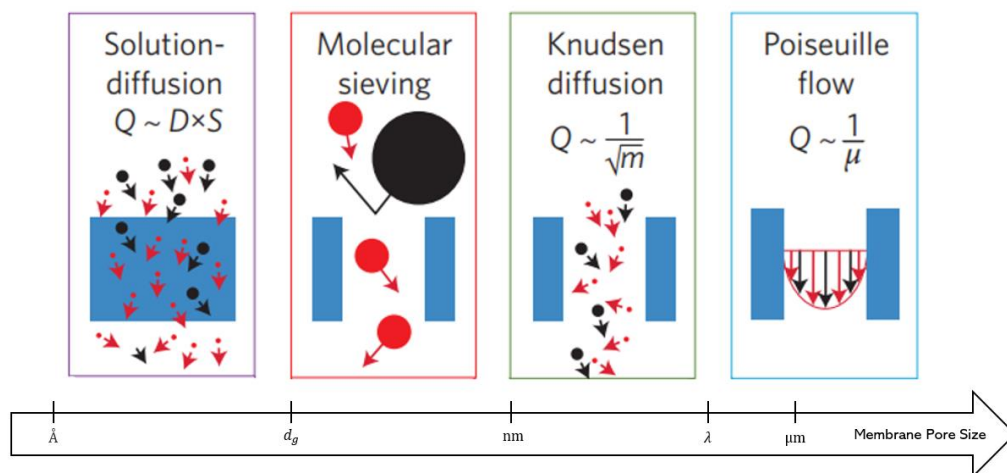


Figure 1.10: Various membrane transport mechanisms as the pore size of a membrane increases, where d_g is the gas molecular diameter, and λ is the gas mean free path. Relationships between Q (flux), D (diffusivity), S (sorption coefficient), m (molecular mass) and μ (viscosity) is provided as needed for the four transport mechanisms. Reprinted by permission from Springer Nature and Copyright Clearance Center: Springer Nature, Nature Nanotechnology, Ref. [9], Copyright 2017.

1.4.4 Gas Transport through Nanoporous Atomically Thin Membranes

Theoretical studies have been used to explore the potential of intrinsically porous atomically thin membranes in the transport of different gases. One approach is to utilize quantum mechanical methods like density functional theory (DFT) to calculate the energy barrier required for a gas molecule to cross a pore⁹. Given the gas molecule kinetic energy distribution, permeance can be estimated via a transition state approach, whereas the ratio of Arrhenius factors (Eq. 1.3) is used to estimate selectivity. DFT can solve higher selectivity, but some present unreasonably low permeance^{9,50}.

$$S_{H_2/C_n} = \frac{r_{H_2}}{r_{C_n}} = \frac{A_{H_2} e^{-E_{H_2}/RT}}{A_{C_n} e^{-E_{C_n}/RT}} \quad (1.3)$$

where S_{H_2/C_n} is the selectivity of the membrane for the diffusion of H_2 relative to CO_2 , r is the diffusion rate, A is the frequency factor, E (J/mol) is the activation energy, R (J/mol*K) is the gas constant and T (K) is temperature.

Another approach is to utilize classical molecular dynamics (MD) simulations to calculate the rate at which a molecule crosses a pore, which is directly proportional to permeance^{9,60}. These studies have permitted researchers to explore different conditions and have led to the realization of the dependence of permeance and selectivity on molecule size, mass, functional group interactions on the pore, tunneling rates, etc. MD can be used to calculate high permeance but not high selectivity ($>10^3$) since low flow rates will mean a small number of observable molecule crossings in the feasible simulation time of <100 ns.

To understand the gas transport through these atomically thin pores, the diameters of the gas molecule (D_m) and pore (D_p) are compared. When the pore diameter is larger than the gas molecule, molecular flow occurs across a thin aperture that is smaller than the gas mean free path. In this case, steric considerations dominate, and the effective pore area (A_{eff}) is smaller than the pore area (A_{pore}).

$$A_{eff} \approx \frac{\pi}{4} (D_p - D_m)^2 \quad (1.4)$$

$$A_{pore} = \left(\frac{\pi}{4}\right) D_p^2 \quad (1.5)$$

When the pore size is equal to or smaller than the gas molecule, an energetic barrier is present that needs to be overcome for the transport of gas molecules. This is denoted as the activated regime. As pore size decreases below the molecular pore size, the activated regime has a lower A_{eff} and permeation constant, whereas the steric regime has a higher A_{eff} and permeation constant.

The Lennard-Jones potential is a simplified model that is used to describe the interactions between non-binding atoms/molecules and is dependent on the distance by which they are separated⁹. Assuming a rigid pore with fixed atoms, this model can be used to approximate the molecule-pore interaction (Eq. 1.6).

$$E \approx \frac{\pi D_c}{a} 4\varepsilon \left[\left(\frac{\sigma}{D_c/2} \right)^{12} - \left(\frac{\sigma}{D_c/2} \right)^6 \right] \approx \frac{4\pi\varepsilon D_c}{a} \left(\frac{\sigma}{D_c/2} \right)^{12} \quad (1.6)$$

where E is the barrier height, a is the distance between adjacent atoms on the pore rim, ε is the depth of the potential well, σ is referred to as the size of the particle, $D_c/2$ is the distance from the center of the pore to the center of the atoms that make up the pore, and $\pi D_c/a$ provides the average number of atoms present on the pore rim (Fig. 1.11).

$$\frac{A_{eff}}{A_{pore}} \approx \frac{1}{2} \operatorname{erfc} \left(\sqrt{\frac{E}{k_B T}} \right) \quad (1.7)$$

where k_B is the Boltzmann constant.

Eq. 1.7 is used to calculate the effective pore size, which can be obtained after assuming that all gas molecules with kinetic energies that can exceed the barrier height in Eq. 1.6, can cross the pore.

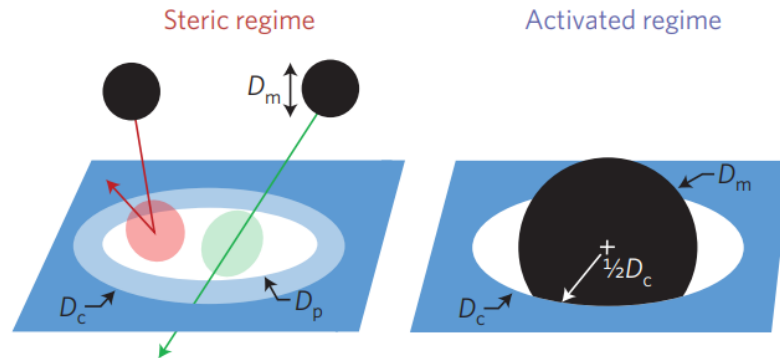


Figure 1.11: Illustrates the steric and activated regime mechanisms for gas transport. Reprinted by permission from Springer Nature and Copyright Clearance Center: Springer Nature, Nature Nanotechnology, Ref. [9], Copyright 2017.

Given two different gas molecules, three possible scenarios exist **A)** In the case of large pores, high selectivity cannot be achieved as transport of both gases is through the steric regime. **B)** When pore size is larger than one gas (activated regime) but smaller than the other (steric regime), high permeance and selectivity can be achieved via molecular sieving. **C)** For small pores, transport only occurs in the activated regime, providing very high selectivity but low permeance due to the dependence of energy barrier on pore size⁹.

In 2012, Koenig et al.⁶⁵ was the first to report experimental evidence of molecular sieving through porous graphene. For the experiment, a single pore was created in bilayer graphene (initially impermeable) using ultraviolet/ozone etching. The material was then charged with various gases creating a nanoballoon, after which the rate of deflection was monitored using atomic force microscopy (AFM). In agreement with theoretical studies, selectivity above 10,000, and permeance in the range of 10^{-23} to 10^{-21} mol/Pa*s was observed⁶⁵. It is important to perform controlled experiments as it highlights unaccounted parameters or fluctuations that do not occur in simulations.

1.5 Industrial Applications of Gas Separation Membranes

Major industrial applications for gas separation membranes include hydrogen separation, separation of carbon-dioxide and water from natural gas, nitrogen, and organic vapor from air²⁸. Over the years, hydrogen gas has become widely used in chemical, metallurgy, and electronic sectors, so demand for efficient hydrogen gas production is at an all-time high. It has also been deemed the energy carrier of the future because it can be used as fuel for zero-emission vehicles, as when H₂ combusts, it only produces water (clean energy)⁶⁶. The primary method of hydrogen production is via steam-methane reforming, as other processes have a high cost of production (e.g., electrolysis) or are still at the laboratory scale (e.g., thermochemical water splitting). In steam-methane reforming, natural gas methane (CH₄) reacts with high-temperature steam (over 700°C) under pressure (3-25 bar) in the presence of a catalyst to produce hydrogen, carbon dioxide, and carbon monoxide⁶⁷. Separating hydrogen from these species is important for its usage and storage, but current membranes require high temperatures, increasing the cost of production while providing non-optimal permeance and selectivity⁶⁸. However, membrane gas separation using graphene or intrinsically porous atomically thin membranes can significantly reduce energy consumption and cost while providing maximum achievable permeance and high selectivity⁶⁹.

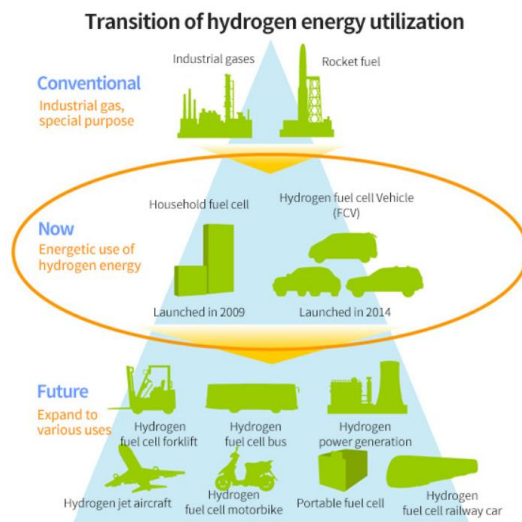


Figure 1.12: Pyramid illustration highlighting the expansion of applications in hydrogen energy. Obtained from Ref. [66].

1.6 Thesis Goals and Objectives

Interest in graphene as a separation membrane material is evident for a wide range of applications, such as desalination, carbon capture, and hydrogen production. Graphene membranes promise hundreds of times higher production rates than conventional polymer membranes while maintaining the low operating costs that make membrane-based separation processes attractive. Being a single atom thick, graphene can support holes the size of small molecules, creating a molecular sieve that allows smaller molecules to pass through while completely blocking larger molecules. Its thinness also imposes minimal resistance to fluid flow enabling high production rates, resolving the major performance limitation of conventional polymer membranes in industrial applications.

Unfortunately, the lattice structure of graphene is so densely packed that it is inherently impermeable to gases and liquids. Methods like electron-beam irradiation and chemical etching must be used to generate nanometer-scale pores in graphene sheets to make them selectively permeable. However, creating trillions of sub-nanometer holes per square centimeter of the same size has proven difficult. My project aims to develop atomically thin membranes that solve this problem by replacing the graphene layer with an intrinsically porous 2D polymer. Such materials naturally have a high density of sub-nanometer pores repeated exactly over their entire surface area, circumventing the pore

creation challenge in graphene. The synthesis and measurement tools I developed will provide a framework to explore the performance of other intrinsically porous graphene-like materials, which will be selective to different molecules and extend the range of separation applications possible from atomically thin membrane technology.

Chapter 2 will explain the experimental techniques and instruments used in this thesis (e.g., Atomic Force Microscopy, Schlenk line, etc.). Chapter 3 directs its focus on developing membranes made from 2D polyphenylene – also known as porous graphene. Unlike graphene, single layers of 2D polyphenylene are not commercially available. Thus, the first phase of my research project covers the synthesis of this material and the challenges faced to obtain the monomer, hexaiodo-substituted cyclohexa-m-phenylene (CHP). In chapter 4, the experimental design and development of graphdiyne (GDY) membranes are expanded on. Chapter 5 details theoretical and computation work exploring convection-diffusion through an infinitely thin orifice plate, a model for a graphene pore, using the computational fluid dynamics (CFD) software OpenFOAM (Open-source Field Operation and Manipulation)⁷⁰ and ANSYS Fluent⁷¹. Finally, Chapter 6 will conclude and provide future directions for this work.

1.7 References

1. King, C.J., Separation processes. Courier Corporation **2013**.
2. Tzschucke, C.C.; Markert, C.; Bannwarth, W.; Roller, S.; Hebel, A.; Haag, R. Modern separation techniques for the efficient workup in organic synthesis. *Angewandte Chemie International Edition* **2002**, *41*, 3964-4000
3. Osada, Y.; Nakagawa, T. Membrane Science and Technology. *New York: Marcel Dekker, Inc.* **1992**.
4. Zeman, L.J.; Zydney, A.L. Microfiltration and ultrafiltration: principles and applications. *CRC press* **2017**.
5. Lipnizki, J.; Adams, B.; Okazaki, M.; Sharpe, A. Water treatment: Combining reverse osmosis and ion exchange. *Filtration+ Separation* **2012**, *49*, 30-33.
6. Baker, R.; Low, B. Gas Separation Membrane Materials: A Perspective. *Macromolecules* **2014**, *47*, 6999-7013.
7. Baker, R. W. Membrane Technology and Applications. *John Wiley & Sons* **2004**.
8. Wenten, I.G. Recent development in membrane science and its industrial applications. *Journal of Science Technology and Membrane Science Technology* **2002**, *24*, 1010-1024.
9. Wang, L.; Boutilier, M.S.; Kidambi, P.R.; Jang, D.; Hadjiconstantinou, N.G.; Karnik, R. Fundamental transport mechanisms, fabrication and potential applications of nanoporous atomically thin membranes. *Nature nanotechnology* **2017**, *12*, 509.
10. Mahajan, R.; Koros, W.J. Mixed matrix membrane materials with glassy polymers. *Polymer Engineering & Science* **2002**, *42*, 1420-1431.
11. Bernardo, P.; Drioli, E.; Golemme, G. Membrane Gas Separation: A Review/State of the Art. *Industrial & engineering chemistry research* **2009**, *48*, 4638-4663.
12. Selatile, M.K.; Ray, S.S.; Ojijo, V.; Sadiku, R. Recent developments in polymeric electrospun nanofibrous membranes for seawater desalination. *RSC advances* **2018**, *8*, 37915-37938.
13. Stookey, D.J.; Graham, T.E.; and Pope, W.M. Natural gas processing with PRISM separators. *Environmental Progress* **1984**, *3*.
14. Strathmann, H. Membrane separation processes: current relevance and future opportunities. *American Institute of Chemical Engineers* **2001**, *47*, 1077.

15. Robeson, L. M. Correlation of separation factor versus permeability for polymeric membranes. *Journal of Membrane Science* **1991**, *62*, 165
16. Synder Filtration, Hollow Fiber Membranes, 2020, <https://synderfiltration.com/learning-center/articles/module-configurations-process/hollow-fiber-membranes/>
17. Baker, R. W. Membranes for Vapor/Gas Separation, 2006, <http://www.mtrinc.com/publications/>.
18. Tanaka, K.; Okamoto, K.-I.; Structure and Transport Properties of Polyimides as Materials for Gas and Vapor Separation Membranes. *In Materials Science of Membranes for Gas and Vapor Separation*; Yampolskii, Yu.; Pinnau, I.; Freeman, B. D. Eds.; Wiley: Chichester, UK, 2006; Chapter 10, pp 271-291.
19. Budd, P. M.; Msayib, K. J.; Tattershall, C. E.; Ghanem, B. S.; Reynolds, K.-J.; McKeown, N. B.; Fritsch, D. Gas separation membranes from polymers of intrinsic mesoporosity. *Journal of Membrane Science* **2005**, *251*, 263.
20. Lin, Y. S. Microporous and dense inorganic membranes: current status and prospective. *Separation and Purification Technology* **2001**, *25*, 39.
21. Fernández-Castro, P.; Ortiz, A.; Gorri, D. Exploring the Potential Application of Matrimid® and ZIFs-Based Membranes for Hydrogen Recovery: A Review. *Polymers* **2021**, *13*, 1292.
22. Zimmerman, C. M.; Singh, A.; Koros, W. J. Tailoring mixed matrix composite membranes for gas separations. *Journal of Membrane Science* **1997**, *137*, 145.
23. Mahajan, R.; Koros, W. J. Factors controlling successful formation of mixed-matrix gas separation materials. *Industrial and Engineering Chemistry* **2000**, *39*, 2692.
24. Guo, A.; Ban, Y.; Yang, K.; Yang, W. Metal-organic framework-based mixed matrix membranes: Synergetic effect of adsorption and diffusion for CO₂/CH₄ separation. *Journal of Membrane Science* **2018**, *562*, 76-84.
25. Rashed, A.O.; Merenda, A.; Kondo, T.; Lima, M.; Razal, J.; Kong, L.; Huynh, C.; Dumée, L.F., Carbon nanotube membranes-strategies and challenges towards scalable manufacturing and practical separation applications. *Separation and Purification Technology* **2020**, 117929.
26. Pulizzi, F.; Bubnova, O.; Milana, S.; Schilter, D.; Abergel, D.; Moscatelli, A. Graphene in the making. *Nature nanotechnology* **2019**, *14*, 914-918.
27. Liu, G.; Jin, W.; Xu, N. Two-Dimensional-Material Membranes: A New Family of High-Performance Separation Membranes. *Angewandte Chemie International Edition*. **2016**, *55*, 13384 – 13397.

28. Liu, M.; Gurr, P.A.; Fu, Q.; Webley, P.A.; Qiao, G.G. Two-dimensional nanosheet-based gas separation membranes. *Journal of Material Chemistry A* **2018**, *6*, 23169.
29. Tsapatsis, M. 2-dimensional zeolites. *American Institute of Chemical Engineers* **2014**, *60*, 2374 – 2381.
30. De Meis, D.; Richetta, M.; Serra, E. Microporous inorganic membranes for gas separation and purification. *Interceram-International Ceramic Review* **2018**, *67*, 16-21.
31. Varoon, K.; Zhang, X.; Elyassi, B.; Brewer, D.D.; Gettel, M.; Kumar, S.; Lee, J.A.; Maheshwari, S.; Mittal, A.; Sung, C.Y.; Cococcioni, M. Dispersible exfoliated zeolite nanosheets and their application as a selective membrane. *Science* **2011**, *334*, 72-75.
32. Zhu, X.; Tian, C.; Do-Thanh, C.L.; Dai, S. Two-Dimensional materials as prospective scaffolds for mixed-matrix membrane-based CO₂ separation. *ChemSusChem* **2017**, *10*, 3304-3316.
33. Xu, M.; Liang, T.; Shi, M.; Chen, H. Graphene-like two-dimensional materials. *Chemical reviews* **2013**, *113*, 3766-3798.
34. Shen, J.; Liu, G.; Ji, Y.; Liu, Q.; Cheng, L.; Guan, K.; Zhang, M.; Liu, G.; Xiong, J.; Yang, J.; Jin, W. 2D MXene nanofilms with tunable gas transport channels. *Advanced Functional Materials* **2018**, *28*, 1801511.
35. Shen, J.; Liu, G.; Ji, Y.; Liu, Q.; Cheng, L.; Guan, K.; Zhang, M.; Liu, G.; Xiong, J.; Yang, J.; Jin, W. 2D MXene nanofilms with tunable gas transport channels. *Advanced Functional Materials* **2018**, *28*, 1801511.
36. Liu, Y., Wang, N., Cao, Z. and Caro, J., 2014. Molecular sieving through interlayer galleries. *Journal of Materials Chemistry A*, *2*(5), pp.1235-1238.
37. Xue, Y.; Zhao, G.; Yang, R.; Chu, F.; Chen, J.; Wang, L.; Huang, X. 2D metal–organic framework-based materials for electrocatalytic, photocatalytic and thermocatalytic applications. *Nanoscale* **2021**, *13*, 3911.
38. Furukawa, H.; Cordova, K.E.; O’Keeffe, M.; Yaghi, O.M. The Chemistry and Applications of Metal-Organic Frameworks. *Science* **2013**, *341*, 6149.
39. Liang, R.R.; Jiang, S.Y.; Ru-Han, A.; Zhao, X. Two-dimensional covalent organic frameworks with hierarchical porosity. *Chemical Society Reviews* **2020**, *49*, 3920.

40. Bunch, J.S.; Verbridge, S.S.; Alden, J.S.; Van Der Zande, A.M.; Parpia, J.M.; Craighead, H.G.; McEuen, P.L. Impermeable atomic membranes from graphene sheets. *Nano letters* **2008**, *8*, 2458-2462.
41. Hegab, H.M.; Zou, L. Graphene oxide-assisted membranes: fabrication and potential applications in desalination and water purification. *Journal of Membrane Science* **2015**, *484*, 95-106.
42. McCoy, T.M.; Turpin, G.; Teo, B.M.; Tabor, R.F. Graphene oxide: a surfactant or particle?. *Current Opinion in Colloid & Interface Science* **2019**, *39*, 98-109.
43. Surwade, S.P.; Smirnov, S.N.; Vlassioux, I.V.; Unocic, R.R.; Veith, G.M.; Dai, S.; Mahurin, S.M. Water desalination using nanoporous single-layer graphene. *Nature nanotechnology* **2015**, *10*, 459-464.
44. Prozorovska, L.; Kidambi, P.R. State-of-the-Art and Future Prospects for Atomically Thin Membranes from 2D Materials. *Advanced Materials* **2018**, *30*, 1801179.
45. Yoon, H.W.; Cho, Y.H.; Park, H.B. Graphene-based membranes: status and prospects. *Philosophical Transactions of the Royal Society. A* **2016**, *374*, 2015002
46. Bieri, M.; Treier, M.; Cai, J.; Ait-Mansour, K.; Ruffieux, P.; Gröning, O.; Gröning, P.; Kastler, M.; Rieger, R.; Feng, X.; Müllen, K. Porous graphenes: two-dimensional polymer synthesis with atomic precision. *Chemical Communications* **2009**, *45*, 6919–6921.
47. Matsuoka, R.; Sakamoto, R.; Hoshiko, K.; Sasaki, S.; Masunaga, H.; Nagashio, K.; Nishihara, H. Crystalline Graphdiyne Nanosheets Produced at a Gas/Liquid or Liquid/Liquid Interface. *Journal of the American Chemical Society*. **2017**, *139*, 3145–3152.
48. Jiang, D-E.; Cooper VR, Dai S. Porous graphene as the ultimate membrane for gas separation. *Nano Letters*. **2009**, *9*, 4019–4024.
49. Li, Y.; Zhou, Z.; Shen, P.; Chen, Z. Two-dimensional polyphenylene: experimentally available porous graphene as a hydrogen purification membrane. *Chemical Communications* **2010**, *46*, 3672–3674
50. Blankenburg, S.; Bieri, M.; Fasel, R.; Müllen, K.; Pignedoli, C.A.; Passerone, D. Porous Graphene as an Atmospheric Nanofilter. *Small* **2010**, *6*, 2266-2271.
51. Bartolomei, M.; Carmona-Novillo, E.; Hernández, M.I.; Campos-Martínez, J.; Pirani, F.; Giorgi, G. Graphdiyne Pores: “Ad Hoc” Openings for Helium Separation Applications. *Journal of Physical Chemistry C* **2014**, *118*, 29966–29972.

52. Baughman, R.H., Eckhardt, H. and Kertesz, M., 1987. Structure-property predictions for new planar forms of carbon: Layered phases containing sp² and sp atoms. *Journal of Chemical Physics*, 87(11), pp.6687-6699.
53. Cranford, S.W.; Buehler, M.J. Selective hydrogen purification through graphdiyne under ambient temperature and pressure. *Nanoscale* **2012**, 4, 4587–4593.
54. Zhao, W.H.; Yuan, L.F.; Yang, J.L. Graphdiyne as hydrogen purification membrane. *Chin. Journal of Chemical Physics* **2012**, 25, 434
55. ACS Material. Comparing Graphene and Graphyne. 2020.
<https://www.acsmaterial.com/blog-detail/comparing-graphene-and-graphyne.html>
56. Zhou, J.; Gao, X.; Liu, R.; Xie, Z.; Yang, J.; Zhang, S.; Zhang, G.; Liu, H.; Li, Y.; Zhang, J.; Liu, Z. Synthesis of graphdiyne nanowalls using acetylenic coupling reaction. *Journal of the American Chemical Society* **2015**, 137, 7596-7599.
57. Yan, H.; Yu, P.; Han, G.; Zhang, Q.; Gu, L.; Yi, Y.; Liu, H.; Li, Y.; Mao, L. High-Yield and Damage-free Exfoliation of Layered Graphdiyne in Aqueous Phase. *Angewandte Chemie International Edition* **2019**, 58, 746-750.
58. Zhang, F.; Liu, G.; Yuan, J.; Wang, Z.; Tang, T.; Fu, S.; Zhang, H.; Man, Z.; Xing, F.; Xu, X. 2D graphdiyne: an excellent ultraviolet nonlinear absorption material. *Nanoscale* **2020**, 12, 6243-6249.
59. Xu, P.; Yang, J.; Wang, K.; Zhou, Z.; Shen, P. Porous graphene: Properties, preparation, and potential applications. *Chinese science bulletin* **2012**, 57, 2948-2955.
60. Gao, X.; Liu, H.; Wang, D.; Zhang, J. Graphdiyne: synthesis, properties, and applications. *Chemical Society Reviews* **2019**, 48, 908-936.
61. Ismail, A.F.; Khulbe, K.C.; Matsuura, T. Gas Separation Membranes. *Switz. Springer* **2015**, 10, 978-3.
62. Hashemifard, S.A.; Ismail, A.F.; Matsuura, T. Prediction of gas permeability in mixed matrix membranes using theoretical models. *Journal of Membrane Science* **2010**, 347, 53-61.
63. Ismail, A.; Kusworo, T.; Mustafa, A.; Hasbullah, H. Understanding the Solution-Diffusion Mechanism in Gas Separation Membrane for Engineering Students. *Regional Conference on Engineering Education* **2005**, 155-159.
64. Du, H.; Li, J.; Zhang, J.; Su, G.; Li, X.; Zhao, Y. Separation of hydrogen and nitrogen gases with porous graphene membrane. *Journal of Physical Chemistry C* **2011**, 115, 23261-23266.

65. Koenig, S.P.; Wang, L.; Pellegrino, J.; Bunch, J.S. Selective molecular sieving through porous graphene. *Nature nanotechnology* **2012**, *7*, 728-732.
66. Dainichi Machine and Eng. Co., Ltd. Hydrogen energy engineering. 2020. <https://www.dainichikikai.co.jp/en/hydrogenenergy/>
67. Franchi, G.; Capocelli, M.; De Falco, M.; Piemonte, V.; Barba, D. Hydrogen Production via Steam Reforming: A Critical Analysis of MR and RMM Technologies. *Membranes* **2020**, *10*, 10.
68. Shimonosono, T.; Imada, H.; Maeda, H.; Hirata, Y. Separation of hydrogen from carbon dioxide through porous ceramics. *Materials* **2016**, *9*, 930.
69. Sazali, N.; Mohamed, M.A.; Salleh, W.N.W. Membranes for hydrogen separation: a significant review. *Journal of Advanced Manufacturing Technology* **2020**, *107*, 1859–1881.
70. Jasak, H. OpenFOAM: open source CFD in research and industry. *International Journal of Naval Architecture and Ocean Engineering* **2009**, *1*, 89-94.
71. Fluent, A.N.S.Y.S. Ansys fluent. *Academic Research* **2015**. Release, 14.

Chapter 2

2 General Experimental Techniques and Equipment

2.1 Organic synthesis

2.1.1 Glove Box and Schlenk Line

Glove boxes are sealed compartments designed to permit manipulation (via attached gloves) of certain chemicals in an inert atmosphere. They are used to protect chemicals sensitive to air or water vapor, and people from being exposed to hazardous materials¹. However, to maintain the inert atmosphere, not all reagents and solvents are permitted in the glove box, and certain experiments that require heating or cooling are also challenging to perform¹. Under these circumstances, a Schlenk line is frequently used to synthesize air/water-sensitive materials. In a typical Schlenk line, a vacuum manifold is connected to a vacuum pump, and an inert gas manifold is connected to a source of inert gas (usually argon)². To visually monitor the inert gas coming out of the manifold, a bubbler is used. A liquid nitrogen trap is used to protect the vacuum pump by condensing any solvent vapors. Finally, the double oblique stopcocks allow for an easy switch between vacuum or inert gas, and the tubing is connected to a Schlenk flask in which the reaction occurs².

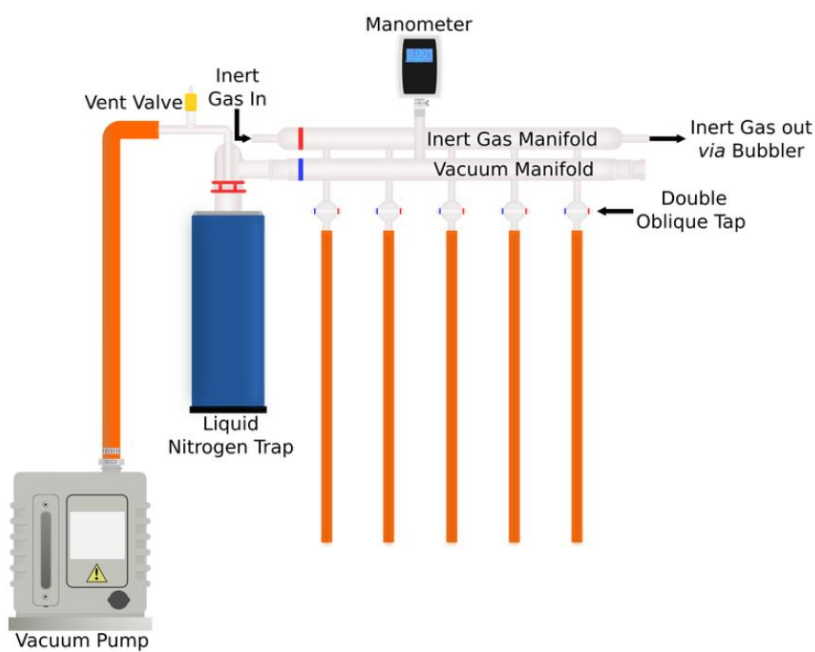


Figure 2.1: A typical Schlenk line set-up. Image was obtained from Ref. [2].

2.2 Methods of Characterization

2.2.1 Nuclear magnetic resonance (NMR) Spectroscopy and Mass Spectrometry (MS)

NMR Spectroscopy and MS are both powerful techniques used to identify and analyze organic compounds^{3,4}. NMR spectroscopy is based on atomic nuclei that have a spin and are electronically charged. In the presence of a strong magnetic field, these nuclei will behave like magnets. At a broad spectrum of radio frequencies, nuclei resonate at their frequencies³. However, when a resonating frequency is applied, these nuclei absorb this energy and undergo a “spin-flip” to align themselves against the field and reach a higher energy state⁵. The signal from these frequencies is used to create an NMR spectrum, where the height of a peak (intensity of the signal) represents the number of resonating nuclei. In organic synthesis, ^1H , ^{13}C NMR are commonly obtained as they are present in all organic molecules; other nuclei with an odd number of protons/neutrons (^{31}P) also display this property⁵. Chemical shifts in the spectrum are usually caused by the presence of electronegative atoms (such as fluorine) that remove the electron density from the nuclei of interest, causing it to be deshielded (moving downfield of the NMR spectrum)³. As nuclei are affected by the orientation of neighboring nuclei, their signal can split depending on the number of protons present on the adjacent carbon atom. For example, three neighboring hydrogen atoms can split the signal into four peaks (also known as a quartet)³.

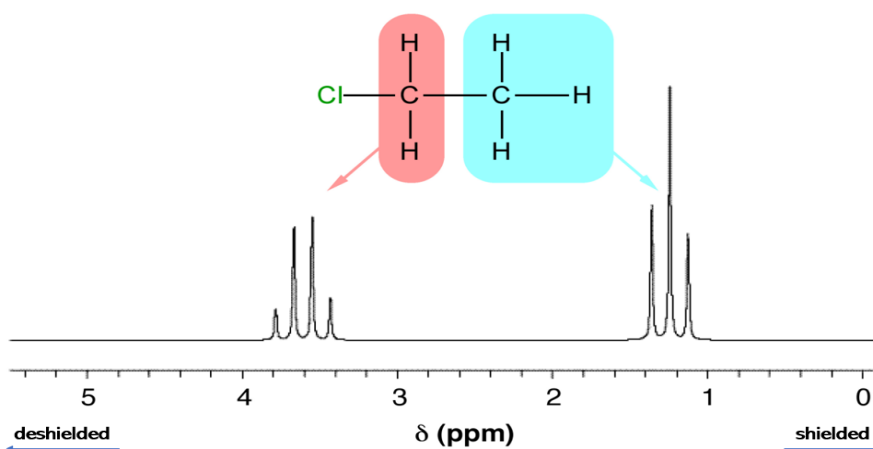


Figure 2.2: ^1H NMR spectrum for chloroethane, showing chemical shifts that correspond to the two proton signals. Note deshielding of protons near the electronegative chlorine atom. Reproduced from Ref. [6].

In MS, molecular compounds in gaseous form are ionized and broken into fragments using a high-energy electron beam. The ion fragments are then sorted based on their mass-to-charge (m/z) ratio⁴. An electric current signal, that is proportional to the intensity of charged ions, is detected and used to produce a MS spectrum (m/z vs. relative abundance)⁷.

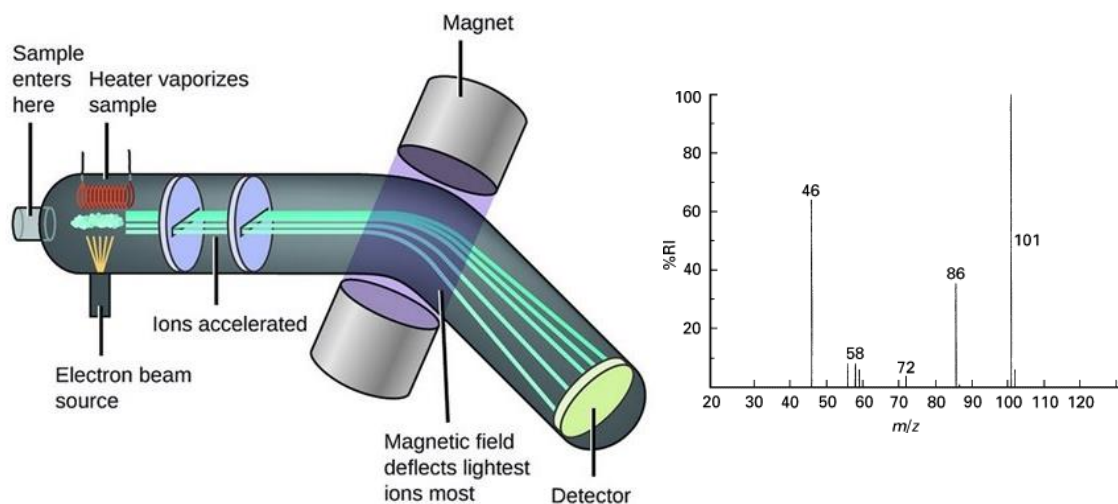


Figure 2.3: (left) A schematic illustration of mass spectrometry. Obtained from Ref. [8] (right) Results obtained from a MS spectrum. Reprinted from Ref. [9], Copyright 1999, with permission from Elsevier.

2.2.2 Scanning electron microscopy (SEM)

SEM is an electron microscopy technique that exposes the sample to a high-energy electron beam and provides information about the size, shape, texture, composition, and more. This is achieved by using a high-energy beam with the sample to produce secondary electrons, backscatter electrons, and characteristic X-rays¹⁰. Secondary electrons (low energy) originate from the sample's surface and are used to study the surface morphology, and result in the highest resolution. Backscatter electrons (high-energy) are reflected from the sample because of elastic scattering by atoms and reveal chemical compositional differences¹¹. The collected signals by detectors form images that can be resolved to as low as 1-20nm. Unlike light microscopes, electron microscopes are not limited by the wavelength of the visible spectrum of light, and electrons can attain shorter wavelengths resulting in better resolution¹⁰. SEM combined with energy-dispersive x-ray spectroscopy (EDS or EDX), also known as SEM-EDX, uses emitted X-rays from the sample to show the material's elemental composition. In addition, SEM combined with a focused ion beam (FIB), also

called SEM-FIB, uses an ion beam instead of an electron beam. This ion beam is usually made up of gallium ions and can directly modify the sample's surface (with nanometer precision) via sputtering¹².

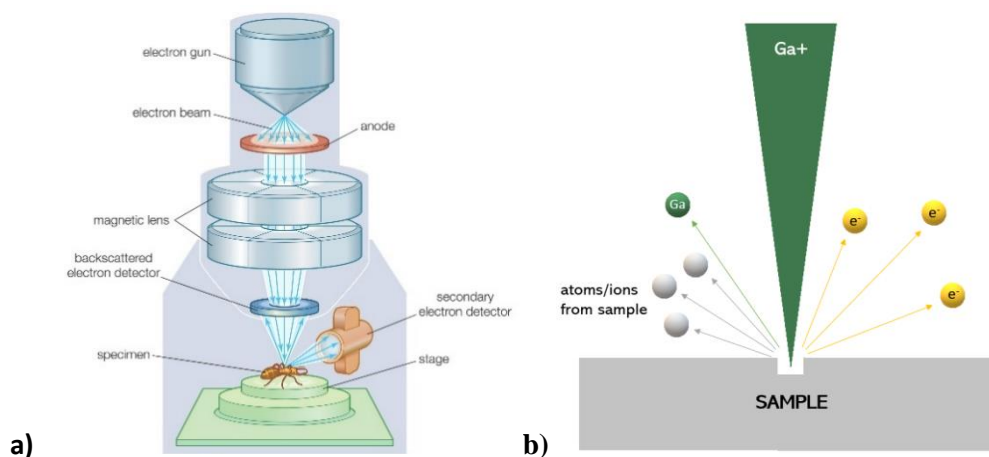


Figure 2.4: a) Schematic illustration of SEM showing the origin of electron beam, backscatter, and secondary electron detector. Image was obtained from Ref [13]. b) Diagram of gallium ions milling the surface of a sample, and the production of secondary electrons which can be used for imaging. Reproduced from Ref. [13].

2.2.3 Atomic Force Microscopy (AFM)

AFM is a powerful high-resolution scanning probe microscope that can image 3D topography to give height information at the nanoscale and provide various types of surface measurements with minimum sample preparation¹⁴. AFM uses a sharp tip attached to a cantilever to scan over the sample surface line by line, when the tip approaches the surface, attractive forces between the surface and the tip make the cantilever deflect towards the surface¹³. On the other hand, when the tip contacts the surface, reflective forces deflect the cantilever away from the surface. By reflecting an incident laser beam off the top of the cantilever, these deflections will change the direction of the reflected beam, which is then measured using a position-sensitive photodiode¹⁵. In comparison to SEM, AFM does not need a vacuum and can provide height data. However, some disadvantages include its longer scan time and limitation of scan size to be in the micrometer scale instead of SEM's millimeter scale^{13,14}.

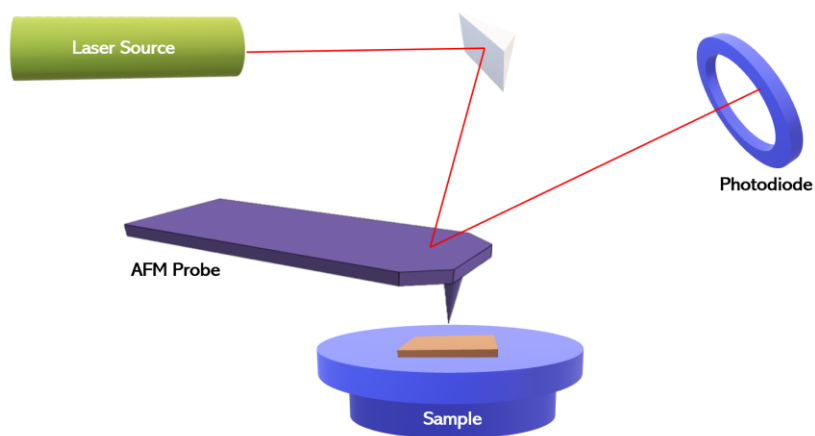


Figure 2.5: AFM scanning setup showing the how the laser light travels from the light source, bounces off the AFM probe and then hits the photodiode. Reproduced from Ref. [15].

AFM has three modes of operation, namely contact mode, tapping mode, and non-contact mode¹⁶. In contact mode, the tip contacts the surface, and a feedback circuit is used to adjust the probe height to maintain a constant force. This mode is fast but can damage the sample¹⁷. In non-contact mode, the cantilever oscillates slightly above the resonant frequency and comes near the surface but does not make contact. This mode applies minimal force to the sample, so it is good to use for very soft samples, but this results in very low scan speeds^{16,17}.

On the other hand, in tapping mode, the cantilever oscillates at or below its resonant frequency. It maintains an oscillation amplitude in the range of 20 to 100nm¹⁶. Here frequency and amplitude of the driving signal are kept constant. Therefore, forces like van der Waals change the amplitude when the tip comes close to the surface¹⁷. Consequently, a feedback circuit adjusts the probe height to maintain a constant amplitude of oscillation. Hence, tapping mode can be described as intermittent contact of the tip with the sample surface^{16,17,18}. This method was used for all imaging done in Chapter 4 as the low forces cause less damage to samples and the scan rates are not as slow as non-contact mode¹⁸.

2.3 References

1. Kasiviswanathan K.V. Hot Cells, Glove Boxes, and Shielded Facilities - Encyclopedia of Materials: Science and Technology. *Springer* **2001**, 3830-3833.
2. The Schlenk Line Survival Guide. 2021. <https://schlenklinesurvivalguide.com/>
3. Keeler, J. Understanding NMR spectroscopy. *John Wiley & Sons* **2011**.
4. Hiraoka, K. ed. Fundamentals of mass spectrometry. *Springer* **2013**, 8, 145.
5. Derome, A.E. Modern NMR techniques for chemistry research. *Elsevier* **2013**, 1-8.
6. Chemistry LibreTexts.NMR Spectroscopy. 2021: [https://chem.libretexts.org/Courses/University_of_Illinois_Springfield/Introduction_to_Organic_Spectroscopy/5%3A_Proton_Nuclear_Magnetic_Resonance_Spectroscopy_\(NMR\)/5.03%3A_NMR_Spectroscopy](https://chem.libretexts.org/Courses/University_of_Illinois_Springfield/Introduction_to_Organic_Spectroscopy/5%3A_Proton_Nuclear_Magnetic_Resonance_Spectroscopy_(NMR)/5.03%3A_NMR_Spectroscopy)
7. Herbert, C.G.; Johnstone, R.A. Mass spectrometry basics. *CRC press* **2002**, 1-16.
8. Mass Spectrometry and Mass Flow Control; A closer ion them. Bronkhorst. **2021** <https://www.bronkhorst.com/en-us/blog-en/mass-spectrometry-and-mass-flow-control-a-closer-ion-them/>
9. Maccoll, A. Mass Spectrometry, Historical Perspective. Elsevier **1999**, 1241-1248.
10. Ul-Hamid, A. A Beginners' guide to scanning electron microscopy. *Springer International Publishing* **2018**, 1, 402.
11. Akhtar, K.; Khan, S.A.; Khan, S.B.; Asiri, A.M. Scanning electron microscopy: Principle and applications in nanomaterials characterization - Handbook of materials characterization. *Springer*, **2018**, 113-145.
12. Nanoscience Instruments. *Scanning Electron Microscopy - Nanoscience Instruments*. 2021. <https://www.nanoscience.com/techniques/scanning-electron-microscopy/>
13. Encyclopedia Britannica. Scanning electron microscope | Definition, Images, Uses, Advantages, & Facts. 2020. <https://www.britannica.com/technology/scanning-electron-microscope>
14. Giessibl, F.J. Advances in atomic force microscopy. *Reviews of modern physics* **2003**, 75, 949.

15. Zeng, G.; Duan, Y.; Besenbacher, F.; Dong, M. Nanomechanics of amyloid materials studied by atomic force microscopy. *Atomic Force Microscopy Investigations into Biology-From Cell to Protein* **2012**.
16. Hölscher H. AFM, Tapping Mode. Encyclopedia of Nanotechnology. *Springer* **2012**.
17. Trache, A.; Meininger, G.A. Atomic force microscopy (AFM). *Current Protocols in Microbiology* **2008**, 8, 2C-2.
18. J Roa, J.; Oncins, G.; Diaz, J.; Sanz, F.; Segarra, M. Calculation of Young's modulus value by means of AFM. *Recent Patents on Nanotechnology* **2011**, 5, 27-36.

Chapter 3

3 Developing 2D Polyphenylene Membranes

3.1 Introduction

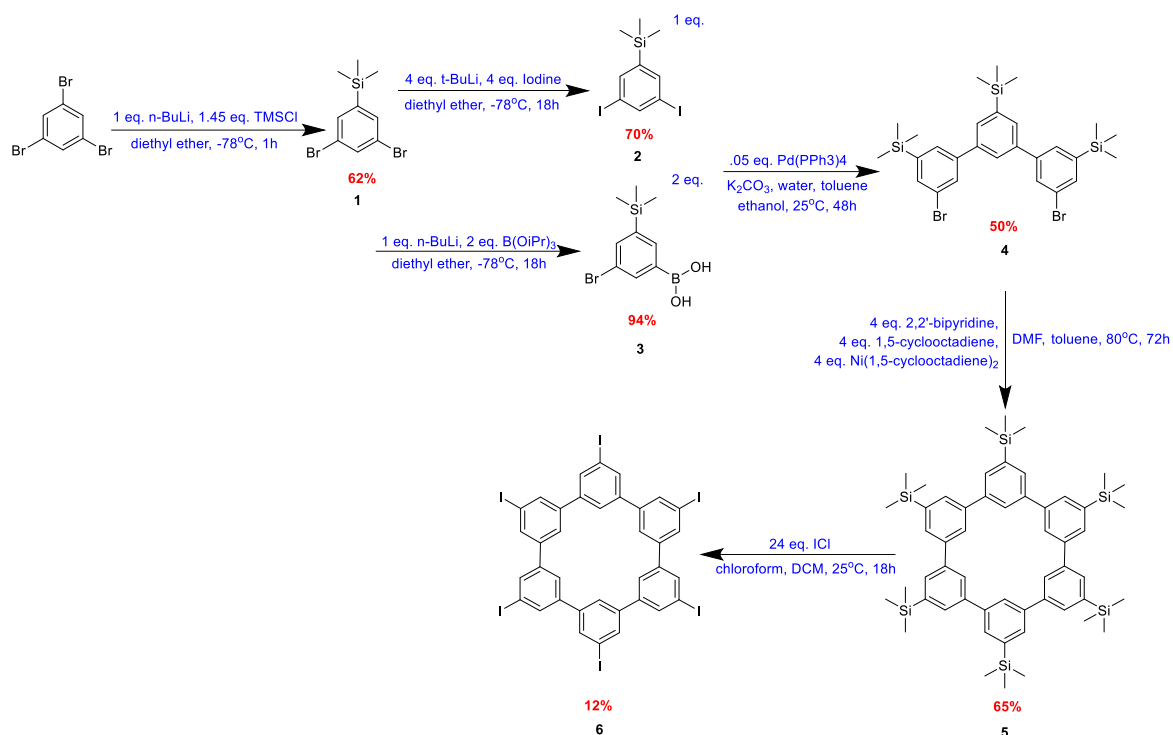
This project aimed to develop membranes made from 2D polyphenylene, also known as porous graphene, and perform the first experiments to measure fluid flow rates through sub-nanometer pores of known structures in an atomically thin material. Unlike graphene, single layers of 2D polyphenylene are not commercially available; therefore, the first phase of my research project involved the synthesis of this material. Covalent 2D polyphenylene networks form by crosslinking hexaiodo-substituted cyclohexa-m-phenylene (CHP), which happens by silver-promoted aryl-aryl coupling under ultrahigh vacuum conditions^{1,2}. Moreover, synthesis of the CHP monomer is a multi-step process³, which is explained thoroughly in Section 3.2. As of 2020, this procedure was the only way to synthesize 2D polyphenylene, and there is a need to develop a more straightforward method to make bulk production possible³.

Though the CHP monomer was successfully synthesized in the end; synthesis of the material was and continues to be suspended as a thermal evaporator⁴ with the required conditions was not available due to pandemic restrictions and new operating policies, further delaying the progress of this project. In the next section, I discuss the multi-step synthesis of the CHP monomer. I discuss the reaction mechanisms, challenges faced, and how they were overcome for each step – in detail.

3.2 Synthesis of Hexaiodo-substituted cyclohexa-m-phenylene (CHP)

A Schlenk line was used to perform each reaction under an air and moisture free environment, since the dual manifold of a Schlenk line allows connection to a purified inert gas (argon) and a vacuum pump⁵. After each reaction, the synthesized products were concentrated in vacuo using a rotary evaporator and allowed to crystallize overnight in the fridge. The products were dissolved in deuterated chloroform (CDCl_3), dichloromethane (CD_2Cl_2), or acetone ($(\text{CD}_3)_2\text{CO}$) and then submitted to NMR (Bruker Avance III HD 400)

spectrometer to obtain ^1H and ^{13}C NMR. The NMR spectra were then analyzed using a spectral data analysis software named Mestre Nova.



Scheme 1: Synthesis of hexaiodo-substituted cyclohexa-m-phenylene (CHP).

3.2.1 Synthesis of 1,3-dibromo-5-(trimethylsilyl)benzene

In this step, commercially available 1,3,5-tribromobenzene (Millipore-Sigma, 98%, CAS 626-39-1) is being converted into **1**. To achieve this, one of the bromines on benzene undergoes a halogen-metal exchange, wherein n -butyllithium [$n\text{-BuLi}$] (Millipore-Sigma, CAS 109-72-8, 1.6 M in hexanes) performs a nucleophilic attack on bromine to make an organolithium⁶. This occurs because the resulting organolithium has a pK_a of 43 [Ref 7], which is less basic and more stable than starting butyllithium with a pK_a of 50 [Ref 8]. To ensure $n\text{-BuLi}$ only attacks one of the bromines, and not all the bromines on the benzene, slow-addition and cold temperatures are used to slow down the reaction. Thus, the probability of the same molecule being attacked more than once decreases. Next, chlorotrimethylsilane (Millipore-Sigma, >99%, CAS 75-77-4) is slowly added to the mixture, where the double bond on the lithiated side of the benzene then promotes a nucleophilic substitution reaction by attacking the electrophilic chlorotrimethylsilane,

making chlorine leave and pair with lithium to form lithium chloride⁹. The general purpose of synthesis in this step was to protect one of the reactive sites of the benzene with a trimethylsilyl (TMS) protecting group so that the other sites can be manipulated while keeping this site unreacted¹⁰. This site can be easily deprotected when needed and will be seen in Section 3.2.6.

The initial synthesis procedure was obtained from Gong et al., where 2.6 M n-BuLi dissolved in tetrahydrofuran (THF) was added to the commercially available 1,3,5-tribromobenzene (1:1 molar ratio)¹¹. It was expected that this would produce needle-like crystals, but it produced a viscous dark-brown liquid. The NMR Spectroscopy (Fig. 3.1 top) also shows multiple peaks representing impurities and minimal signs of product. It appears that due to a high concentration of n-BuLi (2.6 M), multiple sites were lithiated, resulting in undesired product formation. Therefore, Ye et al.'s modified version of the procedure was tested¹² – though instead of a 1:2 molar ratio between the starting material and the low concentration n-BuLi (1.6 M), a 1:1 molar ratio was maintained. This procedure was successful and produced the desired product but also other impurities. Surprisingly after 24 hours in the fridge, needle-like crystals formed, separating from the produced dark-yellow liquid mixture. NMR spectroscopy (Fig. 3.1 bottom) showed that the needle-like crystals were a pure form of the product, whereas the leftover liquid had impurities. To further clean these crystals, they were washed with cold methanol, yielding white needle-like crystals. In addition, it was found that the reaction reaches completion within 1 hour and does not have to be stirred overnight.

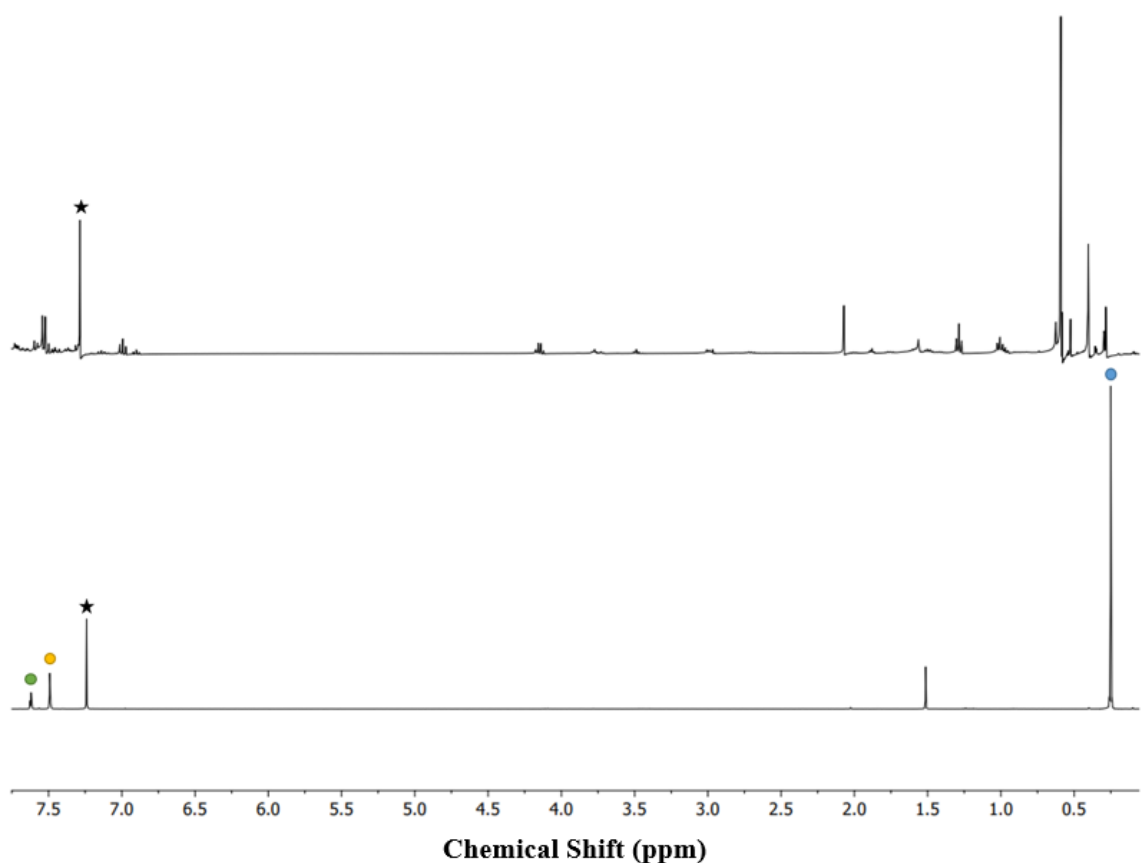
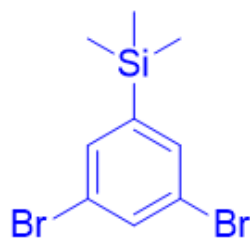


Figure 3.1: (top) ^1H NMR spectra of **1** using procedure by Gong et al.¹¹, showing multiple impurities and minimal product (bottom) ^1H NMR spectra of purified **1** using a modified version of Ye et al.¹², where ● are signals from aryl group, ● TMS protecting group and ★ chloroform solvent peak.

Experimental Procedure



1,3,5-tribromobenzene (12.0 g, 38 mmol) was dissolved in anhydrous diethyl ether (250 mL) and cooled to -78°C in a 500 mL round-bottom flask. To this solution, n-BuLi (15 mL, 38 mmol, 1.6 M in hexane) was added dropwise, and the solution was stirred for 30 min. Then, chlorotrimethylsilane (7 mL, 55 mol) was added dropwise over about 10 min. The solution was warmed to room temperature and stirred for 1 hour. Water (15 mL) was added to the solution, and the organic layer was separated and washed with brine then dried over magnesium sulfate. The removal of solvent gave white needle-like crystals (Appendix 3), which were further washed with cold methanol (yield 7.23 g, 62%). ^1H NMR

(CDCl₃, 400 MHz) δ 7.64 (1H, t), 7.51 (2H, d), 0.27 (9H, s). ¹³C NMR (CDCl₃, 100 MHz) δ 146.1, 134.5, 134.2, 123.2, -1.35.

3.2.2 Synthesis of 1,3-diiodo-5-(trimethylsilyl)benzene

In this step, **1** is being converted into 1,3-diiodo-5-(trimethylsilyl)benzene. Like step 1, bromine undergoes a halogen-metal exchange to make an organolithium⁶. Similar to n-BuLi, a strong base like tert-butyllithium (also known as T-BuLi) is used to perform a nucleophilic attack on bromine as selectivity is not an issue and the nucleophilic attack occurs on both bromines. T-BuLi (Millipore-Sigma, CAS 594-19-4, 1.7 M in pentane) is extremely reactive and can degrade quickly in ether solvents; therefore, these reactions are conducted at very low temperatures¹³. After lithiation, an iodine solution is added to the mixture, where again, the double bond on the benzene promotes a nucleophilic substitution reaction by attacking the electrophilic iodine bond⁹. The attack pushes out one of the iodine, which then pairs with lithium to form lithium iodide. This repeats until both lithiated sides have been substituted with iodine. The purpose of this step is to make a R-halogen (X) compound that will be later used in 3.2.4 for a Suzuki cross-coupling reaction¹⁴. Pisula et al.'s procedure was used to synthesize **2** successfully (Fig. 3.2)³.

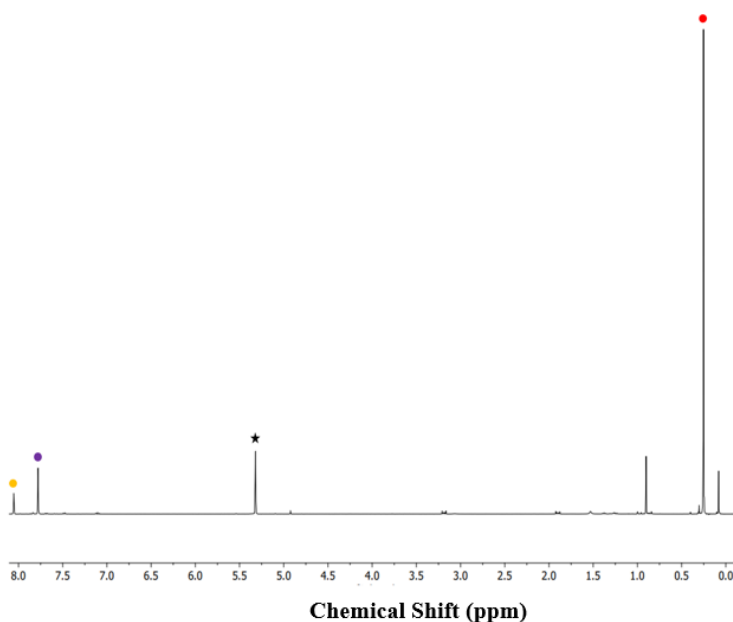
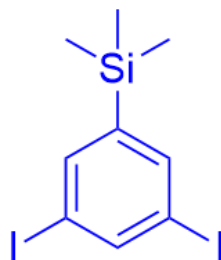


Figure 3.2: ¹H NMR spectra of purified **2**, signal indication: ● aryl group, ● TMS protecting group and ★ dichloromethane solvent peak.

Experimental Procedure



1,3-Dibromo-5-(trimethylsilyl) benzene (2.10 g, 6.8 mmol) was dissolved in anhydrous diethyl ether (70 mL) and cooled to -78°C in a 250 mL round bottom flask. To this solution, T-BuLi (16 mL, 27 mmol, 1.7 M in pentane) was added dropwise, and the solution was stirred for 30 min. After which, the reaction was brought to room temperature and stirred for an additional hour. Then, a mixture containing iodine (7.2 g, 28 mmol) and diethyl ether (40 mL) was slowly added to the solution. The reaction was then stirred overnight at room temperature. The organic phase was washed with water, aqueous sodium bisulfite, and ammonium chloride, then dried with magnesium sulfate. After solvent removal, the obtained product was filtered over a silica column with hexanes, and a yellow crystalline material (Appendix 4) was obtained (yield 1.88 g, 70%). ^1H NMR (CD_2Cl_2 , 400MHz) δ 8.05 (t, 1H), 7.77 (d, 2H), 0.25 (s, 9H). ^{13}C NMR (CD_2Cl_2 , 100MHz) δ 147.0, 145.3, 141.0, 96.0, -1.7.

3.2.3 Synthesis of 3-bromo-5-(trimethylsilyl)phenylboronic acid

In this step, **1** is converted into 3-bromo-5-(trimethylsilyl)phenylboronic acid. Here, *n*-BuLi selectively lithiates one of the bromines via a halogen-metal exchange at very cold temperatures⁶. After which, the double bond on the benzene attacks the boron on triisopropyl borate (Millipore-Sigma, 98%, CAS 5419-55-6) and breaks an ester bond¹⁵. The intermediate is stable until hydrochloric acid (HCl) is added to the solution, where the chlorine nucleophile attacks the carbon (linked to the oxygen), breaking the carbon-oxygen bond. The neighboring hydrogen bonds stabilize the oxygen and form boronic acid. This step is a crucial component to the Suzuki cross-coupling reaction¹⁴ presented in Section 3.2.4.

Pisula et al.'s procedure was used to synthesize **3**, where certain modifications were made to maximize yield and minimize impurities³. In the initial synthesis, after adding *n*-BuLi, the solution was stirred at room temperature. However, as the quantities used in this test reaction were small, the reaction reached equilibrium quickly, encouraging undesired side reactions such as lithiation of both sides. To prevent this, the temperature was maintained

at -78°C until all the reagents were added and then it was slowly warmed to room temperature. In addition, the obtained amorphous solid was washed with water and hexanes to clean the product further (Fig. 3.3).

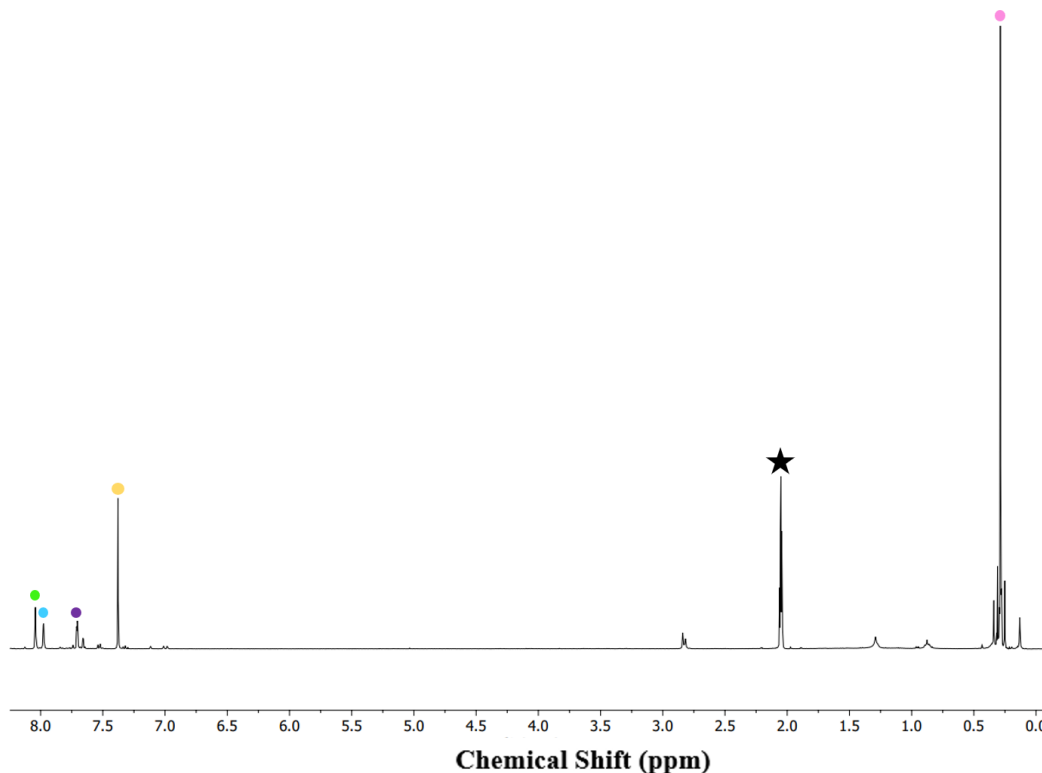
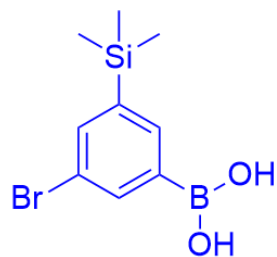


Figure 3.3: ^1H NMR spectra of cleaned **3**, signal indication: ●●● aryl group, ● boronic acid, ● TMS protecting group and ★ acetone solvent peak.

Experimental Procedure



1,3-Dibromo-5-(trimethylsilyl) benzene (8.0 g, 26 mmol) was dissolved in anhydrous diethyl ether (120 mL) and cooled to -78°C in a 250 mL round-bottom flask. To this solution, *n*-BuLi (16 mL, 26 mmol, 1.6 M in hexane) was added dropwise, and the solution was stirred for 1 hour. Then, tri-isopropyl borate (12 mL, 52 mmol) was quickly added, and the mixture was slowly warmed to room temperature and stirred overnight. The reaction was stopped by adding 10% aqueous HCl. The organic phase was separated, washed with water, and dried with magnesium sulfate. After solvent removal, a white amorphous solid (Appendix 5) was obtained, which was further washed with water and

hexanes (yield 6.65 g, 94%). $^1\text{H NMR}$ ($[\text{D}_6]$ acetone, 400 MHz) δ 8.06 (1H, t), 7.98 (1H, dd), 7.70 (1H, d), 7.38 (2H, s), 0.29 (9H, s).

3.2.4 Synthesis of 5,3''-dibromo-3,5',5''-tris-trimethylsilyl-1,1';3',1''-terphenyl (m-terphenyl derivative)

In this step, **2** and **3** are coupled to make a m-terphenyl derivative. It utilizes the Suzuki cross-coupling catalytic cycle, which couples a boronic acid and an organohalide using a palladium (0) catalyst and a base¹⁶. Compared to other cross-coupling reactions, Suzuki coupling reactions are preferred because they are relatively mild, and their reagents are easy and inexpensive to prepare¹⁷. The catalytic cycle involves three main steps, namely oxidative addition, transmetalation, and reductive elimination. In the oxidative addition step, an organohalide couples with the palladium catalyst (Tetrakis(triphenylphosphine)palladium (0), Millipore-Sigma, 99% CAS 14221-01-3), which undergoes oxidation from palladium (0) to palladium (II)¹⁶. This forms an organopalladium complex where a carbon-halogen bond is broken, and palladium inserts itself between the R group and the halogen. In the transmetalation, an organoborane reacts with the intermediate palladium (II) complex that formed after adding a base, resulting in a ligand transfer. Lastly, in reductive elimination, the palladium (II) complex eliminates the two R groups, and a carbon-carbon bond is formed while palladium (II) returns to palladium (0)^{16,17}. Pisula et al.'s procedure was used to successfully synthesize **4** (Fig. 3.5)³.

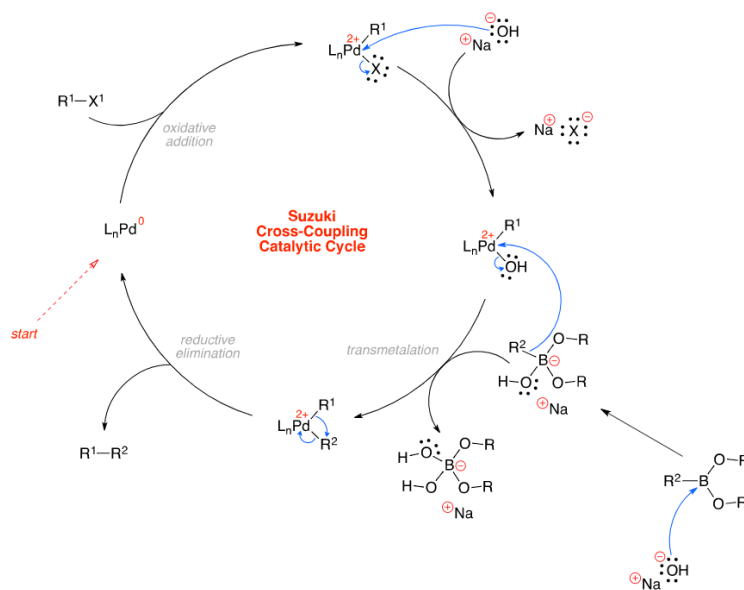


Figure 3.4: Catalytic cycle for a general Suzuki cross-coupling reaction, which was used for the synthesis of the m-terphenyl derivative. Obtained from Ref. [18].

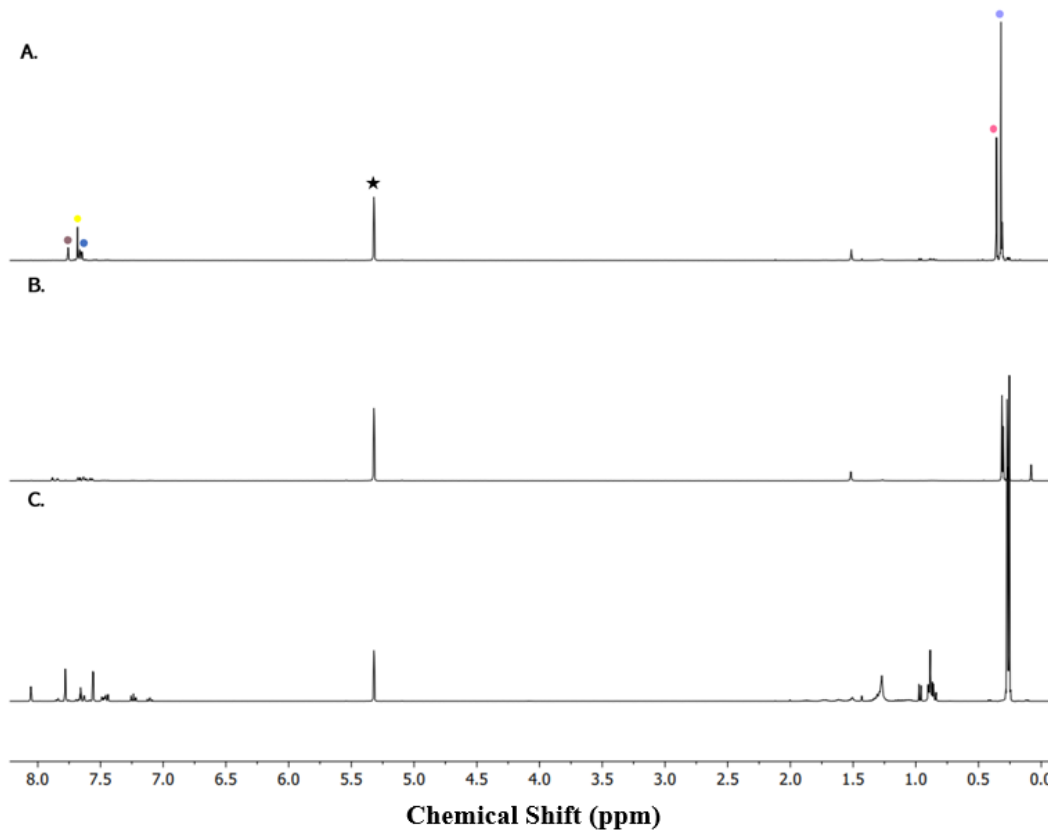
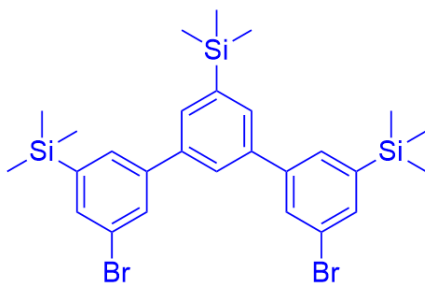


Figure 3.5: **A.** 1H NMR spectra of purified 4, signal indication: ●●● aryl group, ●● TMS protecting group and ★ acetone solvent peak. **B.** and **C.** 1H NMR spectra of undesired eluents obtained during column chromatography.

Experimental Procedure



3-Bromo-5-(trimethylsilyl) phenylboronic acid (1.36 g, 5 mmol), 1,3 diiodo-5-(trimethylsilyl) benzene (1.00 g, 2.5 mmol), and potassium carbonate (10.9 g) were dissolved in a mixture of toluene (82 mL), water (41 mL), and ethanol (6 mL) in a 250 mL round bottom flask. The solution was then degassed with Argon gas for 30 min. After which, Tetrakis(triphenylphosphine)palladium (0) (0.14 g, 0.1 mmol) was added and the mixture was stirred at room temperature for 48 hours. The organic phase was separated, washed with water, and dried with magnesium sulfate. After solvent removal, the residue was purified by preparative column chromatography (silica gel, hexane, $R_f = 0.4$) to obtain a colorless solid (1.0 g, 50%) (Appendix 6). ^1H NMR (400 MHz, CD_2Cl_2) δ 7.77 (dd, 2H), 7.69 (s, 3H), 7.67 (dd, 2H), 7.65 (dd, 2H), 0.36 (s, 9H), 0.32 ppm (s, 18H); ^{13}C NMR (75 MHz, CD_2Cl_2) δ 144.8, 143.3, 142.7, 140.5, 135.2, 132.0, 131.2, 130.9, 127.2, 123.4, -1.2.

3.2.5 Synthesis of 5,5',5'',5''',5''''-hexatrimethylsilylhexa-m-phenylene

In this step, **4** undergoes an aryl-aryl coupling with itself to make hexatrimethylsilylhexa-m-phenylene. This is possible due to Yamamoto coupling, where a carbon-carbon bond of aryl halogenide compounds forms via the mediation of transition metal complex bis(cyclooctadiene)nickel (0), also known as $\text{Ni}(\text{cod})_2$ (Millipore-Sigma, >95%, CAS 1295-35-8)¹⁹. The mechanism is shown in Fig. 3.6, with the main steps being oxidative addition, disproportionation, and reductive elimination²⁰. In the oxidative addition step, a halogen functionalized monomer couples with nickel (0), which undergoes oxidation to form a palladium (I) and (II) complex. The addition of 2,2'-bipyridine [BPY] (Millipore-Sigma, 99%, CAS 366-18-7), an auxiliary ligand, makes oxidative addition easier by forming a $\text{Ni}(\text{cod})(\text{BPY})$ complex²¹. After which, disproportionation of the two complexes of nickel occurs. In this type of reaction, two molecules of the same species react to give two different species²⁰. A polar solvent like DMF at 60-80 °C makes disproportionation easier and liberates BPY at room temperature²¹. Then, reductive elimination of nickel (III) complex leads to $\text{Ni}(0)$ regeneration and the desired product **5**. In the end, when aryl-aryl

bonds form, nickel is consumed, and thus, an excess of $\text{Ni}(\text{cod})_2$ is used to maximize the yield²⁰. Compared to other coupling mechanisms (such as Suzuki cross-coupling), Yamamoto coupling is a simple reaction that only requires a singly halogen functionalized monomer. Moreover, since the monomer lacks the flexibility to pack efficiently, this reaction can create sufficient free volumes and prepare ultra-high porosity solids¹⁹.

Pisula et al.'s procedure³ was used to synthesize **4**. Here 1,5-cyclooctadiene [cod] (Millipore-Sigma, >98%, CAS 1552-12-1) was added to stabilize the nickel transition complex. In the initial reactions, an incorrect amount of cod was used. The excess cod did not allow BPY to bind to the nickel transition complex, and thus, the reaction did not proceed. This issue was corrected, but the reaction still did not progress. As $\text{Ni}(\text{cod})_2$ is extremely sensitive to light, air, and water, extra precautions were taken²², such that it was only used in a glove box and covered with aluminum foil. It was suspected that DMF solvent had some water that could cause rapid degradation of the nickel complex, thus, DMF was dried over 4 Å molecular sieves (pellets, 1.6 mm diameter, Millipore-Sigma, CAS 70955-01-0) before use. Still, the reaction did not progress, so a longer approach that utilized the Suzuki cross-coupling reaction was attempted¹⁷.

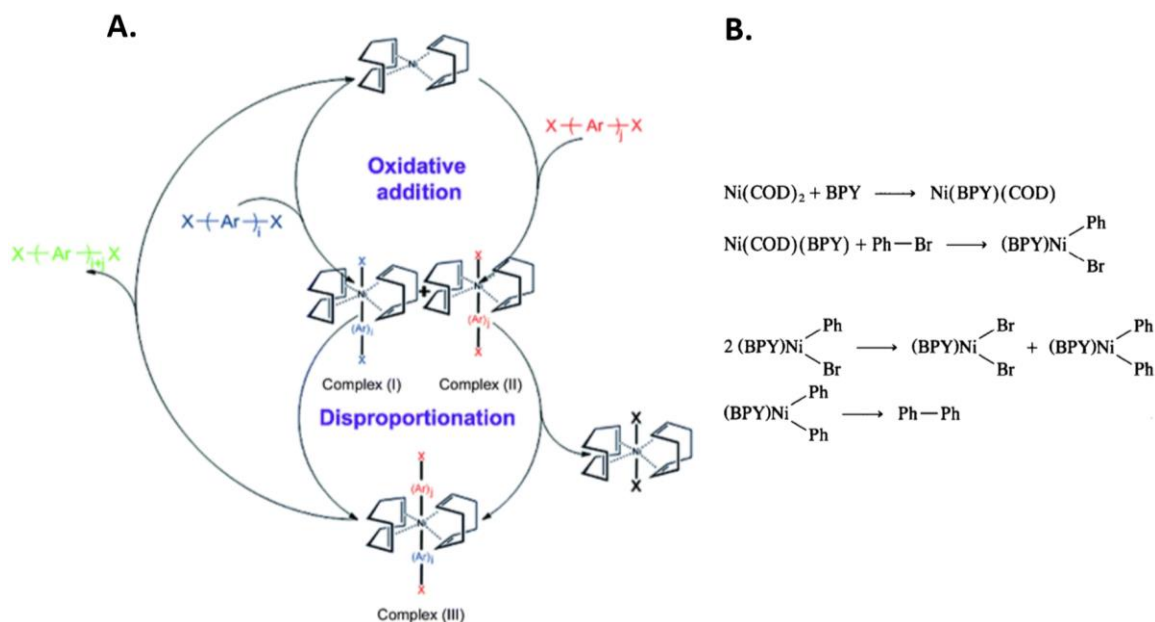
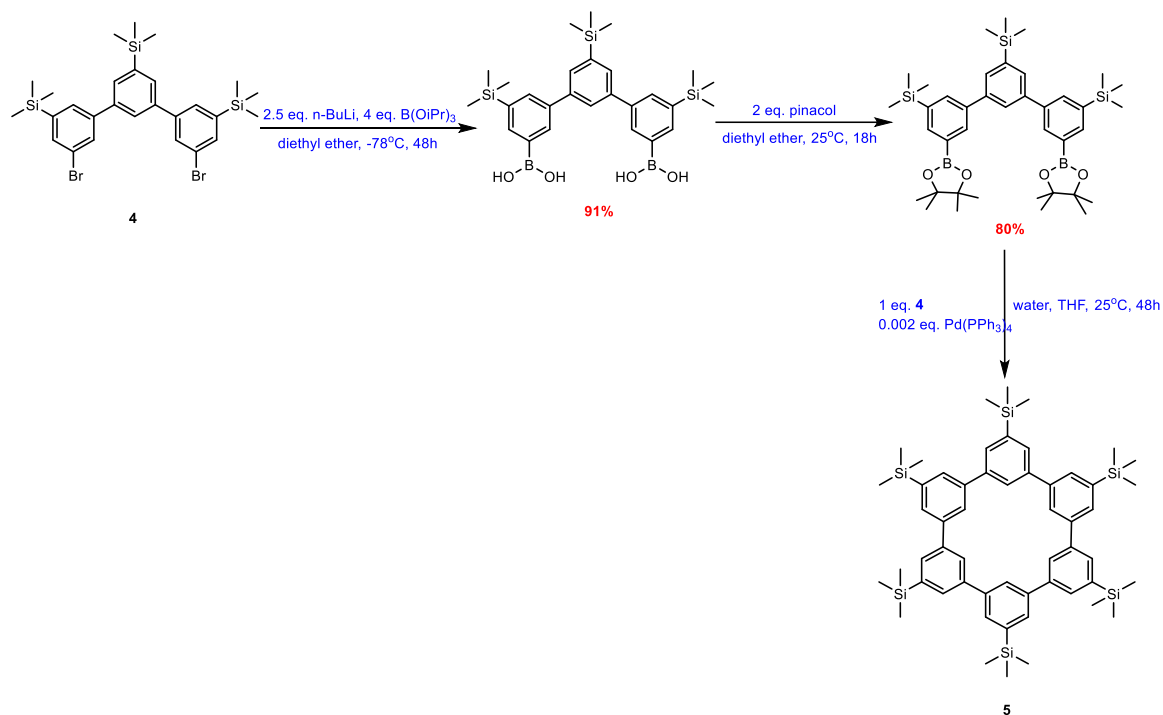


Figure 3.6: **A.** General reaction scheme for a Yamamoto coupling reaction used in the synthesis of hexatrimethylsilylhexa-*m*-phenylene. Republished with permission of Royal Society of Chemistry from Ref. [20]; permission conveyed through Copyright Clearance Center, Inc. **B.** Important intermediate steps in Yamamoto coupling, where Ph is a phenyl group. Reprinted from Ref. [21], Copyright 1992, with permission from Elsevier.

As mentioned earlier, the Suzuki cross-coupling reaction requires an organohalide and a boronic species. Since an organohalide has already been synthesized, some of that can be converted into a boronic ester. For these reactions, selecting the correct kind of boron reagent is essential to ensure that reaction progresses well. Boron reagents are usually assessed based on their nucleophilicity, and boronic acids and esters are commonly employed²³. Note that in 3.2.4, a boronic acid was used, but here a boronic ester is being used. Boronic acids are known to have enhanced reactivity and are highly susceptible to oxidation and protodeboronation; on the other hand, boronic esters are more stable and often used as replacements for unstable boronic acids²³.

Scheme 2 shows the alternate reaction scheme to synthesize hexatrimethylsilylhexa-*m*-phenylene. In the first step, boronic acid is synthesized using the procedure highlighted in Section 3.2.3. For the second step, boronic acids were converted into boronic esters using the procedure from Xie et al.²⁴ Under acidic conditions, oxygen on pinacol conducts a nucleophilic attack on the hydrogen on the boronic acid, yielding water²⁵. Thus, water becomes a leaving group, and the pinacol intermediate stabilizes the oxygen on the boron.

This process repeats on both sides until both acidic sites have been replaced, forming a boronic ester. As water is the only leaving group, this process can be easily reversed with the addition of water²⁶. In the last step, Suzuki coupling (like in Section 3.2.4) can be used to produce **5**.



Scheme 2: Alternate reaction scheme to synthesize hexatrimethylsilylhexa-m-phenylene by converting some of **4** to a boronic ester and then cross-coupling the two.

Boronic acid species of *m*-terphenyl derivative were successfully synthesized. However, the initial reaction was stirred for two days, and ¹H NMR in solvent CD₂Cl₂ (Fig. 3.7C) showed the formation of more impurities, which made it difficult to assess product formation. The reaction time was then reduced to overnight instead of two days, and the ¹H NMR in solvent CD₂Cl₂ showed fewer impurities (Fig. 3.7B), but it was still difficult to see if any product had formed. Conducting ¹H NMR in solvent CDCl₃ (Fig. 3.7A) caused a shift in the impurities and made the boronic acid peak more visible. Other procedures also confirmed their boronic acid peak using CDCl₃ as their solvent^{27,28}.

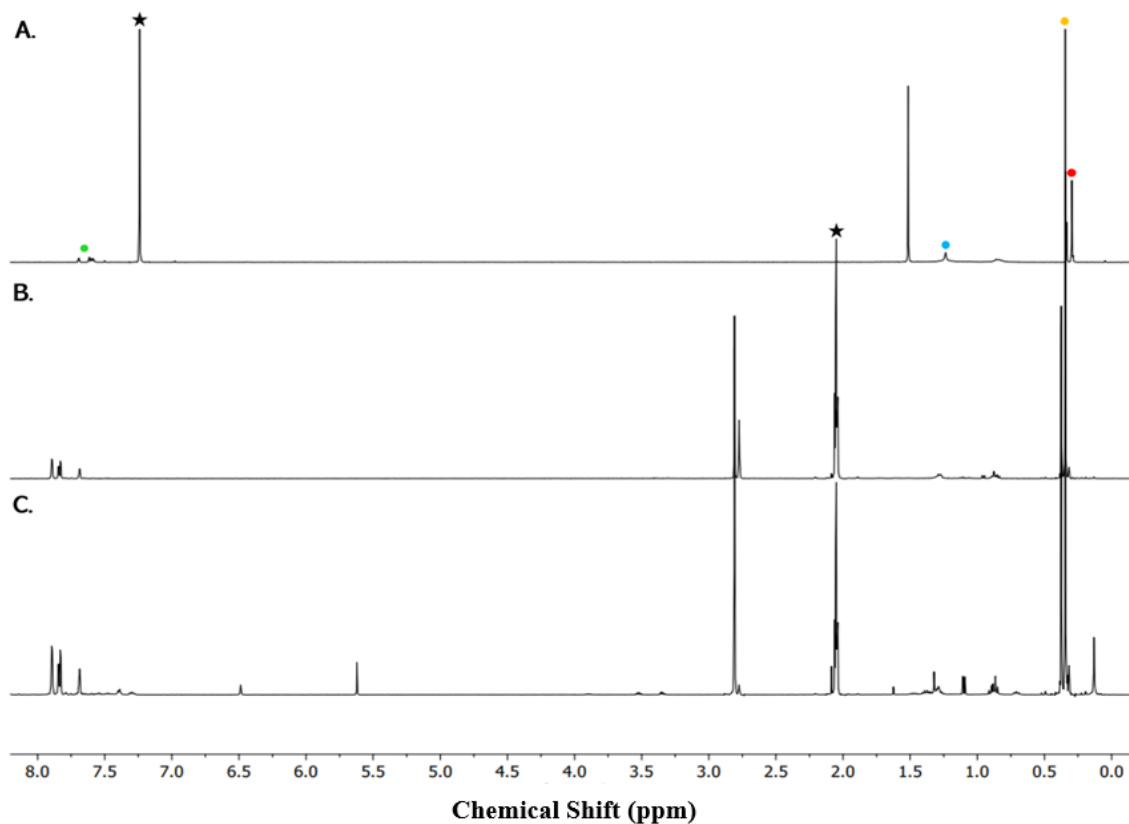


Figure 3.7: **A.** ^1H NMR spectra in CDCl_3 showing the formation of boronic acid species, signal indication \bullet aryl group, \bullet TMS protecting group, \bullet boronic acid, and \star solvent. **B.** ^1H NMR spectra in CD_2Cl_2 after stirring overnight (less impurities) **C.** ^1H NMR spectra in CD_2Cl_2 after stirring for two days (more impurities).

Boronic esters were successfully synthesized (Fig. 3.8) using the procedure from Xie et al.²⁴ As mentioned before, this reaction can be easily reversed by adding water. In this reaction, water is being produced as a leaving group, making it difficult to form the product. A water quencher was needed to solve this problem, and thus 4 Å molecular sieves were used to quench any water that formed during the reaction. The difference in product formation with and without molecular sieves can be seen in Fig. 3.9. The last step was attempted again with Suzuki cross-coupling instead of Yamamoto coupling. However, the reaction still did not progress. This could be due to water formation and the reaction going backward, but more investigation is needed to assess the problems with this reaction²⁶.

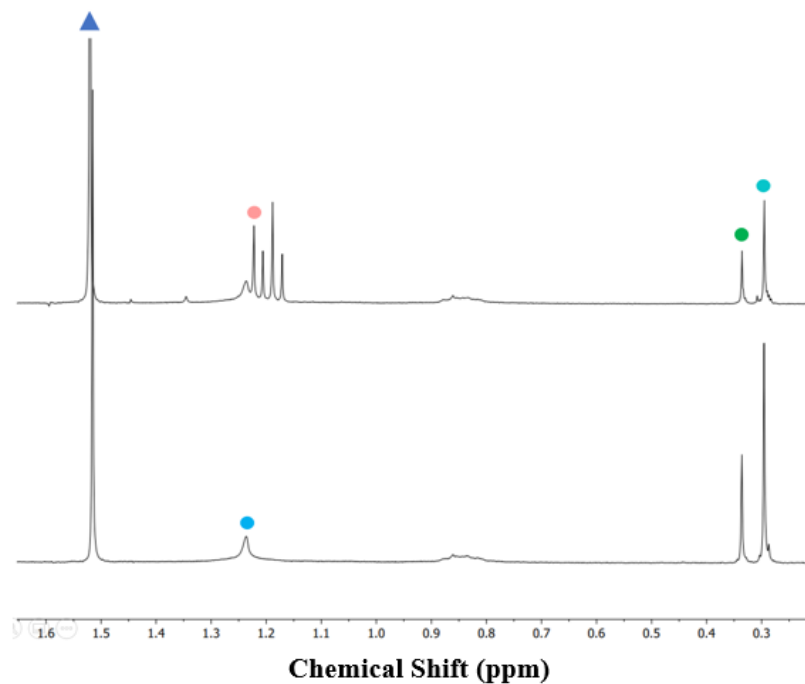


Figure 3.8: (top) ^1H NMR spectra of the boronic ester species, signal indication \blacktriangle water, $\bullet\bullet$ TMS protecting group, and \bullet boronic ester (bottom) ^1H NMR spectra of boronic acid species, where \bullet is boronic acid.

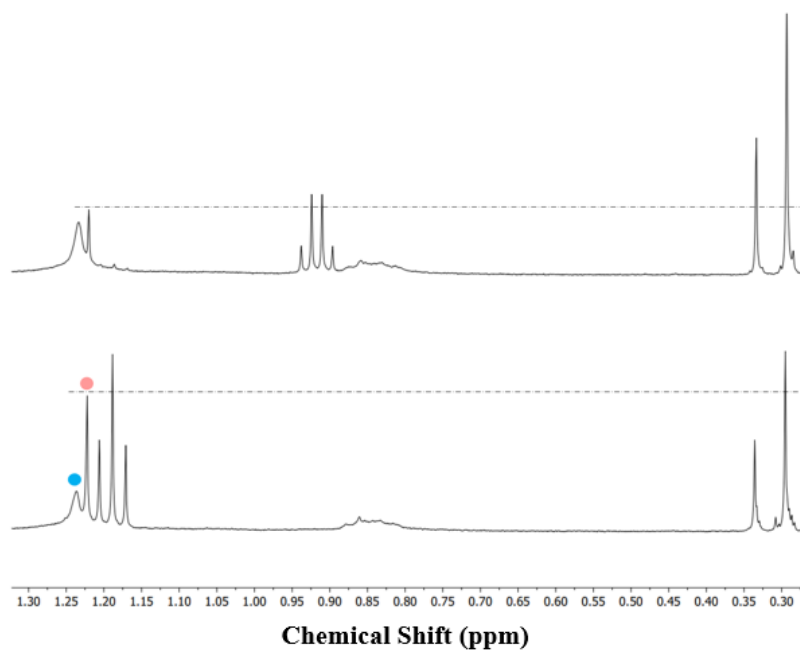


Figure 3.9: (top) ^1H NMR spectra of the boronic ester species without molecular sieves, where the dashed line shows very little product formation. (bottom) ^1H NMR spectra of the boronic ester species with molecular sieves, shows more product formation. Signal indication \bullet boronic acid, and \bullet boronic ester.

Meanwhile, the original Yamamoto cross-coupling reaction was attempted again, with most of the steps being done inside the glove box. Extra precautions were taken while handling the nickel complex (such as dark surroundings), leaving no possibility of a leak during the transfer to the Schlenk flask. This ensured the successful formation of **5** (Fig. 3.10).

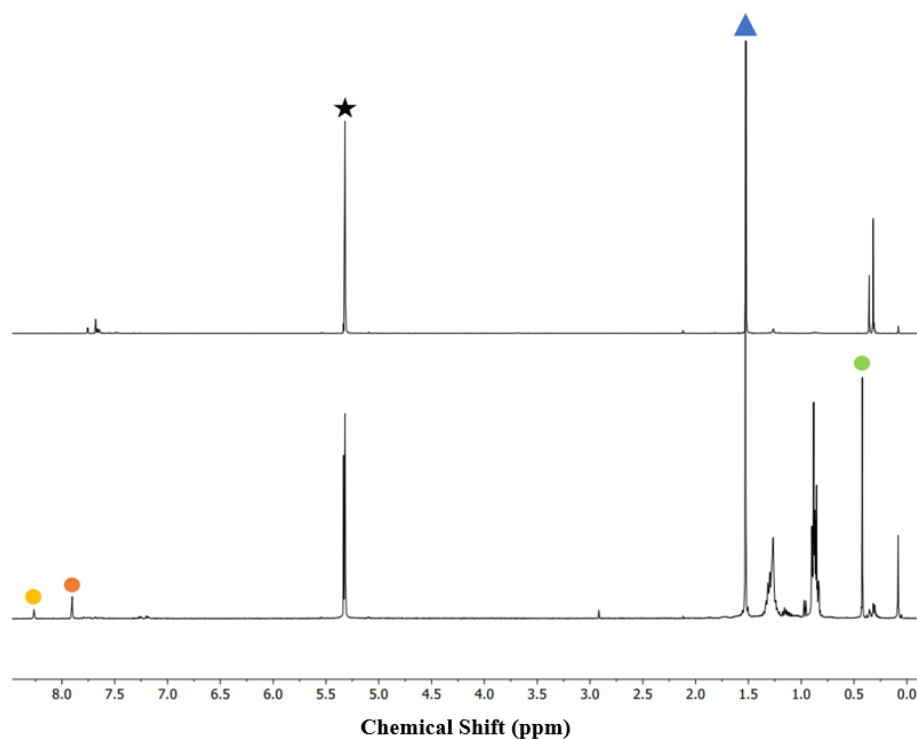
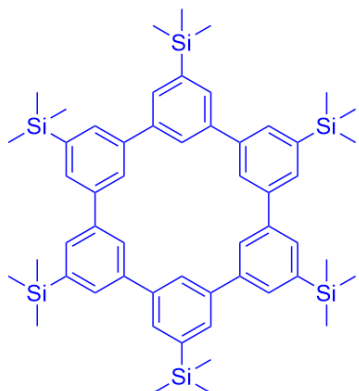


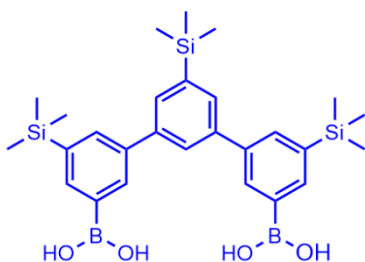
Figure 3.10: (top) ^1H NMR spectra of the alternative synthesis route using Suzuki coupling. (bottom) ^1H NMR spectra of the main synthesis route using Yamamoto coupling and the successful formation of **5**. Signal indication \bullet aryl group, and \bullet TMS protecting groups.

Experimental Procedure

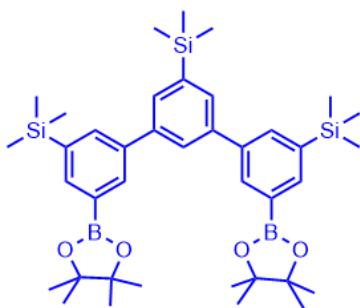


2,2'-bipyridine (52 mg, 0.33 mmol), 1,5-cyclooctadiene (36 mg, 0.33 mmol, 40 μL) and $\text{Ni}(1,5\text{-cyclooctadiene})_2$ (91 mg, 0.33 mmol) were dissolved in anhydrous N,N-dimethylformamide (DMF; 4 mL) and stirred for 30 min at 80°C in the absence of light. A solution of 5,3''-dibromo-3,5',5''-tris-trimethylsilyl-1,1';3',1''-terphenyl (50 mg, 8.3 mmol) in dry and degassed toluene (18 mL) was added

quickly. and the resulting mixture was stirred for three days at 80°C. The reaction was stopped by adding 10% aqueous HCl (1 mL). The organic phase was separated, washed with water, and dried with magnesium sulfate. After solvent removal, the residue was purified with preparative column chromatography (silica gel, petroleum ether, dichloromethane = 11:1; R_f = 0.4) to obtain a colorless solid (48 mg, 65%). ¹H NMR (400 MHz, CD₂Cl₂) δ 8.28 (s, 6H), 7.92 (s, 12H), 0.43 ppm (s, 54H); ¹³C NMR (175 MHz, CD₂Cl₂) δ 142.6, 141.3, 130.9, 128.5, -0.9 ppm.



M-terphenyl derivative (0.1 g, 0.2 mmol) was dissolved in diethyl ether (1 mL) and cooled to -78°C. To this solution, N-BuLi (0.26 mL, 0.4 mmol, 1.6 M in hexane) was added dropwise, and the reaction mixture was stirred for 1 hour. After which, triisopropyl borate (0.15 mL, 0.7 mmol) was added quickly, and then the reaction was slowly warmed to room temperature overnight. The reaction was stopped by adding 10% aqueous HCl, and the organic phase was washed with water and dried with magnesium sulfate. After solvent removal, a white amorphous solid was obtained, which was further washed with water and hexanes (yield 0.08 g, 91%). ¹H NMR (CDCl₃, 400 MHz) δ 7.69 (dd, 2H), 7.62 (s, 3H), 7.60 (dd, 2H), 7.58 (dd, 2H), 1.24 (s, 4H), 0.34 (s, 9H), 0.30 ppm (s, 18H).



Boronic acid species of m-terphenyl derivative (0.05 g, 0.1 mmol) and pinacol (0.02 g, 0.2 mmol) were added to a flask with 4 Å molecular sieves and dried diethyl ether (10 mL). The reaction mixture was stirred overnight and filtered through a short pad of celite, and the filtrate was condensed under vacuo to obtain a white solid (yield 0.049 g, 80%) ¹H NMR (CDCl₃, 400 MHz) δ 7.69 (dd, 2H), 7.62 (s, 3H), 7.60 (dd, 2H), 7.58 (dd, 2H), 1.22 (s, 24H), 0.34 (s, 9H), 0.30 ppm (s, 18H).

3.2.6 Synthesis of 5,5',5'',5''',5''''',5''''''-hexaiodohexa-m-phenylene

In this step, the TMS groups on **5** were converted to hexaiodohexa-m-phenylene (monomer of 2D polyphenylene) using iodomonochloride (Millipore-Sigma, >95%, CAS 7790-99-0)

in an ipso substitution. In ipso substitution, benzene acts as a nucleophile and attacks iodine (strong electrophile) to form a charged intermediate²⁹. The electronegative chlorine then attacks the silicon, forming trimethylsilyl chloride, a leaving group. This is followed by the elimination of the leaving group and regeneration of the aromatic ring^{29,30}. The step aimed to remove all the TMS groups and replace them with reactive iodine, which aids in the synthesis of the polymer. Pisula et al.'s procedure³ was used to synthesize **6** successfully (Appendix 7). Since **6** is sparingly soluble, the NMR spectrum or mass spectrum could not be obtained. To perform elemental analysis, an amount greater than 10 mg – which was more than the yield – was needed to get an accurate measurement. In addition, combining the yield from different reactions would introduce impurities. Therefore, SEM-EDS analysis was performed. In this way, a trace amount of material was used. The elemental spectrum (Fig. 3.11) shows a greater presence of iodine, which points towards product formation. Other elements like silicon and chlorine are present in the trace, which is expected as trimethylsilyl chloride is the side product (leaving group). Note that the ratio of carbon to iodine could not be compared as the sample is placed on carbon tape for SEM analysis, skewing the ratio significantly.

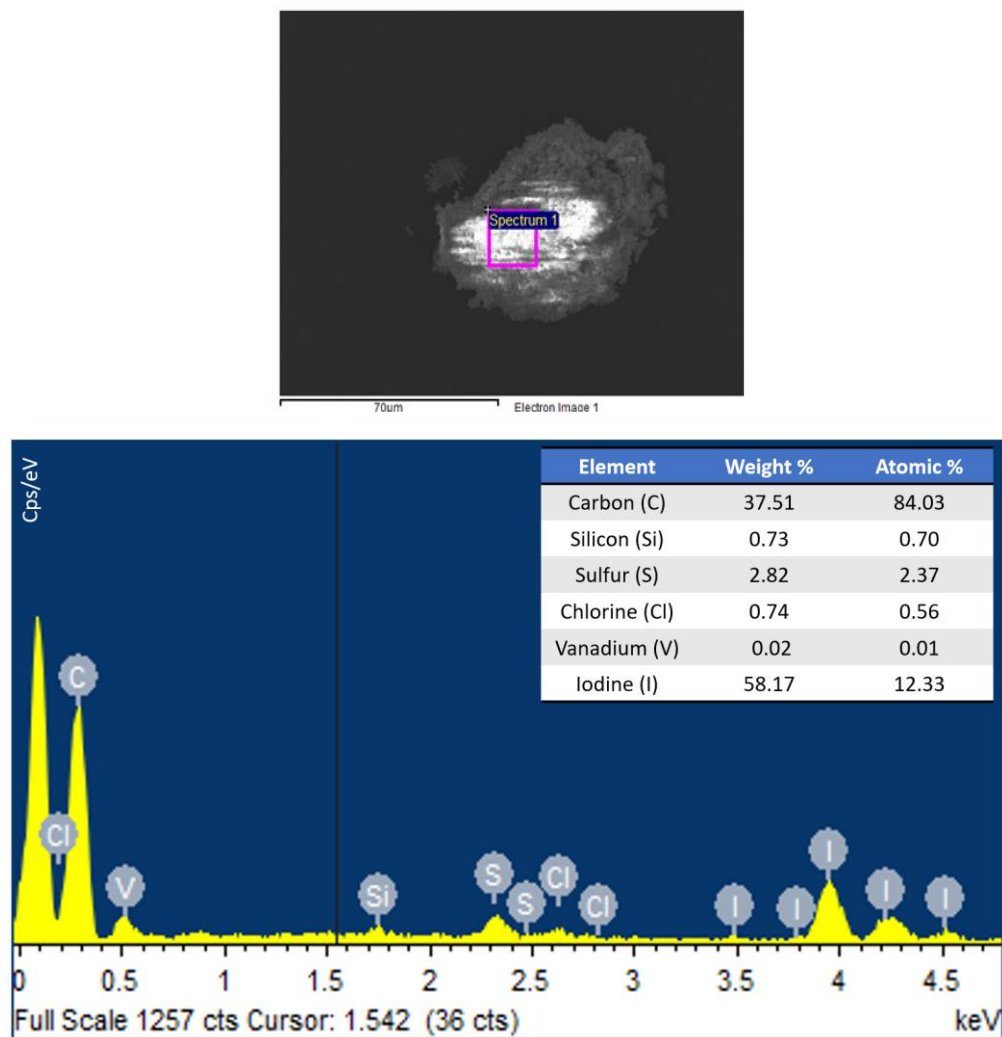
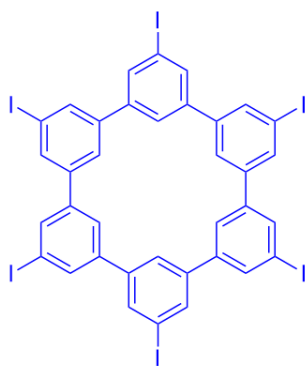


Figure 3.11: (top) SEM image of the particle analyzed. (bottom) Elemental spectrum obtained from the X-ray detector with the weight and atomic % values for each element present in the inset.

Experimental Procedure

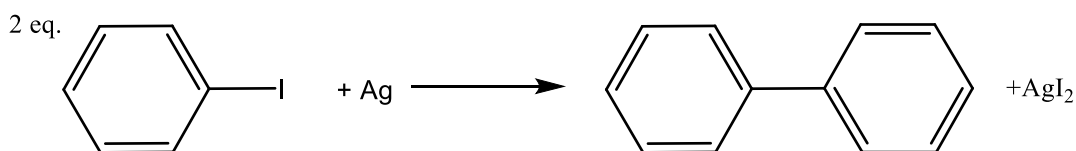


In a glovebox, hexatrimethylsilylhexa-*m*-phenylene (50 mg, 56 mol) was dissolved in dry and degassed chloroform (9 mL). To degas chloroform, a schlenk flask containing the solvent was purged with an inert gas (bubbling an inert gas through the solvent), where the buildup pressure was released using a needle. A solution of iodomonochloride (1 M, 0.22 g, 1.35 mL) in dichloromethane was added in the absence of

light. The resulting mixture was stirred at room temperature for 18 hours and then stopped with concentrated, aqueous sodium thiosulfate (3 mL). The precipitate was vacuum filtered and washed extensively with chloroform, THF, water, and dried in vacuo to obtain a hardly soluble colorless powder (yield 6 mg, 12%) (Appendix 8).

3.3 Discussion and Future Directions

After successful synthesis of the CHP monomer, the next steps involve cross-linking the monomer by silver-promoted aryl-aryl coupling under ultrahigh vacuum conditions¹. Bieri et al.¹ effectively developed polyphenylene networks by depositing CHP from a resistively heated quartz crucible to a silver substrate at 745 K. Surface-assisted coupling reactions were observed to begin at 575 K, and it was found that desorption of Ag-I does not occur until 805 K. In addition, they showed that surface-assisted aryl-aryl coupling reactions could be done on various substrates (such as gold and copper)². This suggests that this method is a versatile way of designing 2D materials, modifying pore size and pore spacing of the network structure via the appropriate chemical design of the monomers. The dissociation of aryl halides is thermodynamically favored on metal surfaces because the carbon-halogen (C-I) bond is weaker than carbon-carbon or carbon-hydrogen bonds, in addition to a strong bond between the metal surface atoms and halogen^{1,2}.



Scheme 3: Silver-promoted aryl-aryl coupling of iodobenzene to biphenyl. Republished with permission of Royal Society of Chemistry from Ref. [1]; permission conveyed through Copyright Clearance Center, Inc.

The deposition is done by utilizing a resistive thermal evaporation technique. A physical vapor deposition technique where the material in an ultrahigh vacuum is resistively heated using electrical energy³¹. The material is heated until it evaporates, and the vaporized molecules travel from the source to the substrate (such as silver) and deposit to form a thin-film coating. These ultrahigh vacuum conditions are necessary to maintain film purity and

avoid undesired collisions with gas molecules that can change the direction of travel for the vaporized molecules and impact coverage^{31,32}.

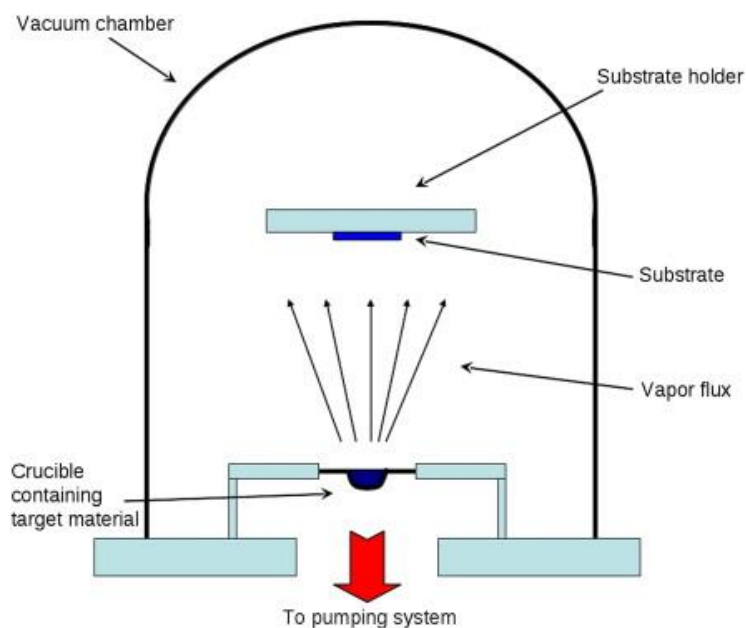


Figure 3.12: Schematic of the resistive thermal evaporation technique. Reprinted from Ref. [31], Copyright 2013, with permission from Elsevier.

Recently, Xu et al. proposed a method achieved bulk production of 2D polyphenylene networks (PPNs) through a solution-based Wurtz reaction³³. A Wurtz reaction is a coupling reaction where two alkyl halides react together to form a higher alkane using metallic sodium. Here, they utilize a solvothermal environment to melt sodium (Na) pieces forming expanded bubbles. When these bubbles break, a large amount of smaller Na spheres are produced. This allows the Wurtz reaction to occur between Na and 1,3,5-trichlorobenzene (like the starting material used in 3.2: 1,3,5-tribromobenzene) on these Na spheres. Under ideal conditions, the intercoupling reaction between trichlorobenzene (TCB) occurs as NaCl precipitate is formed³³. After which, the single formed layers of PPNs exfoliate from the surface when Na spheres are depleted. They pointed out that incomplete dechlorination of TCB may cause defects in these sheets under real reaction conditions³³.

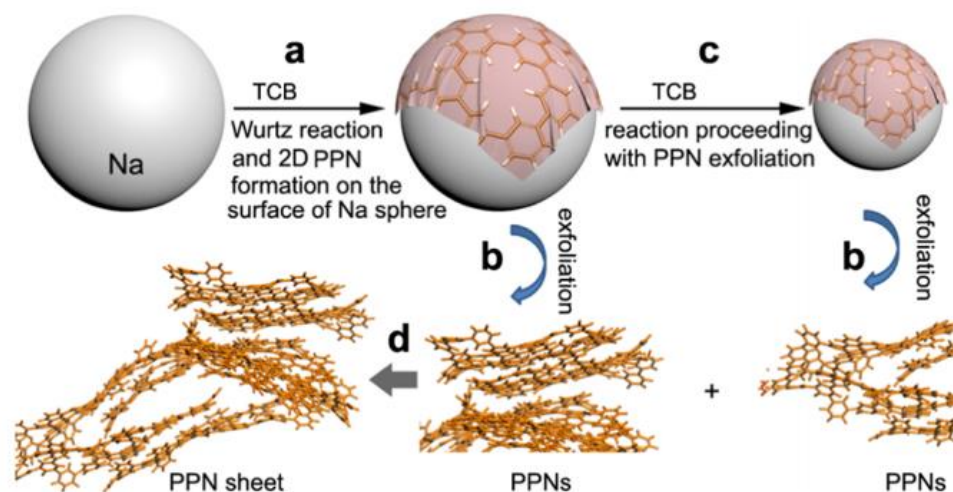


Figure 3.13: Reaction mechanism for the formation of PPN sheets using TCB and Na spheres. Reprinted with permission from Ref. [33]. Copyright 2019, American Chemical Society.

In summary, the CHP monomer was successfully synthesized. The next steps include using the thermal evaporator to produce 2D Polyphenylene on a silver substrate. It was determined that the amount of material synthesized would be enough for three attempts on the thermal evaporator. Some future challenges include suspending and transferring the developed 2D material onto a silicon wafer and studying gas flow. In addition, the Wurtz reaction should be tested and compared to the method used by Bieri et al.¹ as it is a fast and straightforward reaction that can self-assemble 2D PPNs.

3.4 References

1. Bieri, M.; Treier, M.; Cai, J.; Ait-Mansour, K.; Ruffieux, P.; Gröning, O.; Gröning, P.; Kastler, M.; Rieger, R.; Feng, X.; Müllen, K. Porous graphenes: two-dimensional polymer synthesis with atomic precision. *Chemical communications* **2009**, 45, 6919-6921.
2. Bieri, M.; Nguyen, M.T.; Gröning, O.; Cai, J.; Treier, M.; Ait-Mansour, K.; Ruffieux, P.; Pignedoli, C.A.; Passerone, D.; Kastler, M.; Müllen, K. Two-dimensional polymer formation on surfaces: insight into the roles of precursor mobility and reactivity. *Journal of the American Chemical Society* **2010**, 132, 16669-16676.
3. Pisula, W.; Kastler, M.; Yang, C.; Enkelmann, V.; Müllen, K. Columnar Mesophase Formation of Cyclohexa-m-phenylene-Based Macrocycles. *Chemistry—An Asian Journal* **2007**, 2, 51-56.
4. Siciliano, T.; Tepore, A.; Filippo, E.; Micocci, G.; Tepore, M. Characteristics of molybdenum trioxide nanobelts prepared by thermal evaporation technique. *Materials Chemistry and Physics* **2009**, 114, 687-691.
5. The Schlenk Line Survival Guide. 2021. <https://schlenklinesurvivalguide.com/>
6. Parham, W.E.; Jones, L.D.; Sayed, Y.A. Selective halogen-lithium exchange in bromophenylalkyl halides. *The Journal of Organic Chemistry* **1976**, 41, 1184-1186.
7. Schaeffer, D.J. Organolithium chemistry. The acidity of weak carbon acids. *Journal of the Chemical Society D: Chemical Communications* **1970**, 17, 1043-1044.
8. Henderson, R.K.; Hill, A.P.; Redman, A.M.; Sneddon, H.F. Development of GSK's acid and base selection guides. *Green Chemistry* **2015**, 17, 945-949.
9. Bunnett, J.F.; Zahler, R.E. Aromatic Nucleophilic Substitution Reactions. *Chemical Reviews* **1951**, 49, 273-412.
10. Schelhaas, M.; Waldmann, H. Protecting group strategies in organic synthesis. *Angewandte Chemie International Edition in English* **1996**, 35, 2056-2083.
11. Gong, L.Z.; Hu, Q.S.; Pu, L. Optically active dendrimers with a binaphthyl core and phenylene dendrons: Light harvesting and enantioselective fluorescent sensing. *The Journal of organic chemistry* **2001**, 66, 2358-2367.

12. Ye, B.H.; Naruta, Y. A novel method for the synthesis of regiospecifically sulfonated porphyrin monomers and dimers. *Tetrahedron* **2003**, *59*, 3593-3601.
13. Farah, D.; Karol, T.J.; Kuivila, H.G. Nucleophilicity vs. basicity in reactions of n-butyllithium and tert-butyllithium with tetramethylstannane. *Organometallics* **1985**, *4*, 662-666.
14. Bellina, F.; Carpita, A.; Rossi, R. Palladium catalysts for the Suzuki cross-coupling reaction: an overview of recent advances. *Synthesis* **2004**, *15*, 2419-2440.
15. Brown, H.C.; Kramer, G.W.; Levy, A.B.; Midland, M.M. Organic Synthesis via Boranes. *Wiley-Interscience New York* **1975**, Vol 1.
16. Miyaura, N.; Yamada, K.; Suzuki, A. A new stereospecific cross-coupling by the palladium-catalyzed reaction of 1-alkenylboranes with 1-alkenyl or 1-alkynyl halides. *Tetrahedron Letters* **1979**, *20*, 3437-3440.
17. Gujral, S.S.; Khatri, S.; Riyal, P.; Gahlot, V. Suzuki cross coupling reaction-a review. *Indo Global Journal of Pharmaceutical Sciences* **2012**, *2*, 351-367.
18. Name-reaction.com. 2021. Suzuki cross-coupling ~ Name-Reaction.com. <https://www.name-reaction.com/suzuki-cross-coupling>.
19. Liu, Q.; Tang, Z.; Wu, M.; Zhou, Z. Design, preparation and application of conjugated microporous polymers. *Polymer international* **2014**, *63*, 381-392.
20. Ben, T.; Qiu, S. Porous aromatic frameworks: Synthesis, structure and functions. *CrystEngComm* **2013**, *15*, 17-26.
21. Yamamoto, T.; Wakabayashi, S.; Osakada, K. Mechanism of C-C coupling reactions of aromatic halides, promoted by Ni (COD) ₂ in the presence of 2, 2'-bipyridine and PPh₃, to give biaryls. *Journal of organometallic chemistry* **1992**, *428*, 223-237.
22. Wilke, G. Contributions to Organo-Nickel Chemistry. *Angewandte Chemie International Edition in English* **1988**, *27*, 185-206.
23. Lennox, A.J.; Lloyd-Jones, G.C. Selection of boron reagents for Suzuki-Miyaura coupling. *Chemical Society Reviews* **2014**, *43*, 412-443.
24. Xie, J.; Sekine, K.; Witzel, S.; Krämer, P.; Rudolph, M.; Rominger, F.; Hashmi, A.S.K. Light-Induced Gold-Catalyzed Hiyama Arylation: A Coupling Access to Biarylboronates. *Angewandte Chemie International Edition* **2018**, *57*, 16648-16653.

25. Sandford, C.; Aggarwal, V.K. Stereospecific functionalizations and transformations of secondary and tertiary boronic esters. *Chemical Communications* **2017**, *53*, 5481-5494.
26. Hall, D.G. Structure, properties, and preparation of boronic acid derivatives. Overview of their reactions and applications. *Boronic Acids* **2005**, *1*.
27. Wiesenfeldt, M.P.; Knecht, T.; Schleppehorst, C.; Glorius, F. Silylarene Hydrogenation: A Strategic Approach that Enables Direct Access to Versatile Silylated Saturated Carbo-and Heterocycles. *Angewandte Chemie International Edition* **2018**, *57*, 8297-8300.
28. Huang, W., Wang, M., Du, C., Chen, Y., Qin, R., Su, L., Zhang, C., Liu, Z., Li, C. and Bo, Z., 2011. Synthesis of Shape-Persistent Macrocycles by a One-Pot Suzuki–Miyaura Cross-Coupling Reaction. *Chemistry–A European Journal*, *17*(2), pp.440-444.
29. Bonesi, S.M.; Fagnoni, M. The Aromatic Carbon–Carbon ipso-Substitution Reaction. *Chemistry–A European Journal* **2010**, *16*, 13572-13589
30. Taylor, R. Electrophilic aromatic substitution. *J. Wiley* **1990**.
31. Martín-Palma, R.J.; Lakhtakia, A. Vapor-deposition techniques. *Engineered Biomimicry, Elsevier Inc.* **2013**, 383-398
32. Xie, J.; Xie, Q.; Ma, R., Huang, J.; Zhang, C.; Liu, D. Annealing temperature dependent structures and properties of ferromagnetic Fe₃Si films fabricated by resistive thermal evaporation. *Journal of Materials Science: Materials in Electronics* **2018**, *29*, 1369-1376.
33. Xu, C.; Xu, Z.; Lu, Q.; Shao, M.; Zhou, J.; Gai, L. Two-Dimensional Polyphenylene Networks with Tunable Micropores for Hydrogen Storage. *ACS Sustainable Chemistry & Engineering* **2019**, *7*, 18341-18349.

Chapter 4

4 Developing Graphdiyne Membranes

4.1 Introduction

In this work, I evaluate the potential of graphdiyne (GDY) as a gas-separation membrane and perform measurements to study the flow of different gases through GDY at centimeter and micron-scale. I first developed centimeter-scale GDY membranes and studied their permeance and selectivity in a flow cell. Next, I developed a method to study the flow of various gases through a single GDY flake at micron-scale areas. Here, I positioned GDY over a ~ 10 nm hole in graphene that is suspended over a $5\ \mu\text{m}$ diameter cavity (Fig. 4.1), as well as measuring flow rates by charging the cavity with gas and monitoring the rate at which the graphene deflates on an atomic force microscope (AFM). Where prior studies have only measured graphene permeance in this way, I have extended the technique to measure inherently porous materials. The concept is to use the impermeability of graphene to create a nanoballoon by sealing a microcavity. The graphene will deflect when pressurized, and by measuring the change in deflection as the nanoballoon deflates, the flow rate can be measured. A ~ 10 nm hole is then created in the graphene and is covered with the permeable GDY to be measured. Using a much larger graphene area than GDY area provides sufficiently large deflections at low enough flux to resolve the flow rates. The nanoballoon is made primarily of graphene because the GDY is highly permeable. If GDY was suspended over the entire cavity, the nanoballoon would deflate too fast to measure any gases by AFM. The results inform future development efforts on inherently porous atomically thin membranes.

In the following sections, I discuss each step in the development of the GDY membrane. After which, I present the permeance and selectivity data from the flow cell, and membrane deflation data obtained from AFM after charging the membrane with gases like helium (He), nitrogen (N_2), argon (Ar), methane (CH_4), and sulfur hexafluoride (SF_6). Lastly, I highlight some future improvements that could ensure more accurate measurements.

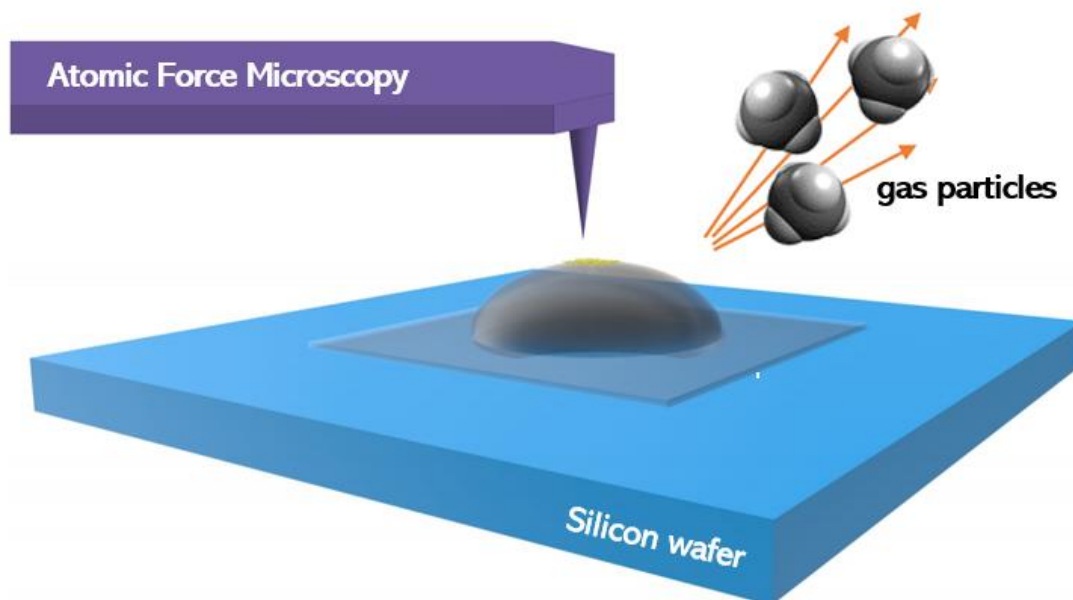


Figure 4.1: Measurement setup for gas flow through Graphdiyne (yellow), which covers a 10 nm-diameter hole in inflated graphene (grey) over a cavity in a silicon wafer (blue).

4.2 Centimeter-Scale GDY Membranes in a Flow Cell

I evaluated GDY's potential as a gas-separation membrane by measuring the permeance and selectivity of centimeter-scale graphdiyne (GDY) membranes in a flow cell². At this scale, we better understand how selective GDY can be when we simultaneously look at multiple flakes. Exfoliated GDY flakes were deposited on a 10 nm diameter pore polycarbonate track etch membrane (PCTEM)³ via vacuum filtration – the details of GDY exfoliation methods are highlighted in section 4.2.1A. The membrane was then placed in a flow cell and permeance and selectivity values were obtained (more details in section 4.2.1B). The measurement values and observations are discussed in section 4.2.2.

4.2.1 Experimental Design and Methods

Commercially available GDY was purchased from ACS Materials and was viewed using AFM and SEM. This helped distinguish dust particles or other impurities from GDY.

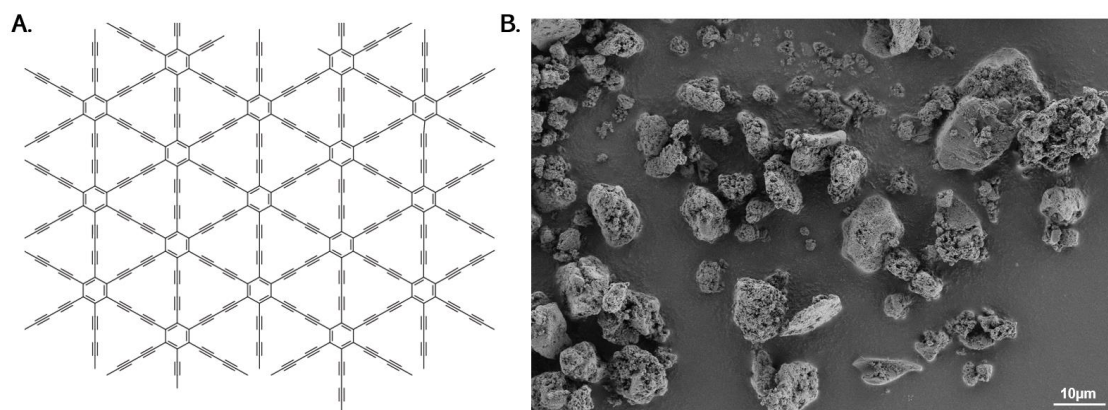


Figure 4.2: **A.** Chemical structure of GDY. Reprinted with permission from Ref. [4]. Copyright 2018, Taylor & Francis. **B.** SEM image of GDY powder on a silicon wafer.

A. Graphdiyne Exfoliation

Here the aim is to exfoliate GDY powder and create ultra-thin graphdiyne flakes. As mentioned in Chapter 1, the synthesis of large-area ultrathin GDY films with high quality and uniformity remains challenging⁵. In addition, due to the poor solution dispersibility of GDY, the transfer of synthesized GDY onto other substrates without damaging the structure remains an issue. Therefore, mechanical and liquid exfoliation techniques were attempted to achieve single or few-layered GDY flakes without creating additional defects.

Mechanical Exfoliation

A small amount of graphdiyne was placed on the sticky side of PVC vinyl surface protection specialty tape, and the tape was folded, pressed gently, and then pulled off carefully. After numerous repetitions, the GDY layer became thinner. This method is commonly used to split a layered material into atomically thin sheets. The resulting tape was placed on a silicon wafer and then peeled off, depositing GDY layers. The wafer was then viewed using AFM and an average flake size of 40-100 nm was obtained.

However, the main issue with this method was the deposition of tape residue along with GDY flakes (Fig. 4.3).

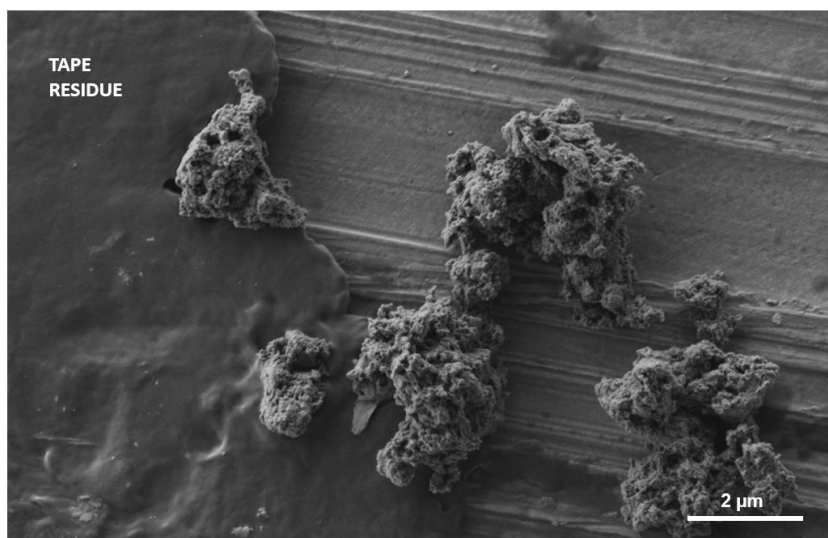


Figure 4.3: SEM image of GDY flakes and tape residue on copper foil.

Liquid-Phase Exfoliation

Yan et al.⁶ reported a high-yield damage-free liquid-phase exfoliation method to prepare single and few-layered GDY flakes in an aqueous solution of lithium hexafluorosilicate (Li_2SiF_6) through stirring and at ambient conditions. They found 85% of the obtained flakes to have 1 to 5 layers, with 18% being single layered. This method does not create any additional defects, allows the GDY flakes to be transferred to other substrates, and was shown to produce smaller flake sizes as compared to mechanical exfoliation.

Using an exfoliant

During the experiment, 50 mg of Li_2SiF_6 was dissolved in 5 mL of water, and then 5 mg of GDY powder was added to this solution. The reaction mixture was stirred for 60 hours under ambient conditions (25 °C), and the obtained dispersion was allowed to settle for 6 hours. After which, the dispersion was collected, filtered through a 200 nm-pore polycarbonate track etched membrane, and consecutively washed with deionized water and isopropanol. The membrane was then heated at 120 °C for 3 hours. The resulting membrane was then viewed using AFM, and flake sizes of 15-30 nm were obtained.

After this step, I planned to dissolve the polycarbonate membrane using chloroform to deposit these GDY flakes directly onto the silicon wafer. However, this adds impurities to

the membrane. The other possible method was to directly transfer the GDY layers from the aqueous solution, but it would contain the exfoliant and add impurities to the membrane. Therefore, a method proposed by Zhang et al.⁷ was followed where an exfoliant was not required, and the method relied on ultrasonication treatment to produce flake sizes of 3.3 – 4 nm.

Without using an exfoliant

For this experiment, 0.1 mg of GDY powder was ground for 30 min and then dissolved in 20 mL of isopropyl alcohol resulting in a brown suspension. After which, the solution underwent an ultrasonication treatment with 45 kHz frequency for 30 min to disperse the nanosheets. Then, the solution was centrifuged for 30 min at 3500 rpm to stratify the dispersed liquid. After which, the top layer of the liquid was pipetted onto a silicon wafer and heated at 60 °C for 1 hour. The resulting wafer was then viewed using SEM and AFM, and an average flake size of 10-25 nm (Fig. 4.4) was obtained.

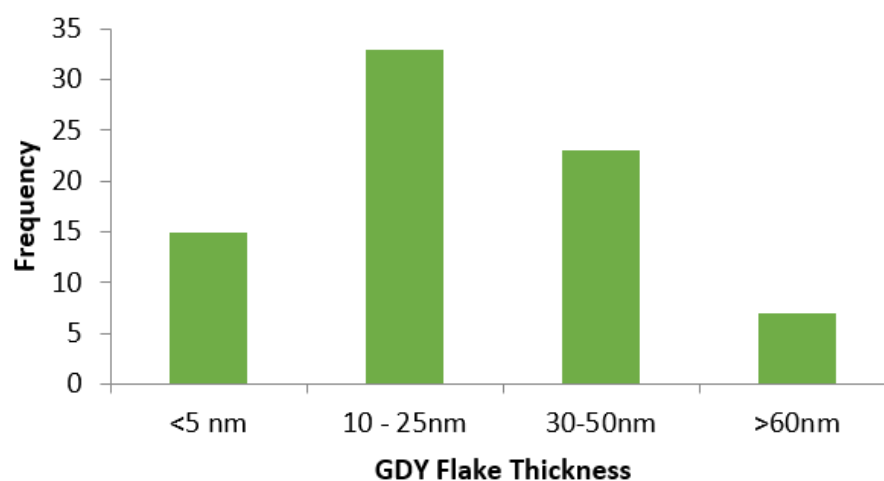


Figure 4.4: Frequency of various GDY flake sizes seen on a silicon wafer via AFM after GDY ultrasonication treatment, with the highest being in the 10-25 nm range.

This method successfully deposited small GDY flakes onto a silicon wafer without adding any impurities or defects.

B. GDY Measurements with Flow Cell

A volume of 16 mL GDY was prepared and then deposited onto a 10 nm PCTEM using vacuum filtration overnight. After which, the PCTEM was heated at 60 °C for 1 hour. The cooled down membrane was then covered with an aluminum foil tape that had a 0.25-inch hole in the center. This ensures the passage of gas through a small and controlled area of the membrane. Aluminum foil covered PCTEM is then placed in the membrane holder and the flow cell was evacuated using the vacuum pump. Next, the desired gas was passed through the membrane, and the absolute pressures upstream and downstream of the membrane were monitored.

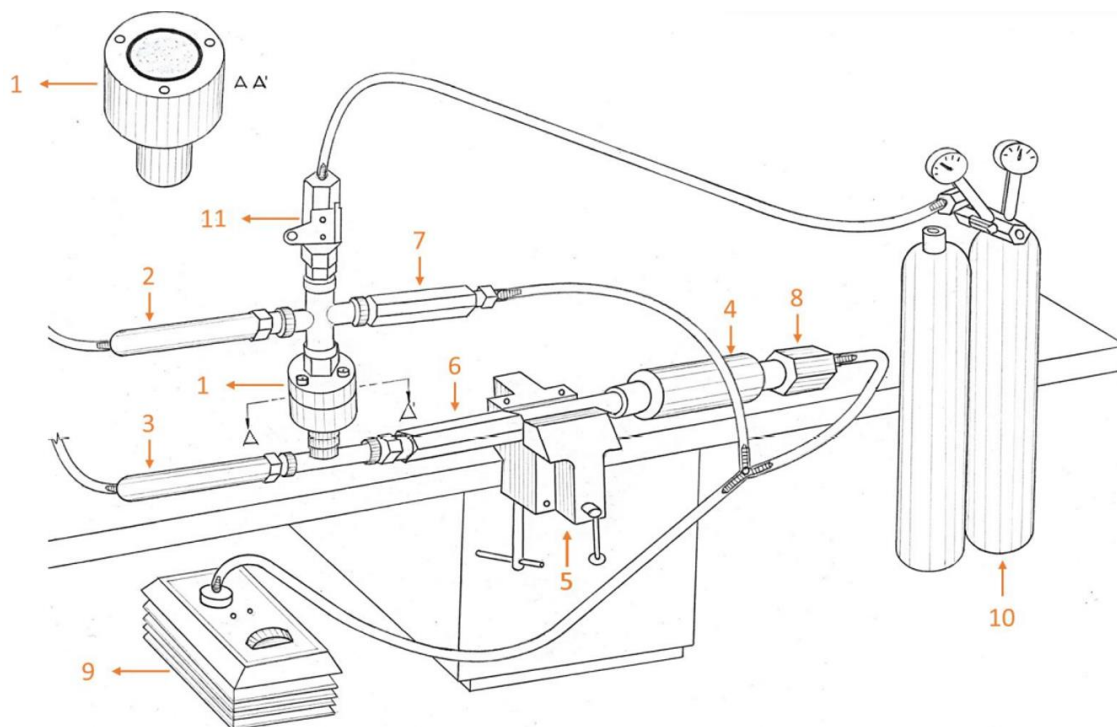


Figure 4.5: Diagram of the flow cell. Created by Samuel Gomez Suarez. **1.** The membrane holder. **2.** and **3.** Pressure transducers that display absolute pressure upstream and downstream the membrane. **4.** Cylinder (volume of 150 mL). **5.** Holds the flow cell in place. **6.** Valve that reduces the downstream volume. **7.** And **8.** Valves connected to the vacuum pump. **9.** Vacuum pump. **10.** Gas cylinders. **11.** Valve connected to the gas supply.

4.2.2 Results and Discussion

A flow cell was used to measure gas flow through GDY on a 10 nm PCTEM to obtain permeance and selectivity data. The values obtained would help gauge GDY's potential as a gas-separation membrane. However, due to gaps in GDY coverage and variation in the GDY thickness across the membrane, these tests do not reflect the full potential of GDY membranes that might be achieved after further development.

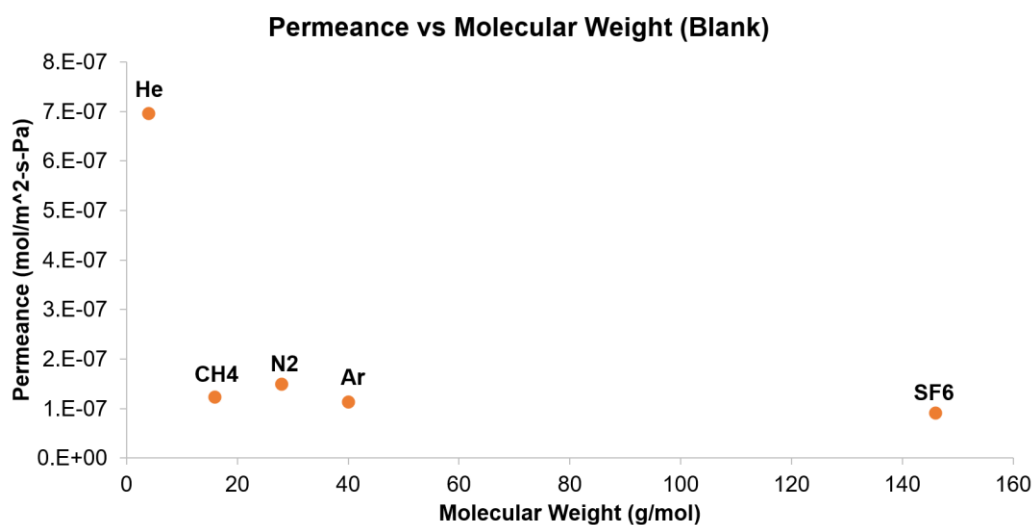


Figure 4.6: Measured permeance for bare 10 nm PCTEM (blank) vs. molecular weight for He, Ar, N₂, CH₄ and SF₆.

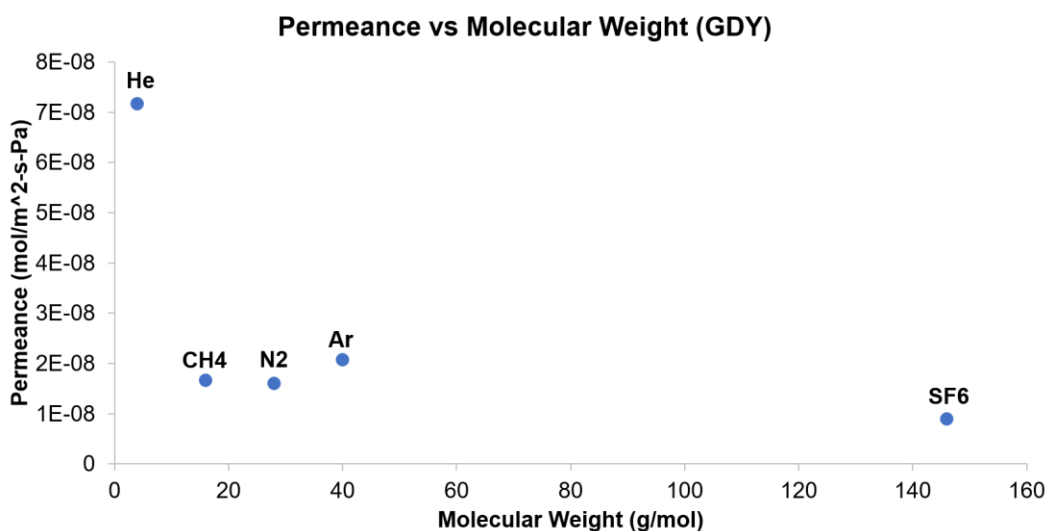


Figure 4.7: Measured permeance for GDY on 10 nm PCTEM vs. molecular weight for He, Ar, N₂, CH₄ and SF₆.

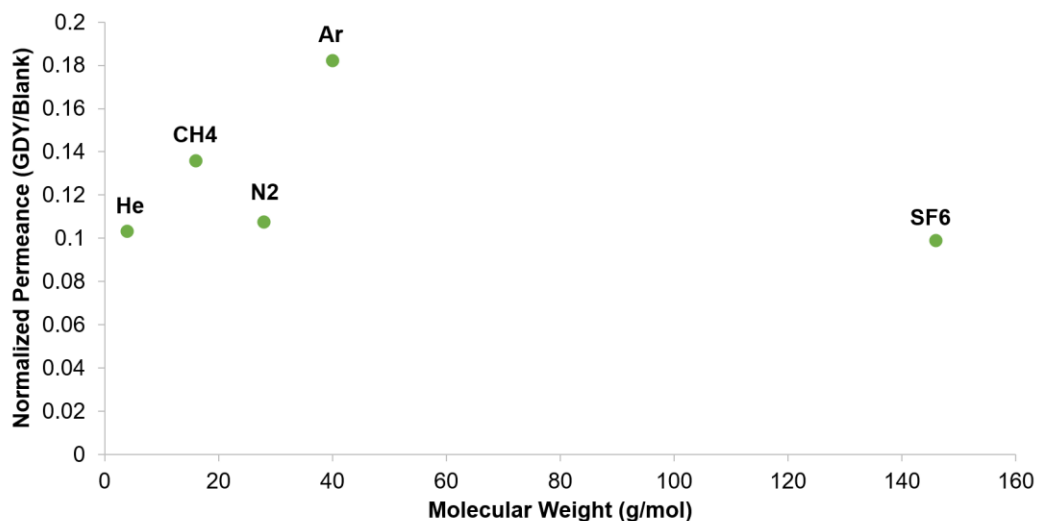


Figure 4.8: Normalized permeance (GDY Permeance/Blank Permeance) vs. molecular weight for He, Ar, N₂, CH₄ and SF₆.

Table 4.1: Selectivity values comparing the calculated Knudsen ratios with the obtained values for bare 10 nm PCTEM and GDY on 10 nm PCTEM. Numbers in orange are selectivity values lower than bare 10 nm PCTEM whereas blue are values higher than bare 10 nm PCTEM.

	Knudsen Values	Bare 10 nm PCTEM	GDY on 10 nm PCTEM
He/Ar	3.16	6.12	3.46
He/N ₂	2.65	4.66	4.46
He/CH ₄	2.00	5.67	4.30
He/SF ₆	6.04	7.63	7.96
Ar/N ₂	0.84	0.76	1.29
Ar/CH ₄	0.63	0.93	1.24
Ar/SF ₆	1.91	1.25	2.30
N ₂ /CH ₄	0.76	1.22	0.96
N ₂ /SF ₆	2.28	1.64	1.79
CH ₄ /SF ₆	3.02	1.35	1.85

The permeance of gases through the bare 10 nm PCTEM (Fig. 4.6) are higher than the permeance with GDY on the 10 nm PCTEM (Fig. 4.7), implying that the GDY flakes present on the membrane are impeding gas flow. However, the GDY membrane was no more selective than the supporting 10 nm PCTEM (Fig. 4.8). This may be caused by gaps

in the material coverage producing low selectivity leakage flow. Similarly, the thickness and relative orientation of GDY layers varies over the membrane, with some GDY flakes having much lower selectivity than others. Such leakage pathways have similarly hampered the development of membranes made from other two-dimensional materials, but defect mitigation strategies are currently being developed⁸. These measurements provide a baseline for further GDY membrane development on larger scales.

In table 4.1, Knudsen selectivity values are being compared to the bare PCTEM and GDY on PCTEM. Note Knudsen flow occurs when the pore diameters are larger than molecular size but much smaller than the gas mean free path⁹. In Knudsen effusion, collisions of molecules with the pore wall are more prominent than collisions between molecules. Thus, a molecule with a lower molecular mass travels faster and has higher permeance than one with a higher molecular mass.

The Knudsen values are inversely proportional to the square root of molecular weight (MW) of each gas⁸. Therefore, to calculate selectivity for He/Ar, the following equation was used: $\sqrt{\frac{MW \text{ of Ar}}{MW \text{ of He}}}$. Values greater than the Knudsen value would indicate selectivity provided by the GDY but were not seen (Table 4.1).

To summarize, an average permeance and selectivity values for GDY on a 10 nm PCTEM were obtained, but no significant change in selectivity was observed. To improve the performance of these membranes, the deposition technique needs to be improved to ensure a more even coverage on PCTEM or to seal defects.

4.3 Single-Flake GDY Analysis using AFM

To experimentally evaluate the potential of GDY as a gas separation material, I instead measure the permeance of a nanoscopic area of the material. Defects and gaps in material coverage encountered at the centimeter-scale can be avoided at micron-scale, allowing us to focus on the inherent properties of the material instead of those of a composite membrane.

Here I developed a method to study the flow of various gases through a single GDY flake at micron-scale areas. As mentioned before, prior studies have used a similar technique to measure graphene permeance, but this method has extended the technique to measure flow through inherently porous materials. By measuring flow through various inherently porous materials, the ability of the material to act as an ideal membrane in gas and liquid separation applications was verified. The three main steps to develop the GDY membrane setup are GDY exfoliation (detailed in section 4.2.1A), multi-layer graphene stack preparation, and membrane fabrication. The gas deflation data are presented and discussed in section 4.3.2.

4.3.1 Experimental Design and Methods

A. Fabrication of a Multi-Layer Graphene Stack

Here the aim is to fabricate a multi-layered graphene stack on a silicon wafer to provide measurable flow rates by having more considerable deflections at a low enough flux. In prior studies, graphene flakes were initially produced via mechanical exfoliation (Scotch-tape method)¹⁰. However, since it is time-consuming and only yields micrometer flakes, they are not used for large-area graphene applications¹¹. A chemical vapor deposition technique is a common approach that produces high-quality graphene on copper. CVD graphene was transferred onto the silicon substrate using a thin sacrificial layer of poly (methyl methacrylate) (PMMA) to support the graphene when the copper is removed¹².

PMMA Transfer

To obtain a graphene stack, a piece of PMMA on graphene on copper was etched in an ammonium persulfate etchant (APS-100) for 15 min. After which, the PMMA-graphene was transferred using a glass slide and cleaned in a water bath for 5 min, which was then repeated two more times. The PMMA-graphene was then scooped up using a piece of graphene on copper. The two-layer graphene stack was then allowed to air dry before heating it to 180 °C for 20 min. This process was repeated three more times to obtain a five-layered graphene stack.

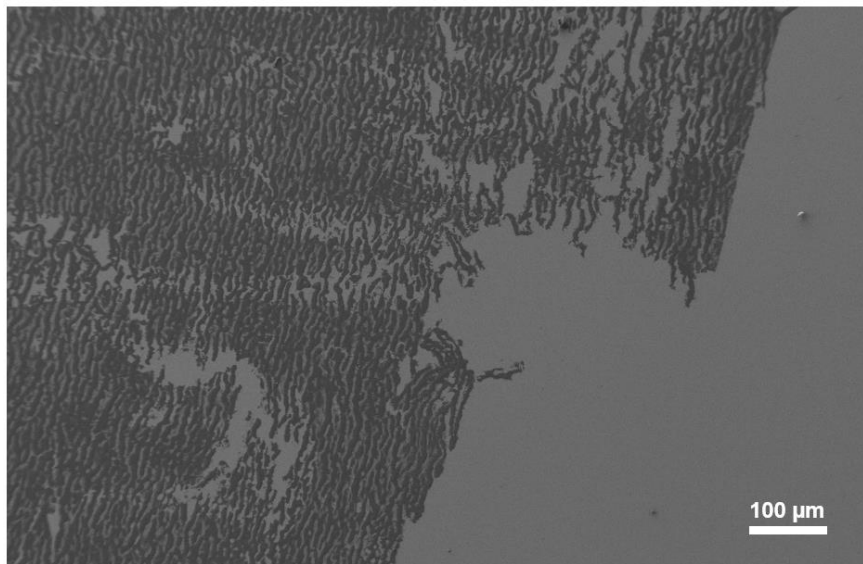


Figure 4.9: SEM image of PMMA-supported Graphene layers on silicon wafer.

This method was successful in producing a PMMA-supported graphene stack and was initially used in membrane fabrication. However, PMMA removal was not evenly removed in some areas, making AFM measurements difficult to interpret. Hence, an emerging polymer-free transfer method was used to achieve clean transfers. A method proposed by Zhang et al.¹³ used a liquid-liquid interface to support the free-standing graphene during transfer, reducing interfacial tension that would otherwise tear the graphene after the copper is removed. The copper was etched at an APS and low-viscosity hexane (non-polar solvent) interface, leaving floating graphene that could be scooped onto the silicon substrate.

PMMA-Free Transfer

To obtain a PMMA-Free graphene stack, a piece of graphene on copper was placed onto the surface of 0.1 M ammonium persulfate solution, and a layer of hexane was slowly added on top using a pipette. The copper substrate completely etched within 3 hours, leaving the graphene sheet trapped at the interface. To minimize any possible contamination from the etchant, the graphene sheet was transferred and cleaned using a hexane/water interface for 30 min. The clean graphene layer was then scooped up using a silicon wafer with pre-defined 5 μm diameter cavities. After which, the wafer was air-dried

for 20 min followed by 30 min under vacuum and 1 hour with heat (200 °C) under vacuum. This process was then repeated five times to obtain a five-layered graphene stack.

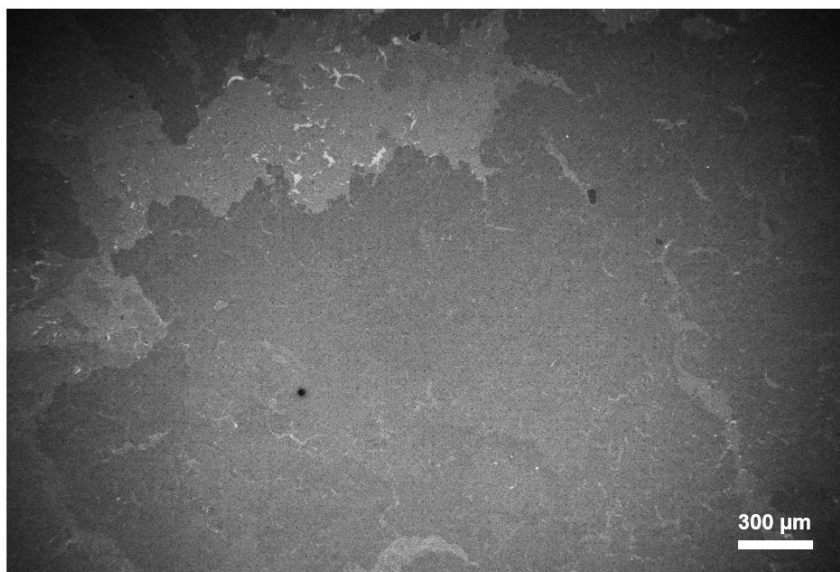


Figure 4.10: SEM image of PMMA-free graphene layers on silicon wafer.

This method successfully produced a clean five-layered graphene stack, which was used for membrane fabrication.

B. Membrane Fabrication

Note that silicon (Si) wafers with pre-defined 5 μm diameter cavities were obtained via photolithographic patterning from Anika Wong.

A photomask with arrays of 3, 5, and 10 μm holes was designed in AutoCAD. This hole pattern was created in the 500 nm thermal oxide layer on a silicon wafer by photolithography followed by etching in hydrofluoric acid. Specifically, the wafer was placed in a spin rinse dryer for cleaning, followed by baking in an oven for 10-15 min. Next, the S1805 photoresist was spun onto the wafer, then baked at 113 °C for 3 min. The wafer was exposed in a mask aligner then submerged in MF 319 developer for 2 min. After which, the wafer was placed in a DI water bath for 2 min and then the spin rinse dryer for another cycle. The oxide layer was used to mask the underlying silicon during reactive ion etching to produce cavities in the silicon. The wafers were then sent to the University of

Toronto for ion etching to create 3 μm wells in the silicon. Subsequently, the oxide mask was completely removed in hydrofluoric acid. The wafers were cut into $\sim 1\text{ cm}^2$ chips and cleaned with isopropanol (IPA). For further cleaning, the chips were placed in acetone and IPA baths, dried with an air gun, and then cleaned via O_2 plasma etching.

PMMA-Graphene Method

PMMA-graphene stack on copper, obtained from the PMMA-Transfer method, was submitted to Nanofabrication Facility for making 30 nm-sized holes every 5 μm using SEM-FIB. After which, PMMA was removed using acetone rinse for 1 hour, followed by IPA rinse for 1 hour. Then the graphene stack on copper was etched and cleaned as before. The resulting graphene was scooped onto a silicon wafer with pre-defined micrometer wells. After which, the region containing holes was identified using SEM and AFM. The fabricated membrane was placed in a pressure chamber at 100 kPa for 48 hours to allow inflation of the pores, and then deflation of the pores was measured using AFM over 48 hours. The PMMA residue on the graphene was a concern as it could alter the mechanical properties of the nanoballoon or potentially obstruct pores in the GDY. For this reason, a switch to a polymer-free graphene transfer method was made.

PMMA-Free Graphene Method

A five-layered graphene stack obtained from the PMMA-Free transfer method was submitted to the Nanofabrication Facility for making 10 nm and 20 nm-sized holes at the center of the pre-defined micrometer wells in the silicon wafer using FIB. After which, the region containing holes was identified using SEM and AFM. The fabricated membrane was then placed in a pressure chamber at 100 kPa for two days to allow inflation of the pores, and then deflation of the pores was measured using AFM over 48 hours.

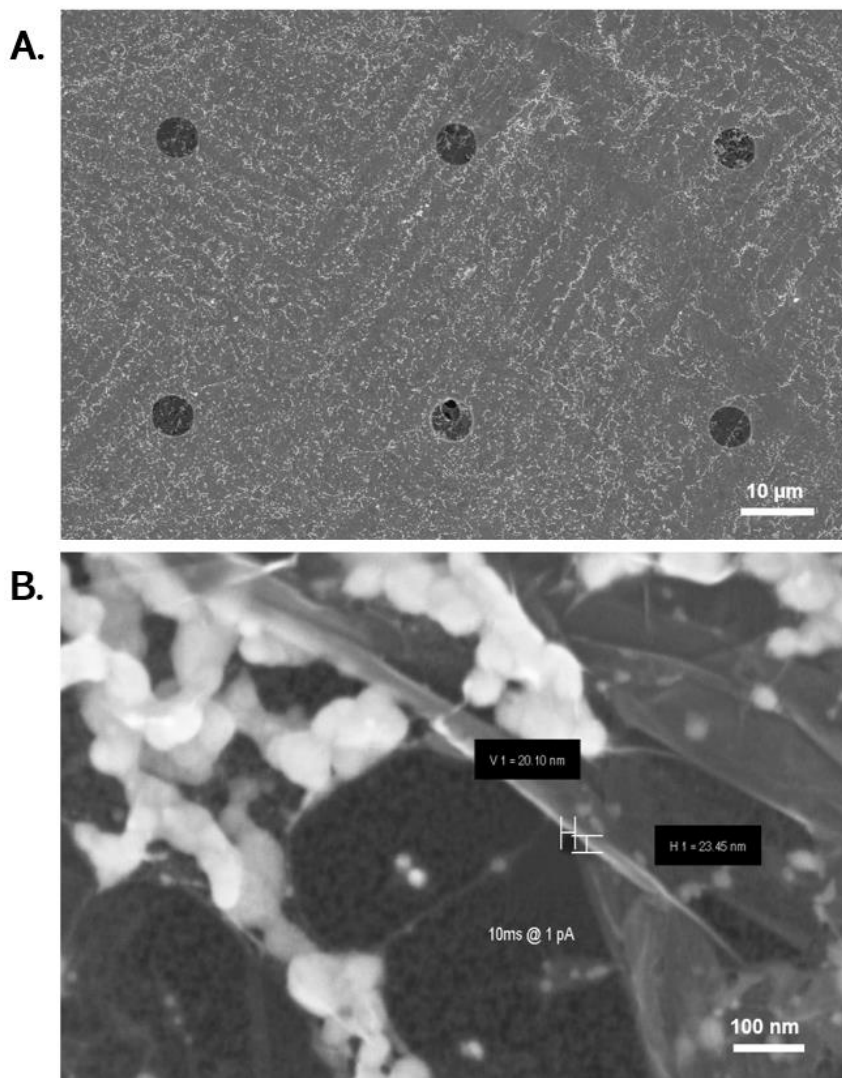


Figure 4.11: **A.** SEM image of four-layered graphene on a silicon wafer with six pre-defined 5 μm cavities. **B.** SEM image of a 10 nm hole in graphene on a 5 μm cavity in the silicon wafer.

C. Deposition of GDY onto the Membrane

Before the deposition of GDY, 10 nm holes made on the fabricated membrane were tested by charging the membrane with air at 100 kPa over 48 hours. Once removed from the pressure chamber, air begins to escape from the well. The flow rate from the 10 nm holes was very high, resulting in full deflation within the 5 min time between removing from the chamber to imaging in the AFM. The nanoballoon was not inflated when imaged by AFM, confirming that the resistance to gas flow through the 10 nm hole is too high to measure

by AFM. This was the desired result, as it means that if inflation is observed after GDY deposition, the measured gas flow rate is entirely due to the GDY material.

Once the holes were tested, GDY was deposited onto the PMMA-free graphene stack using the method described in Section 4.2.2 (no exfoliant). After GDY deposition, the membrane was once again charged with air at 100 kPa over 48 hours, and this time, inflation was observed (Fig. 4.12) and deflation measurements of the membrane were possible.

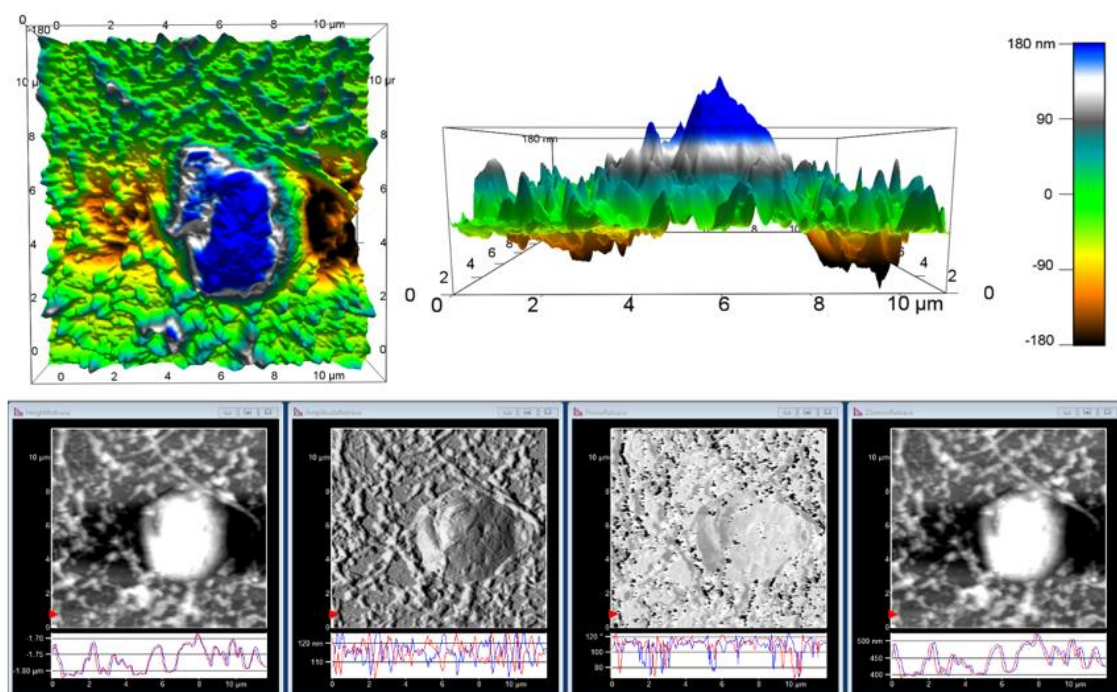


Figure 4.12: AFM images of an inflated membrane (**top**) 3D surface plots. (**bottom**) Height, Amplitude, Phase and Z-sensor retrace.

The silicon wafer was also viewed under SEM. Fig. 4.13A, B highlights the difficulty in viewing GDY in graphene-dense areas where most pores with holes are located. However, in thin graphene-covered areas, GDY flakes become more visible. In Fig. 4.13C graphene can be seen as distinguishable dark grey pieces on the silicon wafer (white). Here GDY is the grey powder (grey) that covers most of the wafer. Once zoomed in (Fig. 4.13 D, E), some of the bigger GDY flakes become clearer.

Even though it is difficult to determine the thickness of GDY covering Pore D15 (used for most gas measurements), I found that the GDY flakes are small, and there is sufficient

GDY coverage on the wafer. I selected the mass of GDY deposited to provide a high probability of covering FIB holes with a single flake. The observation that the graphene over the well deflated quickly prior to GDY deposition and slowly after deposition suggests that a GDY flake was indeed deposited over this hole.

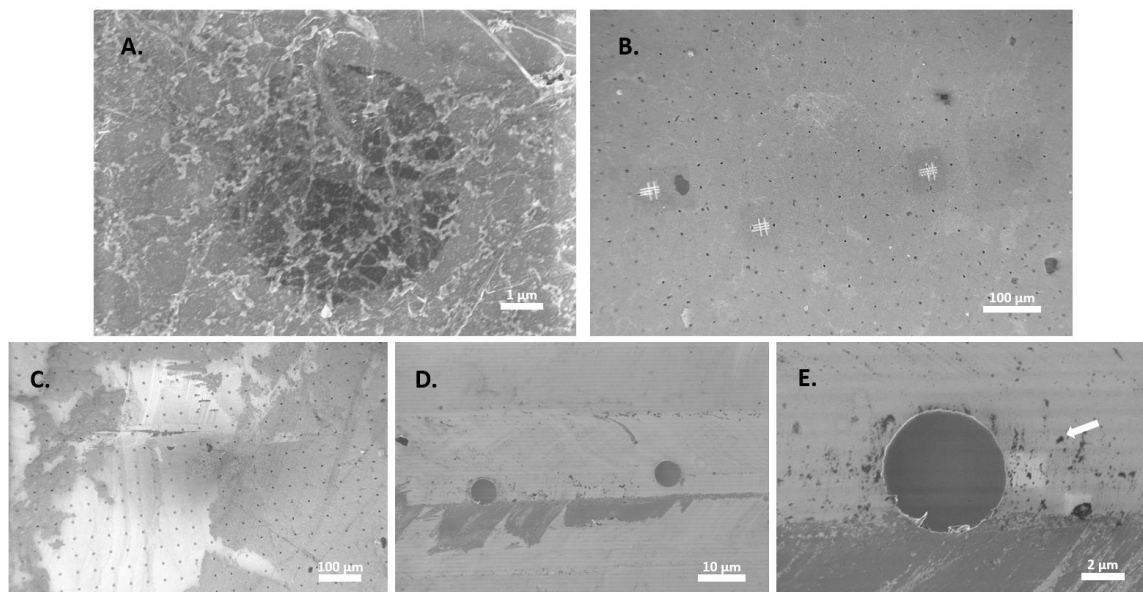


Figure 4.13: SEM images obtained at 1 kV of the silicon wafer after GDY deposition **A.** Pore D15. **B.** Graphene-dense area of interest (hard to see GDY) **C. D.** and **E.** Thin graphene coverage with visible GDY flakes (white arrow).

D. Membrane Charging with Various Gases

The fabricated membrane with GDY was charged with air at 100 kPa over 48 hours, and then deflation of the membrane was measured via AFM (Fig. 4.1). After successful results, the membrane was charged with He over 24 hours at 100 kPa. This resulted in membrane burst for all the cavities with holes. This could be caused by a difference in the gas, as helium flows more rapidly through the system and could more easily permeate into the region where the GDY and silicon meet, delaminating them. In addition, the pressure went to 120 kPa for a couple of minutes as the pressure was being adjusted, which may have caused inflation beyond the threshold. The rest of the graphene-covered cavities were not affected, and thus the sample was resubmitted for the creation of 10 nm and 20 nm holes (as described in Section 4.2.4).

The membrane was then charged with He over 24 hours at 20 kPa, which did not result in a membrane burst. Hence, this process was repeated for Ar, N₂ and CH₄. As SF₆ is a larger gas with greater deflation times, it was charged over 48 hours at 20 kPa.

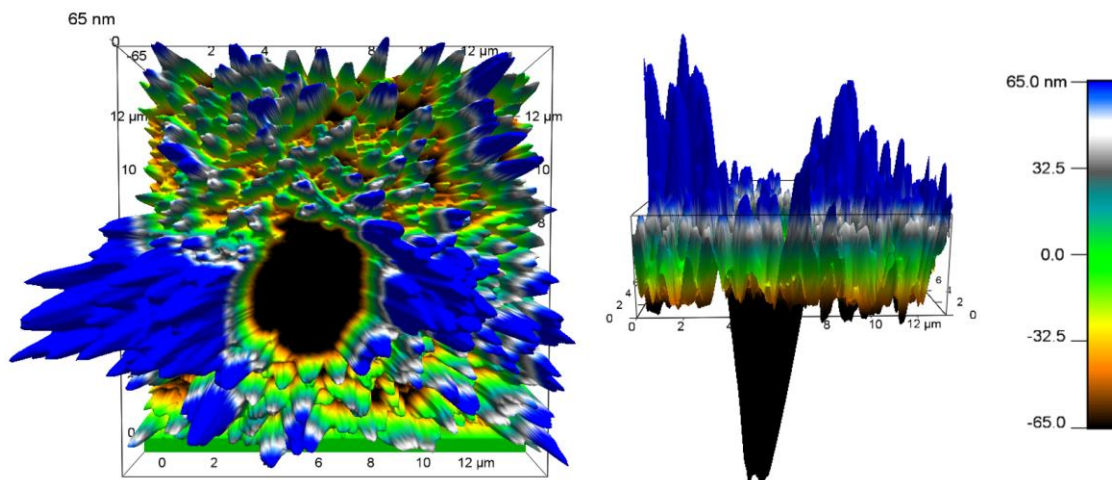


Figure 4.14: 3D surface plots (obtained from AFM) of the burst membrane.

E. On-AFM Setup

Using a closed fluid cell (CFC)¹⁴, I attempted to take AFM measurements of the membrane as the membrane was inflated with a gas. This would allow us to see membrane inflation of gases like He that otherwise deflate too quickly. A CFC is designed to hold gases or liquid through configurable inlet/outlet ports. The design allows the cell, sample, and cantilever holder to be fully assembled and sealed before being transferred to AFM for use. I first tried air at 100 kPa and found that the introduction of air causes a significant shift in the sample pore being viewed. Moreover, the surface images after the CFC setup are different from surface images before the setup, making finding pores more difficult. Overall, on-AFM pressurization measurements through this method are difficult but could be a useful tool if further improved.

4.3.2 Results and Discussion

Fig. 4.15 is the preliminary data obtained after membrane deflation of a 3-layered graphene stack over time. This showed that the method was successful in obtaining deflation measurements via AFM.

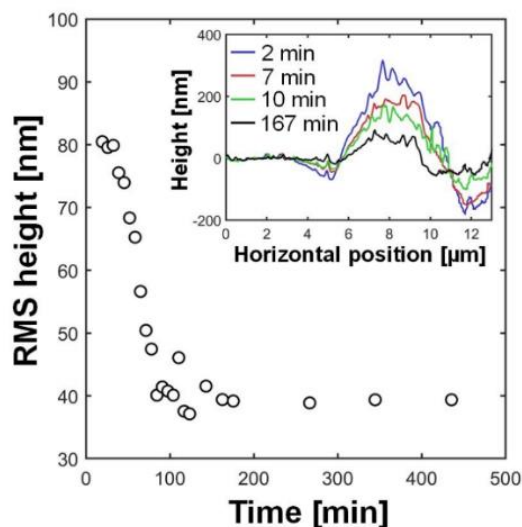


Figure 4.15: Membrane deflation data for a 3-layered graphene stack over time with measured height profiles inset.

As described earlier, the membrane was charged with various gases. The air (100 kPa) measurements were taken prior to other gases and is shown in Fig. 4.16. The higher pressure caused much greater inflation, but the rate of deflation is consistent with the measurements of pure N_2 at 20 kPa.

Pore D15 was used to measure He, Ar, N_2 , CH_4 and SF_6 . Measurements of both SF_6 and N_2 were successful. With He and Ar, the membrane deflated too quickly to measure because they are small gases, and GDY provides low resistance to them. The pore size of GDY is 3.8 \AA [Ref 15], therefore, the membrane showed successful molecular sieving by blocking gases that were bigger than 3.46 \AA (KD of N_2 [Ref 16]). While nitrogen is smaller than the pores in GDY, the GDY flake I measured was likely not a single layer. Gas flow between GDY layers will depend on interlayer channel geometry and gas molecule affinity, strongly affecting permeance.

The gas flow rate values for each measured gas are listed in Table 4.2. To determine the lower bound of permeance for gases that were not measured on D15 (such as He, Ar, and CH_4), the initial bulge volume was set to 0. A worst-case scenario was assumed where the membrane deflated from $0.25 \mu\text{m}^3$ to μm^3 in 10 minutes (flow rate of $0.025 \mu\text{m}^3/\text{min}$). Using Eq. 4.8 in the derivation section (Section 4.3.2A), the lower bound on permeance

was calculated to be 1.69×10^{-20} mol/s, and the lower bound on the selectivity to SF₆ was 23.3.

As determined by the slope of the inflated volume vs. time plot, the gas flow rate was 3 times slower for SF₆ compared to N₂. Inflation was not observed for this well charged with CH₄, but another pore (G14) was found inflated, and the deflation data was collected from G14. It is expected that the GDY flake over G14 was thicker than that over D15, resulting in slower CH₄ deflation that AFM could measure. Moreover, the deflation rate of CH₄ was observed to be faster than expected. As the kinetic diameter of CH₄ is greater than that of N₂, I expected the flow rate of CH₄ to be slower.

It is interesting that D15 did not inflate even though the kinetic diameter of CH₄ is greater than N₂. One possible reason for this could be that gas transport between GDY layers is governed both by molecule size and affinity for the GDY¹⁷. Larger gases tend to adsorb to graphene-like materials with higher surface concentration⁸. Surface diffusion of these gases can enhance transport rates. Increased transport due to surface diffusion through interlayer channels may dominate over the flow impediment produced by the larger size of CH₄ as it navigates these passageways. Although the larger SF₆ might have even greater surface affinity, its size may severely restrict its mobility in the interlayer region. These factors need to be further explored to understand transport through GDY membranes. Nevertheless, GDY membrane displayed molecular sieving of He, Ar, and CH₄ from N₂ and SF₆ gas.

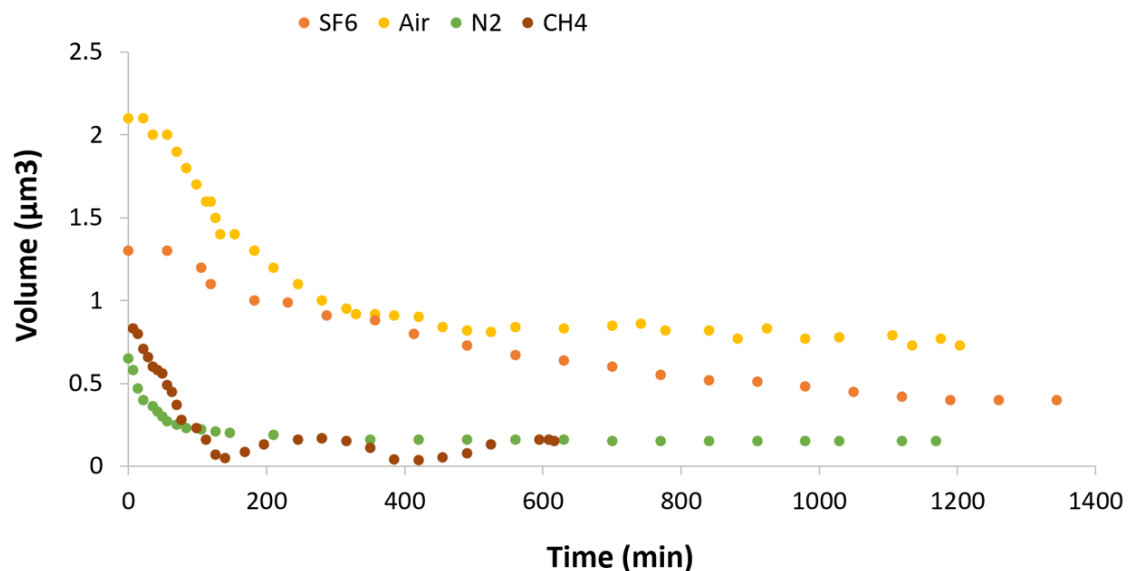


Figure 4.16: Gas deflation data obtained after charging the fabricated membrane with various gases. Note that air (100 kPa) and CH₄ (20 kPa) are from different pores while SF₆ and N₂ (both at 20 kPa) are from the same pore, D15.

Table 4.2: Kinetic diameters¹⁶, calculated slope (volumetric flow rate), initial bulge volume and gas flow rate of each tested gas.

	He	Ar	N ₂	CH ₄	SF ₆
KD (Å)	2.6	3.4	3.46	3.8	5.5
Slope (μm ³ /min)	N/A	N/A	-0.0032	-0.00594	-0.0008
Initial Bulge Volume (μm ³)	N/A	N/A	0.65	0.83	1.3
Gas Flow Rate (mol/s)	N/A	N/A	2.30×10^{-21}	4.63×10^{-21}	7.26×10^{-22}

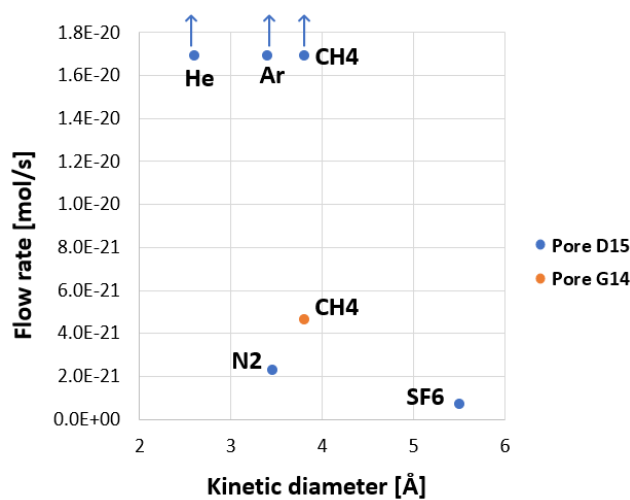
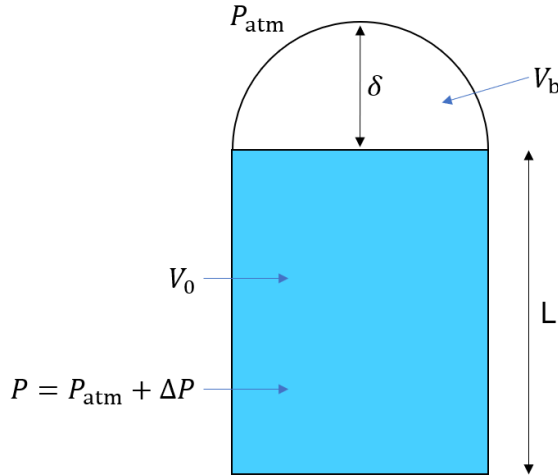


Figure 4.17: Measured gas flow rates through GDY. Arrows indicate that the markers are the lower bound, as the permeance was above the resolvable range.

To summarize, each gas's flow rate (dn/dt) was calculated using Equation 4.18, where the measured parameter was the slope obtained from the gas deflation data (dV_b/dt). The detailed derivation of the equation used is shown in the section below.

Derivation of Gas Flow Rate (mol/s)



Where P is the absolute pressure inside the microcavity, P_{atm} is atmospheric pressure, ΔP is pressure difference, V_b is the volume of the microcavity when the membrane is bulged with deflection δ , V_0 is the initial volume of a microcavity, and L is the length of the microcavity [Ref 1].

Both P and V_b change over time as gas leaks out.

Here I derive the leak rate (gas flow rate) of the microcavity.

Ideal gas law:

$$n = \frac{P(V_0 + V_b)}{RT} \quad (4.1)$$

Where n is the number of moles of gas molecules inside the microcavity, R is gas constant, and T is temperature.

Derivative of Eq. 4.1 gives the molar flow rate:

$$\frac{dn}{dt} = \frac{1}{RT} \frac{d}{dt} [P(V_0 + V_b)] \quad (4.2)$$

Hencky's (1915) solution¹⁸ for the deflection of a thin membrane due to a pressure difference across it relates to bulge volume (V_b) and pressure difference (ΔP) to deflection:

$$\Delta P = \frac{KEw\delta^3}{a^4} \quad (4.3)$$

$$V_b = c\pi a^2 \delta \quad (4.4)$$

where a is the well radius, K (3.09) and C (0.524) are constants for graphene, E is the Young's modulus, and w is the membrane thickness.

$$\frac{dn}{dt} = \frac{1}{RT} \frac{d}{dt} [(P_{atm} + \Delta P)(V_0 + V_b)] \quad (4.5)$$

$$\delta = \frac{V_b}{c\pi a^2} \quad (4.6)$$

Combine Eq. 4.3 and Eq. 4.4 to obtain Eq. 4.7

$$\Delta P = \frac{KEw}{a^4} \left(\frac{V_b}{c\pi a^2} \right)^3 = \frac{KEw}{c^3\pi^3 a^{10}} V_b^3 \quad (4.7)$$

Substitute Eq. 4.7 into Eq. 4.5 to obtain Eq. 4.8.

$$\begin{aligned} \frac{dn}{dt} &= \frac{1}{RT} \frac{d}{dt} \left[\left(P_{atm} + \frac{KEw}{c^3\pi^3 a^{10}} V_b^3 \right) (V_0 + V_b) \right] \\ \frac{dn}{dt} &= \frac{1}{RT} \frac{d}{dt} \left(P_{atm} V_0 + P_{atm} V_b + \frac{KEw}{c^3\pi^3 a^{10}} V_0 V_b^3 + \frac{KEw}{c^3\pi^3 a^{10}} V_b^4 \right) \\ \frac{dn}{dt} &= \frac{1}{RT} \frac{d}{dt} \left(P_{atm} \frac{dV_b}{dt} + \frac{3KEwV_0 V_b^2}{c^3\pi^3 a^{10}} \frac{dV_b}{dt} + \frac{4KEwV_b^3}{c^3\pi^3 a^{10}} \frac{dV_b}{dt} \right) \\ \frac{dn}{dt} &= \frac{1}{RT} \frac{d}{dt} \left(P_{atm} + \frac{3KEwV_0 V_b^2}{c^3\pi^3 a^{10}} + \frac{4KEwV_b^3}{c^3\pi^3 a^{10}} \right) \frac{dV_b}{dt} \end{aligned} \quad (8)$$

B. Applications

In addition to CO₂, several gases like CH₄ and SF₆ are known to have greenhouse effects. Even though SF₆ does not cause air pollution or deplete the ozone layer, it is 24 000 times better than CO₂ at trapping heat¹⁹. Due to their excellent electrical and thermal insulation properties, they are commonly used in medium-high voltage electrical power transmission and distribution (e.g., circuit breakers, capacitors, transformers). The use of this gas continues to rise in the energy distribution industry¹⁹. Even though the net emission rates are much lower than CO₂, they have an extremely high global warming potential (atmospheric lifetime of 3200 years). To control the emission rates and prevent global warming, an efficient recovery and recycling process are needed²⁰. Pure SF₆ can be retrieved by a simple vacuum sucking method, but they are often mixed with other gases¹⁹. The N₂-SF₆ mixture is used as a potential substitute for pure SF₆, and in this case, separation and purification of SF₆ from nitrogen or air is necessary for reuse and recycling.

SF₆ waste products and the separation/retrieval at operating conditions with optimal energy efficiency is only in the initial stages. Choi et al.²¹ ran permeability tests for various commercially available membranes like polycarbonate (PC) and polyimide (PI) and found that the concentration of SF₆ retrieved via PC membranes was 96% at 0.5 MPa (highest among the commercial membranes). Furthermore, Kim et al.²² used cryogenic freezing technology for refinement, where the operating temperatures were -64 °C to -73 °C. Both these technologies produce high purity SF₆ but are energy intensive. Here molecular sieving with GDY membranes at 20 kPa and under ambient conditions was shown. The measured N₂/SF₆ selectivity of GDY membranes could be further explored for potential applications in energy efficient SF₆ recovery.

4.4 Conclusion and Future Directions

I evaluated centimetre-scale GDY membrane by measuring permeance (shown in Figure 4.8) and selectivity (shown in Table 4.1) in a flow cell. Although no significant improvement in selectivity was observed, these measurements provide a baseline for further efforts to create GDY membranes on larger scales. In particular, gaps and defects in the GDY coverage will need to be sealed to prevent non-selective leakage flow from dominating membrane performance.

The major contribution of this chapter is the development of a measurement technique that revealed selective transport of gases through GDY. Permeance of graphene has been measured using a similar method before, but I have extended the technique to measure inherently porous materials. Using the measurement setup, I measured the flow rates of various gases passing through a single flake of GDY. This was done by charging the cavity with gas and monitoring the rate at which the graphene deflates on an AFM. I obtained deflation data for air, nitrogen, sulfur hexafluoride, and methane, which showed significantly higher transport rates for He, Ar, and CH₄ over N₂ and SF₆. Modest selectivity to N₂ over SF₆ was also measured. The permeance and selectivity of GDY flakes likely vary significantly due to variability in thickness and relative orientation of GDY layers. More measurements using different individual flakes should be performed to quantify this variation and understand transport through this material.

The measurement technique could be further modified to improve our ability to resolve high permeances and characterize the structure being measured. Using a smaller diameter hole in graphene to define the flow area could sufficiently reduce the flow rate of smaller gases, facilitating AFM measurement. This could be done using helium ion beam or electron beam milling. Furthermore, performing the measurements on wells created in transmission electron microscope grids may allow for high resolution imaging of the material after AFM measurements.

4.5 References

1. Koenig, S.P.; Wang, L.; Pellegrino, J.; Bunch, J.S. Selective molecular sieving through porous graphene. *Nature nanotechnology* **2012**, *7*, 728-732.
2. Chen, X.; Shen, J.; Hu, Z.; Huo, X. Manufacturing methods and applications of membranes in microfluidics. *Biomedical microdevices* **2016**, *18*, 1-13.
3. Cornelius, T.W.; Apel, P.Y.; Schiedt, B.; Trautmann, C.; Toimil-Molaes, M.E.; Karim, S.; Neumann, R. Investigation of nanopore evolution in ion track-etched polycarbonate membranes. *Nuclear Instruments and Methods in Physics Research Section B: Beam Interactions with Materials and Atoms* **2007**, *265*, 553-557.
4. Cataldo, F.; Ori, O.; Putz, M.V. From graphyne to cata-condensed (Acenographynes) and peri-condensed PAHs-graphyne derivatives. *Fullerenes, Nanotubes and Carbon Nanostructures* **2018**, *26*, 535-544.
5. Huang, C.; Li, Y.; Wang, N.; Xue, Y.; Zuo, Z.; Liu, H.; Li, Y. Progress in research into 2D graphdiyne-based materials. *Chemical reviews* **2018**, *118*, 7744-7803.
6. Yan, H.; Yu, P.; Han, G.; Zhang, Q.; Gu, L.; Yi, Y.; Liu, H.; Li, Y.; Mao, L. High-yield and damage-free exfoliation of layered graphdiyne in aqueous phase. *Angewandte Chemie International Edition* **2019**, *58*, 746-750.
7. Zhang, F.; Liu, G.; Yuan, J.; Wang, Z.; Tang, T.; Fu, S.; Zhang, H.; Man, Z.; Xing, F.; Xu, X. 2D graphdiyne: an excellent ultraviolet nonlinear absorption material. *Nanoscale* **2020**, *12*, 6243-6249.
8. Wang, L.; Boutilier, M.S.; Kidambi, P.R.; Jang, D.; Hadjiconstantinou, N.G.; Karnik, R. Fundamental transport mechanisms, fabrication and potential applications of nanoporous atomically thin membranes. *Nature nanotechnology* **2017**, *12*, 509.
9. Liu, M.; Gurr, P.A.; Fu, Q.; Webley, P.A.; Qiao, G.G. Two-dimensional nanosheet-based gas separation membranes. *Journal of Materials Chemistry A* **2018**, *6*, 23169.
10. Novoselov, K.S.; Geim, A.K.; Morozov, S.V.; Jiang, D.E.; Zhang, Y.; Dubonos, S.V.; Grigorieva, I.V.; Firsov, A.A. Electric field effect in atomically thin carbon films. *Science* **2004**, *306*, 666-669.
11. Van Noorden, R. Production: Beyond sticky tape. *Nature* **2012**, *483*, S32-S33.

12. Li, X.; Zhu, Y.; Cai, W.; Borysiak, M.; Han, B.; Chen, D.; Piner, R.D.; Colombo, L.; Ruoff, R.S. Transfer of large-area graphene films for high-performance transparent conductive electrodes. *Nano letters* **2009**, *9*, 4359-4363.
13. Zhang, G.; Güell, A.G.; Kirkman, P.M.; Lazenby, R.A.; Miller, T.S.; Unwin, P.R. Versatile polymer-free graphene transfer method and applications. *ACS applied materials & interfaces* **2016**, *8*, 8008-8016.
14. Asakawa, H.; Katagiri, Y.; Fukuma, T. Closed fluid cell with liquid-sealing mechanism for stable and flexible operation of liquid-environment atomic force microscopy. *Japanese Journal of Applied Physics* **2013**, *52*, 110109.
15. Jiao, Y.; Du, A. J.; Hankel, M.; Zhu, Z. H.; Rudolph, V.; Smith, S. C. Graphdiyne: A Versatile Nanomaterial for Electronics and Hydrogen Purification. *Chemical Communications* **2011**, *47*, 11843–11845.
16. Freeman, B.; Pinnau, I. Separation of gases using solubility-selective polymers. *Trends in polymer science* **1997**, *5*, 167-173.
17. Thomson, J.J. The forces between atoms and chemical affinity. *The London, Edinburgh, and Dublin Philosophical Magazine and Journal of Science* **1914**, *27*, 757-789.
18. Hencky, H. Über den spannungszustand in kreisrunden platten mit verschwindender. *Biegungssteifigkeit. Z. für Mathematik und Physik* **1915**, *63*, 311-317.
19. Shiojiri, K.; Yanagisawa, Y.; Yamasaki, A.; Kiyono, F. Separation of F-gases (HFC-134a and SF₆) from gaseous mixtures with nitrogen by surface diffusion through a porous Vycor glass membrane. *Journal of membrane science* **2006**, *282*, 442-449.
20. Dervos, C.T.; Vassiliou, P. Sulfur hexafluoride (SF₆): global environmental effects and toxic byproduct formation. *Journal of the Air & Waste Management Association* **2000**, *50*, 137-141.
21. Choi, J.W.; Lee, S.; An, B.; Kim, S.B.; Lee, S.H. Separation of sulfur hexafluoride from a nitrogen/sulfur hexafluoride mixture using a polymer hollow fiber membrane. *Water, Air, & Soil Pollution* **2014**, *225*, 1-9.
22. Kim, K.; Kim, K.S.; Lee, J.E.; Park, S.; Ahn, C.K.; Kim, G.H. Status of SF₆ separation/refining technology development for electric industry in Korea. *Separation and Purification Technology* **2018**, *200*, 29-35.

Chapter 5

5 Mass Advection-Diffusion in Creeping Flow Through an Orifice Plate

5.1 Abstract

Continuum transport equations are commonly applied to nanopores in atomically thin membranes for simple modeling. Although these equations do not apply for nanopores approaching the fluid or solute molecule size, they can be reasonably accurate for larger nanopores. Relatively large graphene nanopores have applications in small particle filtration and appear as unwanted defects in large-area membranes. Solute transport rates through these nanopores determine the rejection performance of the membrane. Atomically thin membranes commonly operate in a regime where advection and diffusion both contribute appreciably to transport. Solute mass transfer rates through larger nanopores have previously been modeled by adding continuum estimates for pure diffusion and pure advection through an infinitesimally thick orifice plate as if the separate contributions were independent. I show here that estimating the transport rate in this way is accurate to within 30% through comparison with numerical solutions. I further derive an expression for the net mass transfer rate in advection-diffusion through an infinitesimal thickness orifice plate at low Reynolds numbers accurate to within 1% for positive Péclet numbers (where diffusion is in the same direction as advection). Based on our expression, I devise an equation for the net mass transfer rate in creeping flow through orifice plates of arbitrary thickness that matches finite volume calculations to within 3% for 18 positive Péclet numbers. Our expressions are found to provide accurate predictions for negative Péclet numbers as well (diffusion opposite advection). These simple but accurate analytical equations for mass transfer rates in creeping flow through an orifice plate will be useful for constructing approximate transport models.

5.2 Introduction

Atomically thin membrane technology is being actively developed for applications including desalination, water purification, petrochemical separations, carbon capture, and natural gas filtration¹. Flow rates tend to decrease as membrane thickness increases, and as

such, membranes made from single atom thick materials such as graphene promise exceptionally high throughput. These membranes accomplish size-based separation through nanopores large enough to allow some species to pass through but small enough to block others. Pores smaller than ~ 1 nm (Fig. 5.1a) can even separate molecules of different sizes. Graphene nanopore selectivity has been demonstrated experimentally for gas molecules², ions^{3,4,5}, and small solute molecules^{6,7}. For pores not much larger than the molecules flowing through them, the continuum laws of fluid mechanics break down even for liquids. Molecular dynamics simulations have been performed for a wide range of solutions and nanopore geometries in atomically thin materials to predict flow rates and solute rejection⁸⁻²¹. Flow through larger graphene nanopores (e.g., Fig. 5.1b, c), of size ~ 5 nm to $1 \mu\text{m}$, has also been measured^{4,5,22}. Membranes with such pores have potential applications in air particulate filtration, nanofiltration, and ultrafiltration.

Furthermore, defects in this size range occur in large-area graphene membranes and cause undesirable, non-selective leakage flow²³⁻²⁵. Transport models for graphene membranes commonly estimate flow rates through defects and larger nanopores using Sampson's analytical solution²⁶ for creeping flow through an infinitesimally thick orifice plate or similar expressions^{6,7,23,27}. Dagan et al.²⁸ extended Sampson's²⁶ expression to provide approximate flow rates through orifice plates of arbitrary thickness. Suk & Aluru⁸ further modified this expression to capture sub-continuum effects for water flows through pores down to ~ 1 nm in size by incorporating fitting parameters to match molecular dynamics simulation results. Sampson's expression²⁶ has also been used to model gas flows through graphene pores of size $\sim 1 \mu\text{m}$ ²². Continuum orifice plate solutions are similarly used to model solute transport through graphene pores. In the absence of flow (zero Péclet number), the species diffusion equation can be solved analytically in cylindrical coordinates for the mass flux²⁹.

Similarly, when advection dominates (high Péclet number), the species flux can be found by multiplying the flow rate through the orifice plate by the upstream concentration. Graphene nanopores commonly operate at low Reynolds number (creeping flow) and Péclet number of order one, where both advection and diffusion are important. Prior studies have approximately modeled this transport by adding the separate advective and diffusive

contributions as if they were independent^{6,7,23,27}. I find here that estimating the species flux through an infinitesimally thick orifice plate in this way is accurate to within 30% for positive Péclet numbers, where diffusion is in the same direction as advection. Furthermore, I derive an expression for the mass flux through an orifice plate in creeping flow that is accurate to within 1% for positive Péclet numbers. This expression is also accurate for negative Péclet numbers, where diffusion opposes advection, and which cannot be handled by approximating advection and diffusion as an independent. I extend this expression to cases of non-zero thickness orifice plates by matching them to finite volume numerical solutions.

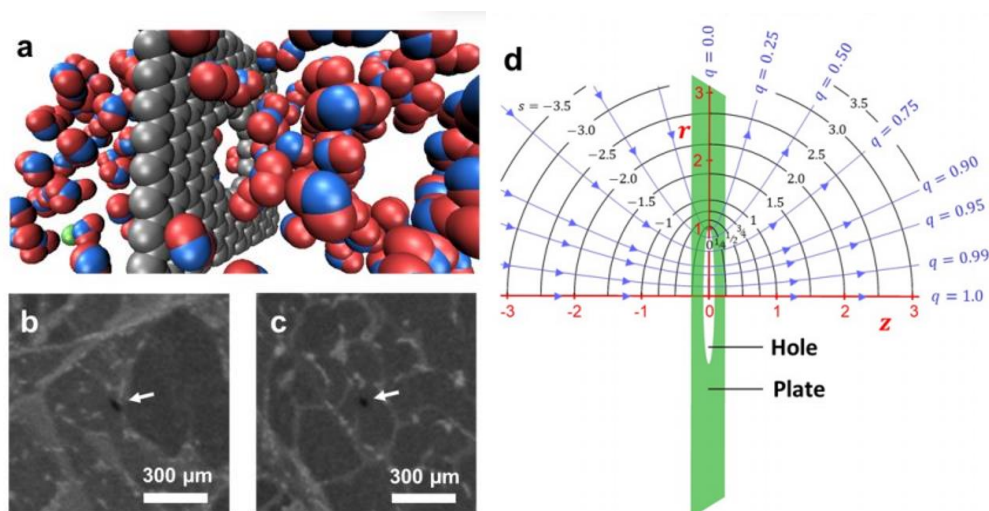


Figure 5.1: Atomically thin membranes. **a.** Illustration of water and solute molecules in the vicinity of a ~ 1 nm graphene pore. **b. and c.** Scanning electron micrograph showing ~ 30 nm pores in few-layer graphene. Pores indicated with white arrows. Images were obtained with a Zeiss LEO 1530 field emission scanning electron microscope at 1 kV accelerating voltage. **d.** Hole in an infinitesimally thick plate with cylindrical and oblate-spheroidal coordinates shown.

Sampson²⁶ showed that the Stokes equations can be solved analytically for pressure driven creeping flow through an infinitesimal thickness orifice plate in the oblate-spheroidal (q - s) coordinate system shown in Fig. 5.1d. This coordinate system is defined in terms of an axisymmetric cylindrical (r - z) coordinate system by $r = \sqrt{(1 + s^2)(1 - q^2)}$ and $z = qs$. Sampson²⁶ showed that curves of constant q are streamlines in this flow and that the average flow speed through the pore (volume flow rate divided by pore area) is,

$$V = \frac{\Delta p D}{6\pi\mu}, \quad (5.1)$$

where D is the hole diameter, μ is the dynamic viscosity, and Δp is the pressure difference from far upstream to far downstream of the hole. Choosing to non-dimensionalize velocities by V and lengths by $D/2$, the velocity components in the r and z directions are,

$$v_r = \frac{3}{2} \frac{q^2 s}{s^2 + q^2} \sqrt{\frac{1-q^2}{1+s^2}} \quad (5.2)$$

and

$$v_z = \frac{3}{2} \frac{q^3}{s^2 + q^2}. \quad (5.3)$$

The steady, non-dimensional species advection-diffusion equation ($\nabla^2 c = \frac{1}{2} Pe \mathbf{v} \cdot \nabla c$) in oblate-spheroidal coordinates for the above velocity field is,

$$\frac{3}{4} Pe q^2 \frac{\partial c}{\partial s} = \frac{\partial}{\partial s} \left[(1 + s^2) \frac{\partial c}{\partial s} \right] + \frac{\partial}{\partial q} \left[(1 - q^2) \frac{\partial c}{\partial q} \right] \quad (5.4)$$

Here, concentration is non-dimensionalized as $c = (c' - c_{\text{Low}}) / (c_{\text{High}} - c_{\text{Low}})$, where c' is the local concentration, c_{High} is the concentration far from the hole on the $z < 0$ side, and c_{Low} is the concentration far from the hole on the $c > 0$ side. \mathbf{v} is the non-dimensional local velocity vector. Péclet number is defined as $Pe = V D / \mathcal{D}$, where \mathcal{D} is the species diffusivity. The Péclet number quantifies the ratio of advective to diffusive mass transfer; I use the convention that $Pe > 0$ corresponds to advection in the same direction as diffusion whereas $Pe < 0$ corresponds to advection being opposite to diffusion.

Our analysis here is restricted to sufficiently dilute solutions or low concentration differences that bulk flow induced by solute concentration gradients is negligible. Here only the solute molecules that do not interact with the membrane except through the impermeability condition are being considered but note that Ref. [30] provides a theoretical treatment of diffusive continuum transport through infinitesimally thick orifice plates accounting for solute-membrane interactions. Although this work is motivated by applications in modeling flow through atomically thin membranes, an attempt to resolve nanoscale effects that emerge for pores similar in size to solute molecules was not made³¹.

The development here is limited to the continuum regime, expected to apply for larger graphene nanopores.

Bauer³² considered Eq. 5.4 for the case of constant wall concentration with diffusion along streamlines being negligible compared to advection. He obtained an infinite series solution for the concentration field in terms of Legendre polynomials. For the membrane system of interest here, an impermeable wall condition (zero gradient normal to the wall) is the appropriate boundary condition, rather than a constant wall concentration. The boundary conditions are thus different constant concentrations far from the membrane on either side,

$$c(q, s \rightarrow -\infty) = 1 \quad (5.5)$$

and

$$c(q, s \rightarrow \infty) = 0 \quad (5.6)$$

and zero flux at the wall,

$$\left. \frac{\partial c}{\partial q} \right|_{q=0} = 0 \quad (5.7)$$

I will furthermore retain the term for diffusion along the streamline in our formulation.

The governing equation and physical system have commonalities with the extended Graetz problem for advection diffusion in a pipe accounting for axial conduction³³⁻³⁶. However, the case examined here is further complicated by variable coefficients in both diffusion terms. I employ an integral transform approach³⁷ to approximately solve this equation, as has similarly been applied to extended Graetz problems with various wall boundary conditions^{38,39}.

I seek a series expansion for the concentration field in terms of Legendre polynomials of the form,

$$c(q, s) = \sum_{n=0,2,4,\dots}^{\infty} \frac{2n+1}{2} \hat{c}_n(s) P_n(q), \quad (5.8)$$

where $P_n(q)$ is the n^{th} degree Legendre polynomial and $\hat{c}_n(s)$ is the corresponding coefficient function. Note that only even terms are included in the expansion to satisfy the impermeability condition (Eq. 5.7). Furthermore, the Legendre polynomials are normalized such that⁴⁰,

$$\int_0^1 P_n(q) P_m(q) dq = \frac{1}{2n+1} \delta_{m,n}, \quad (5.9)$$

where $\delta_{m,n}$ is the Kronecker delta. Using this condition, the expansion coefficients can be defined explicitly in terms of the concentration field as,

$$\hat{c}_n(s) = 2 \int_0^1 c(q, s) P_n(q) dq. \quad (5.10)$$

Multiplying both sides of the governing equation (Eq. 5.4) by an arbitrary Legendre polynomial and integrating converts the partial differential equation into an infinite system of coupled ordinary differential equations for the expansion coefficients,

$$\begin{aligned} & \frac{3}{4} P e \left[\frac{n^2+3n+2}{4n^2+8n+3} \frac{d\hat{c}_{n+2}}{ds} + \frac{2n^2+2n-1}{4n^2+4n-3} \frac{d\hat{c}_n}{ds} + \frac{n^2-n}{4n^2-1} \frac{d\hat{c}_{n-2}}{ds} \right] \\ & = \frac{d}{ds} \left[(1+s^2) \frac{d\hat{c}_n}{ds} \right] - n(n+1)\hat{c}_n(s), \end{aligned} \quad (5.11)$$

for $n = 0, 2, 4, \dots$. Here I define $\hat{c}_{-2}(s) = 0$ to avoid having to treat $n = 0$ as a special case, since no \hat{c}_{-2} term appears in the series expansion (Eq. 5.8). Similarly multiplying Eq. 5.5 and 5.6 by an arbitrary Legendre polynomial and integrating provides boundary conditions on these coefficient functions of $\hat{c}_n(s \rightarrow -\infty) = 2\delta_{0,n}$ and $\hat{c}_n(s \rightarrow \infty) = 0$.

To solve this system of differential equations, the series expansion is first truncated to a finite number of terms, setting all higher order terms to zero. This results in a finite number of equations that can be solved numerically. Integral transform solutions such as this will often converge rapidly without the need for many terms in the series³⁷. The advantage of this approach over directly solving the partial differential equation by, e.g., a finite volume method, is that the ordinary differential equations can be solved with higher accuracy.

To further eliminate the need to truncate the infinite domain of this system in the numerical solution, I transform the system to a finite domain by making the change of variables, $\xi = \arctan s$, which leads to,

$$\begin{aligned} & \frac{3}{4} Pe \left[\frac{n^2+3n+2}{4n^2+8n+3} \frac{d\hat{c}_{n+2}}{d\xi} + \frac{2n^2+2n-1}{4n^2+4n-3} \frac{d\hat{c}_n}{d\xi} + \frac{n^2-n}{4n^2-1} \frac{d\hat{c}_{n-2}}{d\xi} \right] \\ & = \frac{d^2\hat{c}_n}{d\xi^2} - n(n+1)\sec^2(\xi)\hat{c}_n(\xi), \end{aligned} \quad (5.12)$$

with boundary conditions $\hat{c}_n(\xi = -\pi/2) = 2\delta_{0,n}$ and $\hat{c}_n(\xi = \pi/2) = 0$.

5.2.1 Numerical Solution

The system of equations (Eq. 5.12) and boundary conditions formulated in terms of the ξ coordinate were solved numerically with the system truncated to the $n = 20$ term. The resulting equations were discretized using a fourth order finite difference approximation for the derivatives at interior nodes and second order finite difference approximations at the two next-to-boundary nodes. The solution was computed using 100,001 equally spaced ξ values on the interval $-\frac{\pi}{2} \leq \xi \leq \frac{\pi}{2}$.

Figure 5.2a shows the computed concentration field for a range of Péclet numbers and Fig. 5.2b shows the corresponding concentration profiles along the z -axis for each value. For the case of pure diffusion ($Pe = 0$) the concentration field is symmetric about the plane of the orifice plate. Appreciable variation in concentration is localized to within a few diameters of the hole. As the magnitude of Péclet number increases, species advection toward the hole raises the concentration near the hole on the upstream side, where the flow converges. The size of the region upstream of the hole over which significant concentration variation occurs also decreases. The downstream side continues to display a more gradual variation in concentration as the flow diverges away from the hole. The greater advection carries the upstream concentration farther away from the hole, enlarging the downstream region over which concentration varies appreciably. The concentration field becomes asymmetric as the magnitude of Pe increases. These trends continue as Péclet number rises and at $Pe = \pm 10$, strong advection leads to a nearly uniform concentration field upstream of the hole.

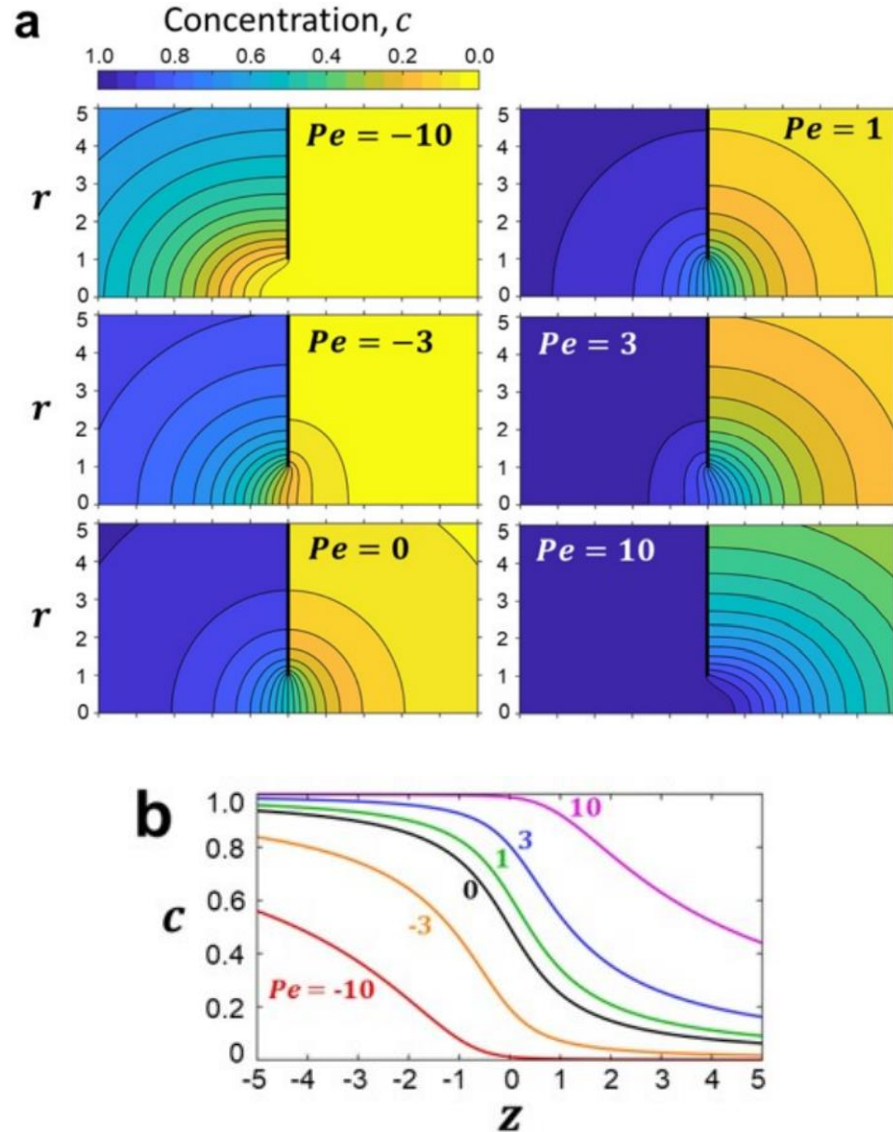


Figure 5.2: Concentration field computed numerically by truncating the series expansion after the $n = 20$ term. **a** Concentration field for various Péclet numbers. **b** Concentration profiles along the z axis.

Figure 5.3a shows the coefficient functions for four of the lowest order terms in the series. Most of the concentration field is captured by the lowest order term, as seen by the rapidly decreasing magnitude of these coefficients with Legendre polynomial order in Fig. 5.3b. The $Pe = 0$ case is exactly solved with only the first term (\hat{c}_0) being non-zero. As Péclet number increases, the importance of higher order terms increases, though the second largest term is still an order of magnitude smaller than the leading order term for $Pe = \pm 10$ (Fig. 5.3b).

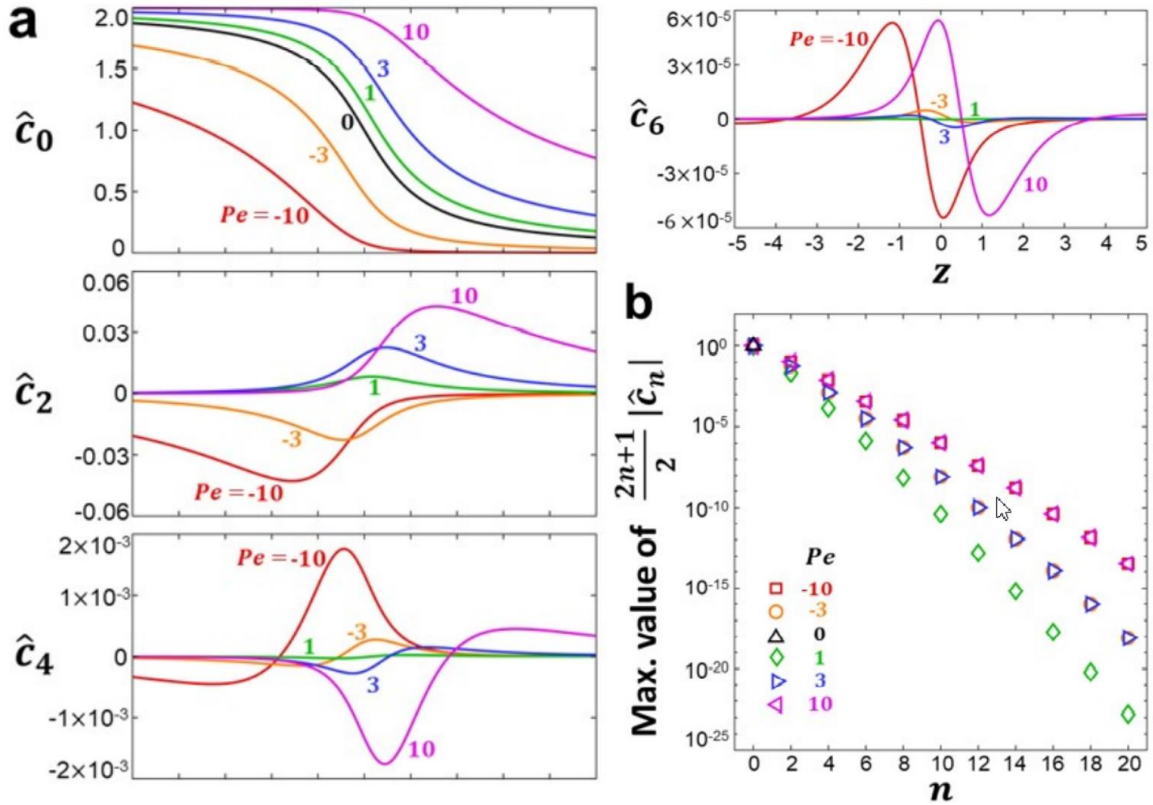


Figure 5.3: Expansion coefficients and convergence. **a** Calculated expansion coefficient plotted along the z axis for the first 4 terms in the series expansion truncated after the $n = 20$ term. **b** Maximum absolute value of each expansion coefficient over all r and z for different Péclet numbers, showing the diminishing contribution of higher order terms.

Our primary interest is in the net mass transfer rate across the orifice plate, \dot{m} . I present this in non-dimensional form by defining a Sherwood number as,

$$Sh = \frac{(\dot{m} - AVc_{Low})D}{AD\Delta c}, \quad (5.13)$$

where $A = \pi D^2 / 4$ is the hole area and $\Delta c = c_{High} - c_{Low}$. Accounting for advective and diffusive transport through the hole, in q - s coordinates the Sherwood number is calculated as

$$Sh = 2 Pe \int_0^1 v_z(q, s=0) c(q, s=0) q dq - 4 \int_0^1 \left. \frac{\partial c}{\partial s} \right|_{s=0} dq \quad (5.14)$$

Substituting in the series expansion for the concentration field (Eq. 5.8) leads to,

$$Sh = Pe \left(\frac{\hat{c}_0(s=0)}{2} + \hat{c}_2(s=0) \right) - 2 \left. \frac{d\hat{c}_0}{ds} \right|_{s=0} \quad (5.15)$$

Sherwood number can be calculated directly from this expression with the numerical solutions for \hat{c}_0 and \hat{c}_2 . Table 5.1 and Fig. 5.4 present the numerically computed values of Sherwood number for a range of Péclet numbers. The solution matches the expected limits of $Sh = 4/\pi$ for pure diffusion at $Pe = 0$, and $Sh = Pe$ for pure advection at $Pe \gg 1$. By comparison with this numerical solution, I find that the simple approximate approach of adding the mass transfer rates for pure advection and pure diffusion is accurate to within 30% for $Pe > 0$. Errors of over 20% occur for $1 \leq Pe \leq 6$.

I note that grid independence of the values of Sherwood number presented in Table 5.1 and Fig. 5.4 was verified by repeating the calculations with half the number of grid points and again with 6 terms in the series expansion instead of 11. Differences in Sherwood numbers remained less than 1×10^{-6} . Sherwood numbers were also calculated in s coordinates by solving Eq. 5.11 with the same number of terms and grid spacing, truncating the infinite domain to $-1000 \leq s \leq 1000$. Sherwood numbers remained within 0.001 of the values computed in terms of the ξ coordinate. The values were further confirmed by finite volume calculations.

Table 5.1: Sh vs. Pe computed for a series expansion truncated after the $n = 20$ term. Pe is read from the first row and column and the Sh value is recorded in the corresponding cell of the table.

Pe	X									
	0	1	2	3	4	5	6	7	8	9
-9.X	0.026	0.025	0.025	0.024	0.023	0.022	0.021	0.020	0.020	0.019
-8.X	0.039	0.037	0.036	0.034	0.033	0.032	0.031	0.029	0.028	0.027
-7.X	0.057	0.055	0.053	0.051	0.049	0.047	0.045	0.043	0.042	0.040
-6.X	0.087	0.084	0.080	0.077	0.074	0.071	0.068	0.065	0.062	0.060
-5.X	0.135	0.130	0.124	0.119	0.113	0.108	0.104	0.099	0.095	0.091
-4.X	0.214	0.204	0.195	0.186	0.178	0.170	0.162	0.155	0.148	0.142
-3.X	0.340	0.324	0.310	0.296	0.282	0.269	0.257	0.245	0.234	0.224
-2.X	0.540	0.516	0.492	0.470	0.449	0.429	0.409	0.391	0.373	0.356
-1.X	0.842	0.807	0.772	0.739	0.707	0.676	0.647	0.618	0.591	0.565
-0.X	—	1.224	1.176	1.130	1.084	1.041	0.998	0.957	0.918	0.879
0.X	1.273	1.324	1.376	1.430	1.484	1.541	1.598	1.657	1.718	1.779
1.X	1.842	1.907	1.972	2.039	2.107	2.176	2.247	2.318	2.391	2.465
2.X	2.540	2.616	2.692	2.770	2.849	2.929	3.009	3.091	3.173	3.256
3.X	3.340	3.424	3.510	3.596	3.682	3.769	3.857	3.945	4.034	4.124
4.X	4.214	4.304	4.395	4.486	4.578	4.670	4.762	4.855	4.948	5.042
5.X	5.135	5.230	5.324	5.419	5.513	5.608	5.704	5.799	5.895	5.991
6.X	6.087	6.184	6.280	6.377	6.474	6.571	6.668	6.765	6.862	6.960
7.X	7.057	7.155	7.253	7.351	7.449	7.547	7.645	7.743	7.842	7.940
8.X	8.039	8.137	8.236	8.334	8.433	8.532	8.631	8.729	8.828	8.927
9.X	9.026	9.125	9.225	9.324	9.423	9.522	9.621	9.720	9.820	9.919
1X	10.018	11.013	12.009	13.007	14.005	15.004	16.003	17.002	18.002	19.001
X0	—	—	20.001	30.000	40.000	50.000	60.000	70.000	80.000	90.000

5.2.2 Leading Order Solution

Most of the value of concentration is captured by the leading order term in the series expansion (Fig. 5.3b). I examine the accuracy of the solution if only this first term is retained in the series expansion, since doing so results in a simple analytical solution. Eq. 5.11 becomes,

$$\frac{Pe}{4} \frac{d\hat{c}_0}{ds} = \frac{d}{ds} \left[(1 + s^2) \frac{d\hat{c}_0}{ds} \right], \quad (5.16)$$

with boundary conditions $\hat{c}_0(s \rightarrow -\infty) = 2$ and $\hat{c}_0(s \rightarrow \infty) = 0$. The solution to these equations is,

$$\hat{c}_0(s) = \frac{2 \left[\exp\left(\frac{Pe}{4} \arctan s\right) - \exp\left(\frac{\pi Pe}{8}\right) \right]}{\exp\left(\frac{-\pi Pe}{8}\right) - \exp\left(\frac{\pi Pe}{8}\right)}, \quad (5.17)$$

and leads to an approximate expression for Sherwood number of,

$$Sh = \frac{Pe}{1 - \exp\left(-\frac{\pi}{4}Pe\right)}. \quad (5.18)$$

This expression is plotted in Fig. 5.4 with the full numerical solution. It is accurate to within 1% over all positive Péclet numbers. The Sherwood number approaches zero for negative Péclet numbers with large magnitude and the relative error in this expression diverges. However, the absolute error remains below 0.04. This expression matches the limits of $Sh = 4/\pi$ at $Pe = 0$ (obtained using the first term of the McLaurin series) and $Sh = Pe$ at $Pe \gg 1$. Eq. 5.18 accurately captures the trend of $Sh \rightarrow 0$ as $Pe \rightarrow -\infty$ that is missed when the advective and diffusive mass transfer rates are simply added as if they were independent for negative Péclet numbers. It provides an accurate estimate for the mass transfer rate through an infinitesimally thick orifice plate over all Péclet numbers in a simple form that will be useful in constructing transport models.

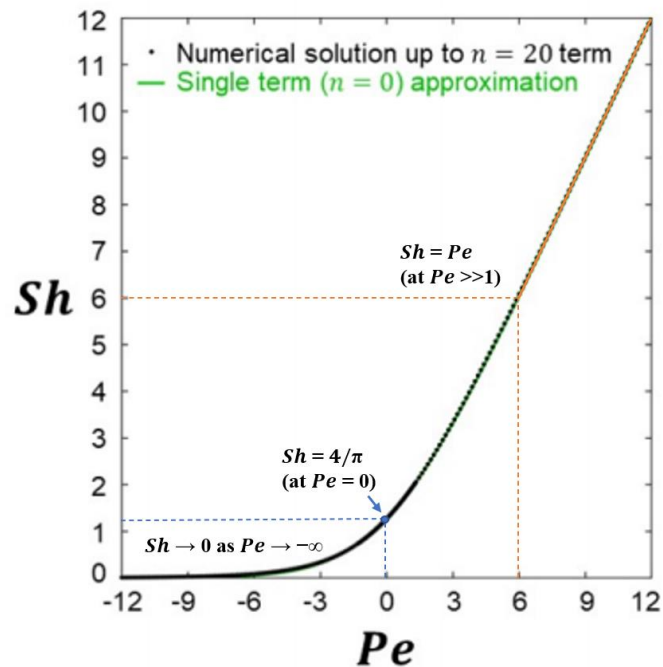


Figure 5.4: Sherwood number dependence on Péclet number of an infinitesimally thick orifice plate. Markers show numerical calculation for a series expansion truncated after the $n = 20$ term. Solid curve shows the analytical approximation obtained by truncating the series expansion to one term (Eq. 5.18). The dotted lines show the three cases that represent the approximate expression.

5.3 Non-Zero Thickness Orifice Plates

I now consider orifice plates of arbitrary thickness. Even for single atom thick graphene membranes, when the hole diameter is not much larger than the thickness of graphene ($\sim 0.34 \text{ nm}^{41}$), approximating the membrane as being infinitesimally thick may not be appropriate. Suk & Aluru⁸ accounted for the finite aspect ratio of the graphene pore when comparing water flow rates from a continuum orifice plate model to molecular dynamics calculations for graphene nanopores. They used as a starting point the model that Dagan et al.²⁸ developed for Stokes's flow through a finite aspect ratio hole. Dagan et al.²⁸ showed that taking the resistance to flow through an infinitesimal orifice plate, derived by Sampson²⁶, in series with the Poiseuille resistance for laminar flow in a long pipe (e.g., Ref. [42, 43]), provides predictions of flow rates accurate to within 1% for all finite aspect ratios. The expression for average velocity through the hole that they derived is,

$$V = \frac{D\Delta p}{\mu\left(6\pi+32\frac{L}{D}\right)}, \quad (5.19)$$

where L is the plate thickness (Fig. 5.5a inset). Here I devise an equivalent expression for mass advection-diffusion through a non-zero thickness orifice plate.

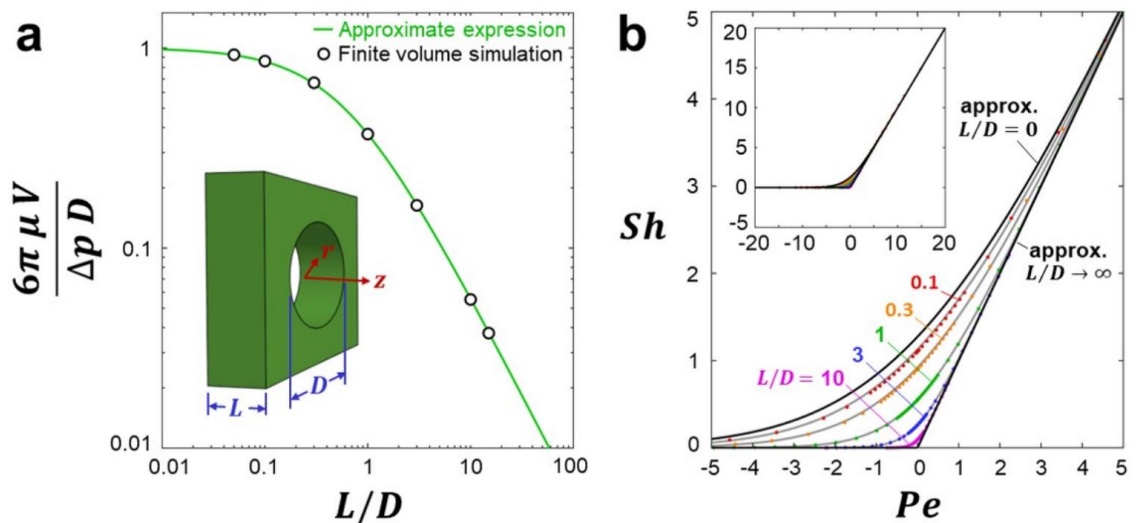


Figure 5.5: Mass transfer rate through an orifice plate of non-zero thickness. **a** Mean flow rate vs. aspect ratio computed by finite volume simulations (markers) compared to the approximate expression of Dagan et al.²⁸ (Eq. 5.19, solid curve). Inset shows a sketch

of the orifice plate geometry. **b** Sherwood number dependence on Péclet number for various hole aspect ratios. Markers show finite volume simulation results whereas curves show the approximate fit from Eq. 5.22 for the same aspect ratios.

5.4 Computational Fluid Dynamics (CFD)

CFD is a branch of fluid mechanics that uses numerical analysis to analyze and solve problems related to fluid flow, chemical reactions, heat and mass transfer, and other related phenomena. CFD is used when an engineering problem cannot be solved using an experimental or analytical approach⁴⁴. It can also complement the experimental approach by reducing total effort and the required cost. With CFD, one can write their own code or use commercially available software such as ANSYS Fluent and OpenFOAM. There are three main elements in commercial CFD packages: a pre-processor, a solver, and a post-processor⁴⁵. In the pre-processor step, the geometry and a mesh are created. After which, the solver numerically solved the fluid flow equations in the computational domain. In the post-processor step, the results of the simulation are analyzed. Moreover, three basic methods of solving CFD problems are finite difference, finite volume⁴⁶, and finite element method⁴⁷. In the finite difference method, conservation equations in differential form (discretized on a mesh) are used, resulting in one algebraic equation for each grid node⁴⁵. In the finite volume method, the integral form of the conservation equations is used⁴⁶. Thus, the domain is divided into small control volumes (CVs), and the conservation equations are applied to each CV, resulting in the production of one algebraic equation per CV. The finite element method and finite volume method are similar, but the finite element method uses weight functions before integrating the equations⁴⁷.

5.4.1 ANSYS Fluent

ANSYS Fluent is one of the popular commercially available CFD software packages. ANSYS CFD solvers are based on the finite volume method⁴⁸. The fluid region of the box in Fig 5.6b is discretized into a finite set of CVs (also called the mesh), and general transport equations for mass, momentum, energy, etc., are solved on this set of control volumes. The partial differential equations are then discretized into a system of algebraic equations, which are then solved numerically to provide the solution field⁴⁶. In pre-

processing, geometry is created or imported into ANSYS. A mesh is then generated, which divides the geometry into elements. Next, the physics and solver are set up by inputting appropriated boundary conditions, materials, and their properties and selecting physical models (e.g., laminar). The solver then computes the solution and solves equations iteratively until convergence. Convergence is achieved when quantities of interest such as pressure drop have reached steady values, overall property conservation is achieved, and changes in variables between the iterations are negligible⁴⁸. The accuracy of this converged solution depends on appropriate and accurate physical models and mesh resolution. A low mesh quality can produce poor simulation results and even divergence.

This software package was initially used to simulate mass transfer rates in creeping flow through an orifice plate. I used 3200 grid points to create a geometry with a hole diameter of 0.4 mm and the wall lengths of 2 mm. The velocity field values were obtained, and flow rates in the x and r direction were calculated. The calculated volume flow rate was 0.002L/s, and the Sampson equation gives 0.00333L/s, which gives a 40% error. Hence, further grid refinement was needed near the pore to converge the flow rate to the Sampson equation. However, the student version of the software package limited the grid refinement of the mesh, thus producing results with a more significant percent error.

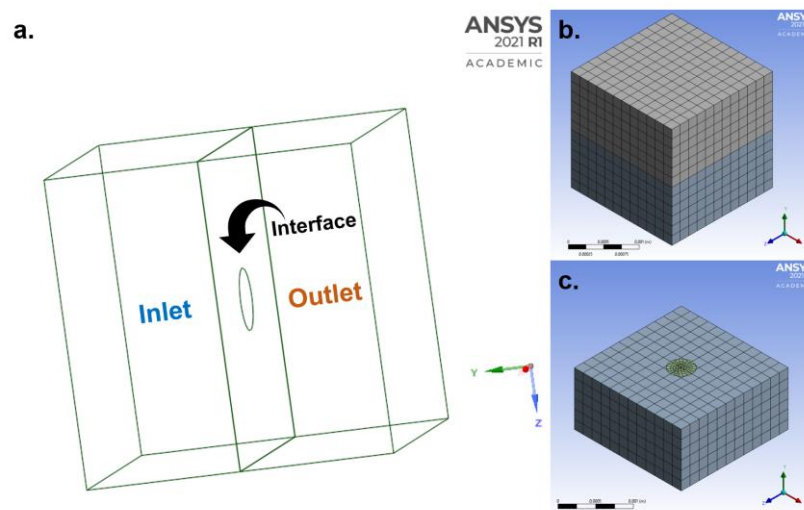


Figure 5.6: Ansys Fluent **a.** Geometry (wireframe mode) of the system consisting of **inlet**, **outlet**, and planar interface. **b.** Meshed geometry **c.** Meshed geometry with outlet removed.

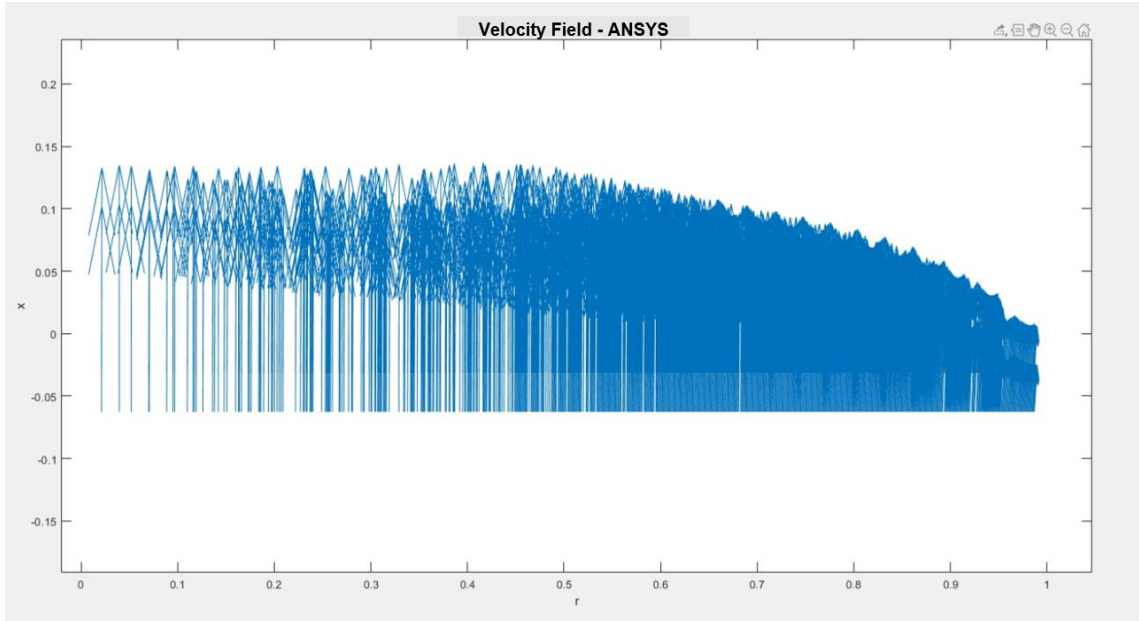


Figure 5.7: A quiver plot (MATLAB) of velocity field in the r and z direction as obtained from ANSYS.

5.4.2 OpenFOAM

OpenFOAM is a free and open-source CFD package that uses the finite volume method to discretize and solve complex fluid dynamic problems. The software runs on Linux systems and uses C++ as its programming language⁴⁹. Like ANSYS Fluent, a three-dimensional volume is created and divided into small volumes (mesh). After which, the initial and boundary conditions are defined and applied to the geometry⁴⁶.

OpenFOAM can use the finite volume method over a collocated grid or a staggered grid. In a staggered grid, scalar variables (e.g., pressure, density) are stored at the cell centers of CVs, whereas the velocity or momentum variables are at the cell faces⁵⁰. On the contrary, a collocated grid arrangement stores all its variables at the cell center, and the same CVs are used for all variables, minimizing the computational effort. An advantage of the staggered grid is the coupling of pressure and velocities, which helps avoid convergence issues and oscillations in pressure or velocity fields^{49,50}.

A *case* folder contains all the information about the geometry, flow conditions, physical parameters set by the user and the computational schemes, and the time-step used in the simulation⁵¹. In a *case* folder, there are three sub-folders: *0* folder, *control* folder, and the

system folder. In the *0* folder, boundary and initial conditions are set up. The *control* folder holds information about the mesh (in the sub-folder *polyMesh*) as well as physical fluid properties (sub-folder *transportProperties*) and models used in the solution. The *system* folder encompasses information about the computational schemes, time-step, and duration of the simulation (*controlDict* file). The linear algebraic solvers definition and tolerance are set in the *fvSolution* file, and the numerical discretization schemes are in the *fvSchemes* file. Moreover, Paraview was used to visualize the solutions produced by OpenFOAM.

To simulate mass transfer rates in creeping flow, a geometry had to be either coded into the *system* folder or imported. As the geometry and the mesh were complex to be coded in, a MATLAB script was used to generate the mesh. Fig 5.8 shows the cross-section in the plane of the wall with different regions of the mesh. The MATLAB code takes as input the sizes of these regions to refine the grid non-uniformly. After which, the *simpleFoam* solver was used for the flow field calculations. This is a steady-state solver for incompressible, turbulent flow and uses the SIMPLE (Semi-Implicit Method for Pressure Linked Equations) algorithm. Note that the turbulence was turned off in the solver parameters. After the calculation run, volume flow rate for each face (top, bottom, side-in, and side-out) was found and the total flow rate was calculated by adding the top and the side-in values together. The input files ran for $\frac{dP}{\rho} = 1m^2 / s^2$ (where dP is differential pressure and ρ is density) and a kinematic viscosity of $100 m^2/s$. For this, the Sampson equation gave a flow rate of 0.003333 L/s. Table 5.2 shows the total flow rate for increasing grid refinement, with the highest number of finite volumes being 810 and the calculated percent error with respect to the Sampson equation.

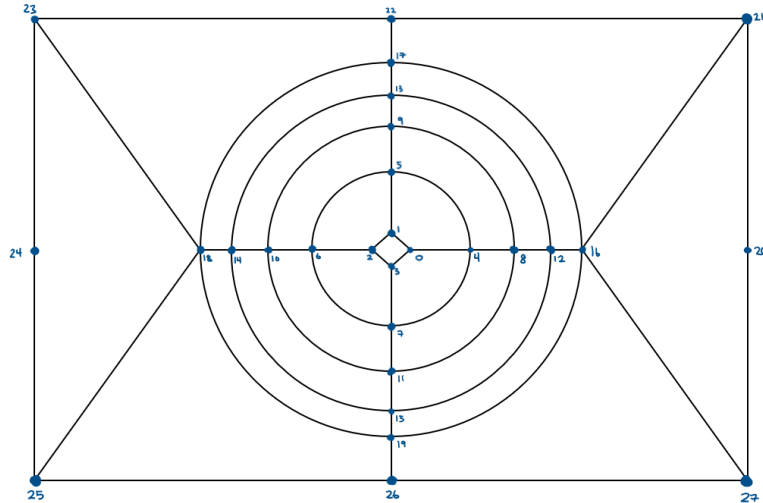


Figure 5.8: Drawing of cross-section in the plane of the wall showing the different regions of the mesh that can be refined non-uniformly.

Table 5.2: Total flow rates obtained from the simulation for increasing grid refinement (# of finite volumes) and the calculated percent error with respect to the Sampson equation.

# of Finite Volumes	Total Flow Rate	% Error
405	0.003297	1.09
540	0.002679	19.63
810	0.002108	36.76

To improve the percent error, r and z values of the cylindrical coordinates in the geometry were varied, and for each variation, the grid refinement was also varied. However, this did not improve the error. Moreover, while creating a non-uniform pressure field, convergence issues arose in OpenFOAM. A possible reason was the presence of sharp edges, to which layers were added to round out the edges but that did not help. Furthermore, OpenFOAM does not take advantage of the cylindrical symmetry of this flow, instead discretizing the domain in Cartesian coordinates. This may also have contributed to the volume flow rate not converging with grid refinement. For these reasons, I decided against using the OpenFOAM solution and instead programmed a finite volume solver for axisymmetric creeping flow.

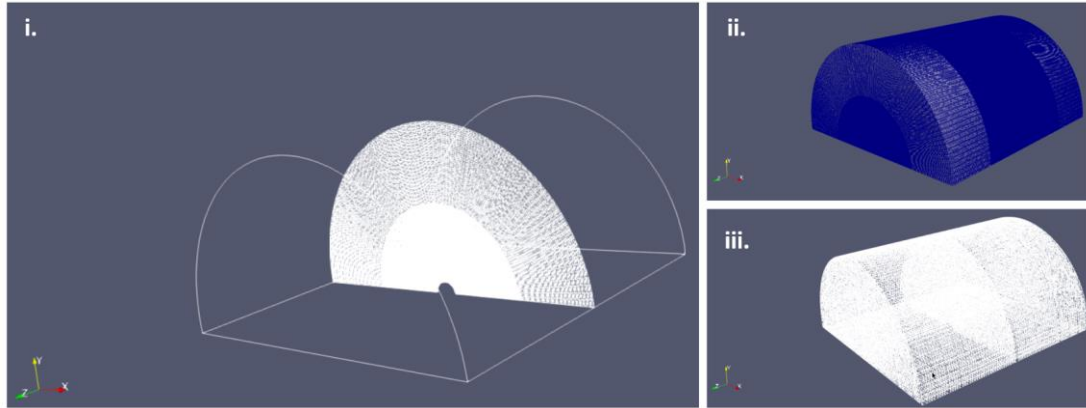


Figure 5.9: Paraview images of the meshed geometry. **i.** Featured edges **ii.** Meshed surface **iii.** Wireframe.

5.5 Finite Volume Solution with Cylindrical Symmetry

I begin by calculating the rate of mass transfer through orifice plates of various aspect ratios by finite volume simulations. For each pore aspect ratio, I solved the Stokes equations in two-dimensional axisymmetric cylindrical coordinates using a staggered grid⁵⁰, truncating the domain to 15-hole radii from the center of the hole inlet in both the r and z directions. A uniform grid with 3900 points in r and 3900 points in z was used over this region outside the hole. The same uniform grid spacing was used in the interior of the hole as well. Second order central difference approximations were used to calculate viscous stresses. Figure 5.5a compares the values of flow rate computed by the finite volume solver (markers) to the predictions of Eq. 5.19 (solid curve) as validation of the simulations.

Once the flow field was calculated, it was used in the species advection-diffusion equation to solve for the concentration field, again using an axisymmetric cylindrical coordinate system. The species diffusion term was approximated using a second order central difference scheme. The species advection term was approximated with a second order central difference scheme for local grid Péclet numbers less than 2 and an upwind scheme for larger grid Péclet numbers.

The markers plotted in Fig. 5.5b show the calculated relationship between Sherwood number and Péclet number for orifice plates of various aspect ratios. Note that for finite thickness orifice plates, I have used the average flow speed through that orifice plate to

calculate Sherwood and Péclet number, rather than Eq. 5.1, which applies to infinitesimal orifice plates. The top and bottom curves show limiting cases of an infinitesimal plate ($L/D = 0$) and a long pipe ($L/D \rightarrow \infty$). In both limits, $Sh \approx Pe$ for $Pe \gg 1$ and $Sh \rightarrow 0$ as $Pe \rightarrow -\infty$. Sherwood numbers for all simulated aspect ratios fall between these limit curves and approach the same $Pe \rightarrow \pm\infty$ limits.

Figure 5.10a shows the flow field for each aspect ratio simulated and Fig. 5.10b shows the corresponding concentration field for the $Pe = 1$ case. As observed for the infinitesimal plate case (Fig. 5.2a), at low L/D ratios, for $Pe \sim 1$ the concentration field only varies significantly within a region a few radii from the hole. Appreciable variations in the velocity field are similarly confined to a few radii from the hole. However, as the L/D ratio increases, the resistance to mass transfer through the hole increases in comparison to the access resistance outside of the hole. As a result, the concentrations just outside of the pore on either side approach their respective distant reservoir values, and all the concentration variation occurs within the hole.

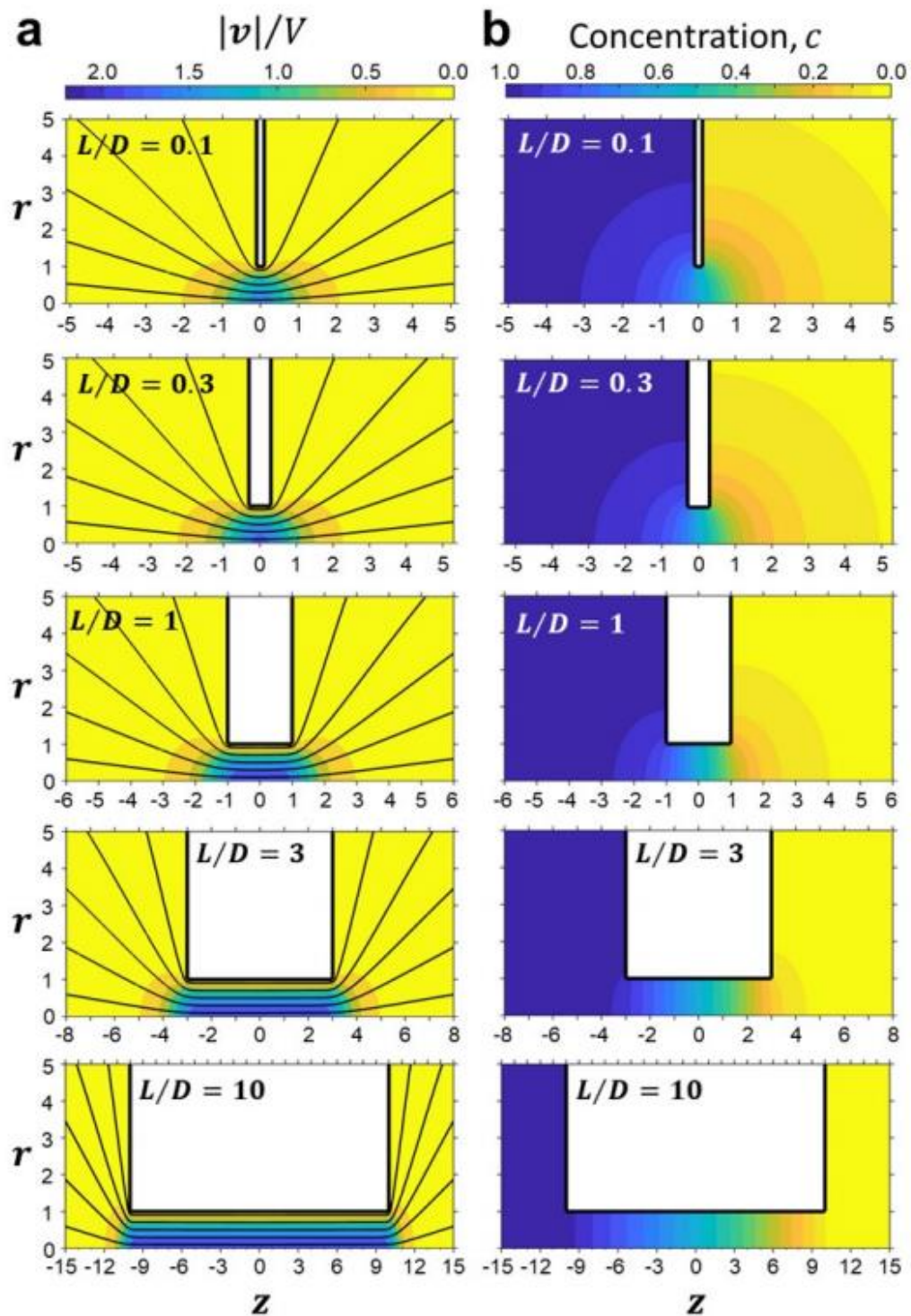


Figure 5.10: Flow fields and concentration fields from finite volume simulations for non-zero thickness plates of various aspect ratios. **a** Local flow speed ($|v|$) normalized by average flow speed through the pore. Solid curves show streamlines. **b** Concentration field.

5.5.1 Approximate Sherwood Number Expression

For an infinitesimal thickness plate, the Sherwood number is accurately approximated by Eq. 5.18. In the other extreme, for a very long pipe with fixed concentrations at either end, the Sherwood number is given approximately by,

$$Sh = \frac{Pe}{1 - \exp\left(-\frac{L}{D}Pe\right)} \quad (5.20)$$

The Sherwood number expressions have similar form in both L/D limits, motivating us to develop an expression of similar form for orifice plates with arbitrary aspect ratios.

I construct the expression such that it (1) recovers the $Sh = Pe$ limit expected for $Pe \gg 1$, (2) results in $Sh \rightarrow 0$ as $Pe \rightarrow -\infty$, (3) returns to Eq. 5.18 for an infinitesimal plate when $L/D = 0$, (4) approaches Eq. 5.20 for a long pipe when $L/D \gg 1$, and (5) matches an approximate resistance model for pure diffusion when $Pe = 0$. For the resistance model in point (5), I note that as $Pe \rightarrow 0$, the Sherwood number for an infinitesimal plate (Eq. 5.18) becomes $Sh = 4/\pi$ and that for a long pipe (Eq. 5.20) becomes $Sh = D/L$. Modeling a finite aspect ratio orifice plate as an equivalent circuit consisting of the access resistance for an infinitesimal plate in series with the pipe resistance in the hole provides a Sherwood number estimate at $Pe = 0$ of,

$$Sh = \frac{1}{\frac{\pi}{4} + \frac{L}{D}} \quad (5.21)$$

I can match this $Pe = 0$ value while satisfying the other proposed requirements by approximating the Sherwood number as,

$$Sh = \frac{Pe}{1 - \exp\left[-Pe\left(\frac{\pi}{4} + \frac{L}{D}\right)\right]} \quad (5.22)$$

This expression is plotted as solid curves for each aspect ratio simulated in Fig. 5.5b. For all 245 Péclet number - aspect ratio pairs simulated, including those plotted in Fig. 5.5b, the expression matches our finite volume calculations to within 3% for $Pe \geq 0$ and to within 0.04 for $Pe < 0$. Eq. 5.22 is a simple but accurate expression for the mass transfer rate through a finite aspect ratio orifice plate under creeping flow conditions.

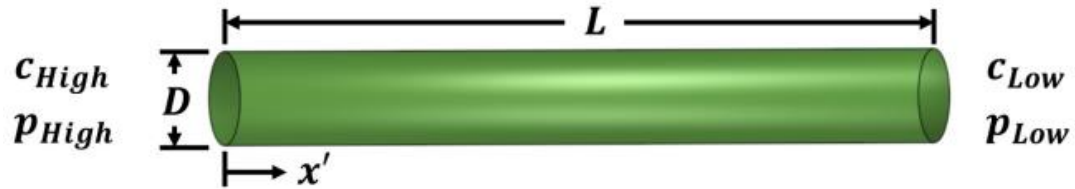


Figure 5.11: Dimensions and coordinate system definition for advection-diffusion in a long pipe.

Note that further details and derivations can be found in the Supplementary Information section of Ref [52].

5.6 Conclusion

An integral transform approach was used to precisely calculate mass advection-diffusion rates in creeping flow through an infinitesimally thick orifice plate. By including only the leading order term in the series expansion, an analytical expression for this mass transfer rate was obtained that is accurate to within 1% for positive Péclet numbers (where advection and diffusion are in the same direction) and maintains low absolute error for negative Péclet numbers (where diffusion is opposite advection). This equation offers an improvement overestimating the mass transfer rate by simply adding the advective and diffusive values as if they were independent, which can be in error by up to almost 30% for $Pe > 0$. Moreover, finite volume calculations were presented for mass advection-diffusion in creeping flow through orifice plates of various aspect ratios and an approximate expression for the mass transfer rate was proposed that matches our simulation results to within 3% for positive Péclet numbers. The main outcomes of this chapter are Eq. 5.18 and 5.22, which accurately approximate the dependence of Sherwood number on Péclet number for creeping flow through an infinitesimally thick orifice plate and orifice plates of arbitrary aspect ratio. They provide simple analytical expressions for use in transport modeling and act as a reference point for examining deviations from continuum solute transport rates in nanopores.

5.7 References

1. Wang, L.; Boutilier, M.S.; Kidambi, P.R.; Jang, D.; Hadjiconstantinou, N.G.; Karnik, R. Fundamental transport mechanisms, fabrication and potential applications of nanoporous atomically thin membranes. *Nature nanotechnology* **2017**, *12*, 509-522.
2. Koenig, S.P.; Wang, L.; Pellegrino, J.; Bunch, J.S. Selective molecular sieving through porous graphene. *Nature nanotechnology* **2012**, *7*, 728-732.
3. Jain, T.; Rasera, B.C.; Guerrero, R.J.S.; Boutilier, M.S.; O'hern, S.C.; Idrobo, J.C.; Karnik, R. Heterogeneous sub-continuum ionic transport in statistically isolated graphene nanopores. *Nature nanotechnology* **2015**, *10*, 1053-1057.
4. Rollings, R.C.; Kuan, A.T.; Golovchenko, J.A. Ion selectivity of graphene nanopores. *Nature communications* **2016**, *7*, 1-7.
5. Cantley, L.; Swett, J.L.; Lloyd, D.; Cullen, D.A.; Zhou, K.; Bedworth, P.V.; Heise, S.; Rondinone, A.J.; Xu, Z.; Sinton, S.; Bunch, J.S. Voltage gated inter-cation selective ion channels from graphene nanopores. *Nanoscale* **2019**, *11*, 9856-9861.
6. O'Hern, S.C.; Jang, D.; Bose, S.; Idrobo, J.C.; Song, Y.; Laoui, T.; Kong, J.; Karnik, R. Nanofiltration across defect-sealed nanoporous monolayer graphene. *Nano letters* **2015**, *15*, 3254-3260.
7. Cheng, P.; Kelly, M.M.; Moehring, N.K.; Ko, W.; Li, A.P.; Idrobo, J.C.; Boutilier, M.S.; Kidambi, P.R. Facile size-selective defect sealing in large-area atomically thin graphene membranes for sub-nanometer scale separations. *Nano Letters* **2020**, *20*, 5951-5959.
8. Suk, M.E.; Aluru, N.R. Molecular and continuum hydrodynamics in graphene nanopores. *RSC advances* **2013**, *3*, 9365-9372.
9. Cohen-Tanugi, D.; Grossman, J.C. Water desalination across nanoporous graphene. *Nano letters* **2012**, *12*, 3602-3608.
10. Gai, J.G.; Gong, X.L. Zero internal concentration polarization FO membrane: functionalized graphene. *Journal of Materials Chemistry A* **2014**, *2*, 425-429.
11. Gai, J.G.; Gong, X.L.; Wang, W.W.; Zhang, X.; Kang, W.L. An ultrafast water transport forward osmosis membrane: porous graphene. *Journal of Materials Chemistry A* **2014**, *2*, 4023-4028.
12. Heiranian, M.; Farimani, A.B.; Aluru, N.R. Water desalination with a single-layer MoS₂ nanopore. *Nature communications* **2015**, *6*, 1-6.

13. Zhu, C.; Li, H.; Zeng, X.C.; Wang, E.G.; Meng, S. Quantized water transport: ideal desalination through graphyne-4 membrane. *Scientific reports* **2013**, *3*, 1-7.
14. Xue, M.; Qiu, H.; Guo, W. Exceptionally fast water desalination at complete salt rejection by pristine graphyne monolayers. *Nanotechnology* **2013**, *24*, 505720.
15. Kou, J.; Zhou, X.; Chen, Y.; Lu, H.; Wu, F.; Fan, J. Water permeation through single-layer graphyne membrane. *The Journal of chemical physics* **2013**, *139*, 064705.
16. Lin, L.C.; Choi, J.; Grossman, J.C. Two-dimensional covalent triazine framework as an ultrathin-film nanoporous membrane for desalination. *Chemical Communications* **2015**, *51*, 14921-14924.
17. Song, Z.; Xu, Z. Ultimate osmosis engineered by the pore geometry and functionalization of carbon nanostructures. *Scientific reports* **2015**, *5*, 1-9.
18. Lin, S.; Buehler, M.J. Mechanics and molecular filtration performance of graphyne nanoweb membranes for selective water purification. *Nanoscale* **2013**, *5*, 11801-11807.
19. Kou, J.; Zhou, X.; Lu, H.; Wu, F.; Fan, J. Graphyne as the membrane for water desalination. *Nanoscale* **2014**, *6*, 1865-1870.
20. Cohen-Tanugi, D.; Lin, L.C.; Grossman, J.C. Multilayer nanoporous graphene membranes for water desalination. *Nano letters* **2016**, *16*, 1027-1033.
21. Cohen-Tanugi, D.; Grossman, J.C. Water permeability of nanoporous graphene at realistic pressures for reverse osmosis desalination. *The Journal of chemical physics* **2014**, *141*, 074704.
22. Celebi, K.; Buchheim, J.; Wyss, R.M.; Droudian, A.; Gasser, P.; Shorubalko, I.; Kye, J.I.; Lee, C.; Park, H.G. Ultimate permeation across atomically thin porous graphene. *Science* **2014**, *344*, 289-292.
23. O'Hern, S.C.; Stewart, C.A.; Boutilier, M.S.; Idrobo, J.C.; Bhaviripudi, S.; Das, S.K.; Kong, J.; Laoui, T.; Atieh, M.; Karnik, R. Selective molecular transport through intrinsic defects in a single layer of CVD graphene. *ACS nano* **2012**, *6*, 10130-10138.
24. Boutilier, M.S.; Sun, C.; O'Hern, S.C.; Au, H.; Hadjiconstantinou, N.G.; Karnik, R. Implications of permeation through intrinsic defects in graphene on the design of defect-tolerant membranes for gas separation. *ACS nano* **2014**, *8*, 841-849.

25. Boutilier, M.S.; Jang, D.; Idrobo, J.C.; Kidambi, P.R.; Hadjiconstantinou, N.G.; Karnik, R. Molecular sieving across centimeter-scale single-layer nanoporous graphene membranes. *ACS nano* **2017**, *11*, 5726-5736.
26. Sampson, R.A. XII. On Stokes's current function. *Philosophical Transactions of the Royal Society of London.(A.)* **1891**, *182*, 449-518.
27. Jang, D.; Idrobo, J.C.; Laoui, T.; Karnik, R. Water and solute transport governed by tunable pore size distributions in nanoporous graphene membranes. *ACS nano* **2017**, *11*, 10042-10052.
28. Dagan, Z.; Weinbaum, S.; Pfeffer, R. An infinite-series solution for the creeping motion through an orifice of finite length. *Journal of Fluid Mechanics* **1982**, *115*, 505-523.
29. Carslaw H.S, Jaeger J.C. *Conduction of Heat in Solids*, Second Edition, Oxford, 1986
30. Rankin, D.J.; Bocquet, L.; Huang, D.M. Entrance effects in concentration-gradient-driven flow through an ultrathin porous membrane. *The Journal of chemical physics* **2019**, *151*, 044705.
31. Faucher, S.; Aluru, N.; Bazant, M.Z.; Blankschtein, D.; Brozena, A.H.; Cumings, J.; Pedro de Souza, J.; Elimelech, M.; Epsztein, R.; Fourkas, J.T.; Rajan, A.G. Critical knowledge gaps in mass transport through single-digit nanopores: A review and perspective. *The Journal of Physical Chemistry C* **2019**, *123*, 21309-21326.
32. Bauer, H.F. Mass transport in a converging-diverging nozzle. *Wärme-und Stoffübertragung* **1988**, *22*, 201-208.
33. Telles, A.S.; Queiroz, E.M.; Elmôr Filho, G. Solutions of the extended Graetz problem. *International Journal of Heat and Mass Transfer* **2001**, *44*, 471-483.
34. Papoutsakis, E.; Ramkrishna, D.; Lim, H.C. The extended Graetz problem with Dirichlet wall boundary conditions. *Applied Scientific Research* **1980**, *36*, 13-34.
35. Acrivos, A. The extended Graetz problem at low Péclet numbers. *Applied Scientific Research* **1980**, *36*, 35-40.
36. Ebdian, M.A.; Zhang, H.Y. An exact solution of extended Graetz problem with axial heat conduction. *International Journal of Heat and Mass Transfer* **1989**, *32*, 1709-1717.
37. Cotta R.M. *Integral Transforms in Computational Heat and Fluid Flow*, CRC Press, 1993.

38. Sphaier, L.A. Integral transform solution for heat transfer in parallel-plates micro-channels: Combined electroosmotic and pressure driven flows with isothermal walls. *International communications in heat and mass transfer* **2012**, 39, 769-775.
39. Knupp, D.C.; Naveira-Cotta, C.P.; Cotta, R.M. Theoretical analysis of conjugated heat transfer with a single domain formulation and integral transforms. *International communications in heat and mass transfer* **2012**, 39, 355-362.
40. Arfken, G.B.; Weber H.J. *Mathematical Methods for Physicists*, Sixth Edition, Elsevier Academic Press, 2005.
41. Ishigami, M.; Chen, J.H.; Cullen, W.G.; Fuhrer, M.S.; Williams, E.D. Atomic structure of graphene on SiO₂. *Nano letters* **2007**, 7, 1643-1648.
42. White, F.M. *Viscous Fluid Flow*, Third Edition, McGraw-Hill, 2006.
43. Lightfoot, E.N.; Bird R.B.; Stewart W.E. *Transport Phenomena*, Revised 2nd Edition, John Wiley and Sons, 2006.
44. Zawawi, M.H.; Saleha, A.; Salwa, A.; Hassan, N.H.; Zahari, N.M.; Ramli, M.Z.; Muda, Z.C. Fundamentals of computational fluid dynamics (CFD). In *AIP Conference Proceedings* **2018**, 2030, 020252.
45. Anderson, J.D.; Wendt, J. *Computational fluid dynamics*, Vol. 206, p. 332. New York: McGraw-Hill, 1995.
46. Eymard, R.; Gallouët, T.; Herbin, R. Finite volume methods. *Handbook of numerical analysis* **2000**, 7, 713-1018.
47. Bathe, K.J. Finite element method. *Wiley encyclopedia of computer science and engineering* **2007**, 1-12.
48. Matsson, J. *An Introduction to ANSYS Fluent 2020*. SDC Publications. 2020
49. Jasak, H. OpenFOAM: open source CFD in research and industry. *International Journal of Naval Architecture and Ocean Engineering* **2009**, 1, 89-94.
50. Ferziger, J.H.; Peric M. *Computational Methods for Fluid Dynamics*, third, rev. edition, Springer-Verlag, 2002.
51. CFD Direct. *OpenFOAM User Guide: CFD Direct, Architects of OpenFOAM*. 2021. <https://cfdirect.com/openfoam/user-guide>
52. Atwal, H.A.; Wong, A.O.K.; Boutilier, M.S.H. Mass advection-diffusion in creeping flow through an orifice plate. **2021**. Manuscript submitted for publication.

Chapter 6

6 Conclusion and Future Directions

Inherently porous atomically thin materials promise similar advantages to graphene as high-performance separation membrane active layers, but without the manufacturing challenge of creating high densities of equally sized pores over large areas. This thesis has furthered inherently porous atomically thin membrane development on multiple fronts. In Chapter 3, CHP monomer was synthesized that will be used in future studies to produce 2D polyphenylene for permeance and selectivity measurements using the tools developed in Chapter 4. The gas separation performance of nanoscopic areas of GDY were measured in Chapter 4 and molecular sieving was demonstrated. The AFM technique developed to measure gas flow rates through flakes of ~nm thickness material is expected to be transferable to other nanomaterials as well. Chapter 5 develops analytical approximations for mass advection-diffusion rates in creeping flow through an orifice plate, of use in atomically thin membrane transport modeling.

6.1 CHP synthesis

In chapter 3, I successfully synthesized cyclohexa-m-phenylene (CHP) monomer of 2D polyphenylene (also known as porous graphene). This material will be used in future studies to produce 2D polyphenylene and measure its gas separation performance. The next steps involve cross-linking the monomer by silver-promoted aryl-aryl coupling under ultrahigh vacuum conditions to produce 2D polyphenylene on a silver substrate. A method needs to be developed to allow suspension and easy transfer of the developed 2D material onto a silicon wafer. Next, experimental measurements can be performed using the method developed in Chapter 4. Moreover, an alternative method needs to be sought, which is faster and more straightforward to produce 2D polyphenylene.

6.2 Molecular sieving through GDY

In chapter 4, I obtained permeance and selectivity data for a centimetre-scale GDY membrane. The permeance values were 7.18×10^{-8} mol/m²-s-Pa, 1.67×10^{-8} mol/m²-s-Pa, 1.61×10^{-8} mol/m²-s-Pa, 2.07×10^{-8} mol/m²-s-Pa, 9.01×10^{-8} mol/m²-s-Pa for

He, CH₄, N₂, Ar and SF₆ respectively. Although no significant improvement in selectivity was observed, these measurements provide a baseline for further efforts to create GDY membrane on larger scales. In particular, gaps and defects in the GDY coverage will need to be sealed to prevent non-selective leakage flow from dominating membrane performance.

The major contribution of this chapter was the development of a measurement setup that permit measuring selective transport of gases through GDY. Prior studies have measured graphene permeance in this way, but I have extended the technique to measure inherently porous materials. It allowed us to measure the gas flow rates passing through a single flake of GDY. In the measurement setup, a single-GDY flake sits on five-layered graphene with a 10 nm hole on a 5 μm cavity in the silicon wafer. Flow through GDY can be measured by charging the cavity with gas and monitoring the rate at which the graphene deflates on an AFM. I obtained deflation data for air, nitrogen, sulfur hexafluoride, and methane, which showed molecular sieving with GDY membranes at 20 kPa and under ambient conditions. The volumetric flow rate of gas exiting the pore D15 was 2.30×10^{-21} mol/s and 7.26×10^{-22} mol/s for N₂ and SF₆ respectively and no inflation was seen for methane. Though, another pore inflated with methane and had a volumetric flow rate of 4.63×10^{-21} μm³/min, it cannot be compared to pore D15. Modest selectivity to N₂ over SF₆ was also measured. The measurement technique could be further modified to improve our ability to resolve high permeances and characterize the structure being measured. Using a smaller diameter hole in graphene to define the flow area could sufficiently reduce the flow rate of smaller gases, facilitating AFM measurement. This could be done using helium ion beam or electron beam milling. Furthermore, performing the measurements on wells created in transmission electron microscope grids may allow for high resolution imaging of the material after AFM measurements.

6.3 Mass advection-diffusion in creeping flow through an orifice plate

In chapter 5, I developed a correlation for simple transport modelling that did not exist before. I used an integral transform approach to precisely calculate mass advection-diffusion rates in creeping flow through an infinitesimally thick orifice plate. By including

only the leading order term in the series expansion, I obtained an analytical expression for this mass transfer rate that is accurate to within 1% for positive Péclet numbers (where advection and diffusion are in the same direction) and maintains low absolute error for negative Péclet numbers (where diffusion is opposite advection). This equation offers an improvement over estimating the mass transfer rate by simply adding the advective and diffusive values as if they were independent, which I found can be in error by up to almost 30% for $Pe > 0$. I presented finite volume calculations for mass advection-diffusion in creeping flow through orifice plates of various aspect ratios and proposed an approximate expression for the mass transfer rate that matches our simulation results to within 3% for positive Péclet numbers. The main outcomes of this chapter are equations that accurately approximate the dependence of Sherwood number on Péclet number for creeping flow through an infinitesimally thick orifice plate and orifice plates of arbitrary aspect ratio. I can further construct approximate transport models using the devised analytical expressions. In addition, the expressions can act as a reference point for examining deviations from continuum solute transport rates in nanopores.

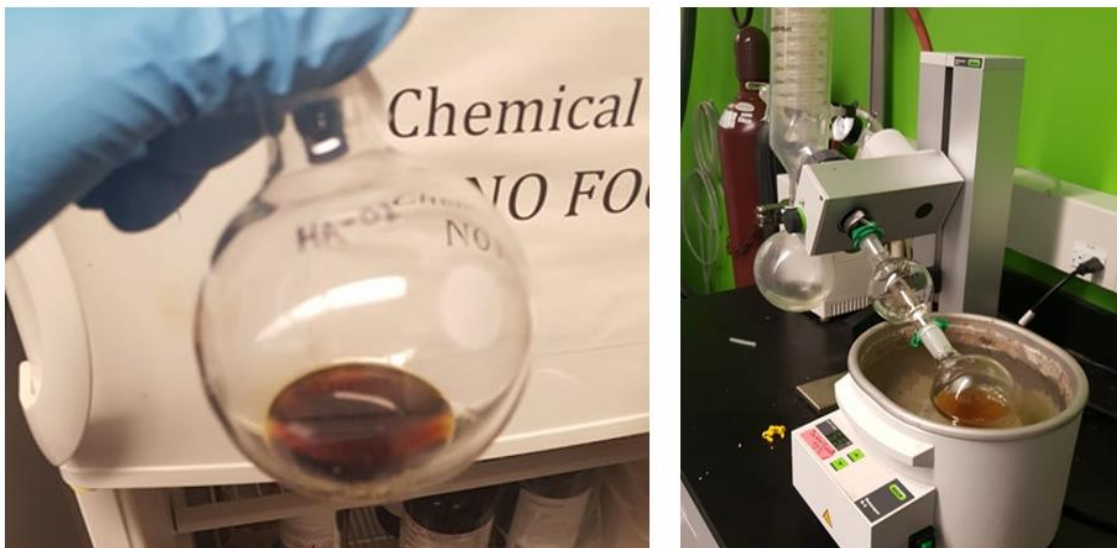
6.4 Closing

Most significantly, in this thesis I have developed an experimental technique with which I can screen inherently porous atomically thin materials for gas separation performance. I have applied this technique to reveal the ability of GDY to separate gas molecule. This project is a major step towards developing selectively permeable, inherently porous, atomically thin membranes for separation applications.

Appendices



Appendix 1: Schlenk line setup for the first reaction.



Appendix 2: (left) Undesired brown oil formation during the first reaction. (right) Rotovap setup.



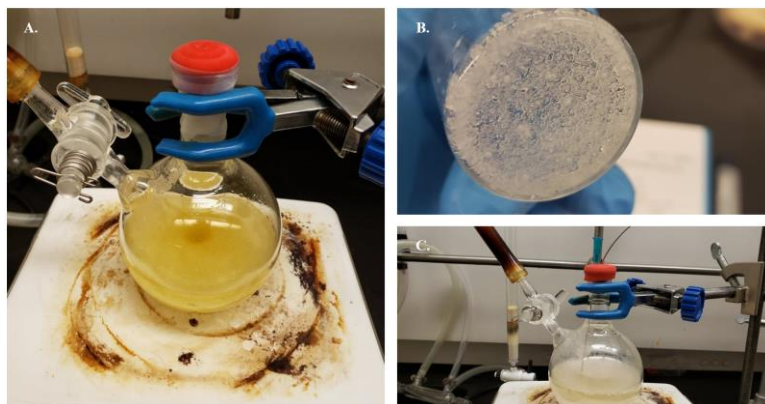
Appendix 3: (left) Separation of impurity from the desired product after 24 hr in the fridge. (middle and right) Desired product **1** with white needle-like crystals.



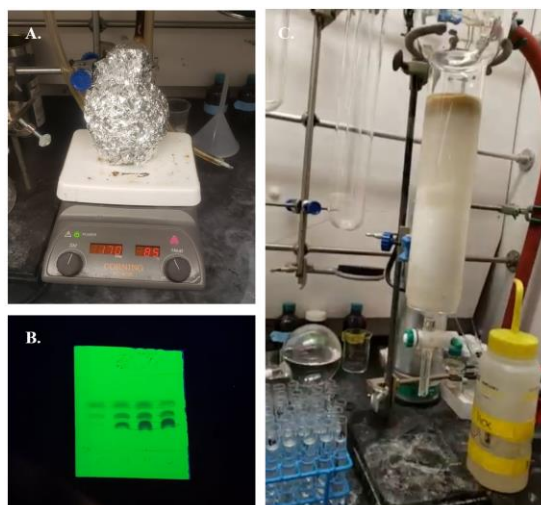
Appendix 4: Desired product **2** (yellow crystalline material) after silica column.



Appendix 5: (left) Synthesis of **3** prior to workup. (right) White amorphous solid **3** after workup.



Appendix 6: **A.** Synthesis of **4** after addition of the Pd catalyst (yellow) **B.** Colorless solid **4** after workup **C.** Degassing setup (bubbling with argon gas) and pressure release via the blue needle



Appendix 7: **A.** Synthesis setup for **5** where aluminum foil ensures absence of light. **B.** Thin Layer Chromatography (TLC) plate of the product showing two additional impurities. **C.** Isolation of the desired product using column chromatography.



Appendix 8: Synthesis setup for **6** in a glove box - covered with black tape to ensure absence of light.

Appendix 9: Copyright Licenses

CCC | Marketplace™

This is a License Agreement between Harpreet Atwal ("User") and Copyright Clearance Center, Inc. ("CCC") on behalf of the Rightsholder identified in the order details below. The license consists of the order details, the CCC Terms and Conditions below, and any Rightsholder Terms and Conditions which are included below. All payments must be made in full to CCC in accordance with the CCC Terms and Conditions below.

Order Date	17-Aug-2021	Type of Use	Republish in a thesis/dissertation
Order License ID	1141286-2	Publisher	RSC Publishing
ISSN	2046-2069	Portion	Chart/graph/table/figure

LICENSED CONTENT

Publication Title	RSC advances	Publication Type	e-Journal
Article Title	Recent developments in polymeric electrospun nanofibrous membranes for seawater desalination	Start Page	37915
Date	01/01/2011	End Page	37938
Language	English	Issue	66
Country	United Kingdom of Great Britain and Northern Ireland	Volume	8
Rightsholder	Royal Society of Chemistry	URL	http://pubs.rsc.org/en/journals/journaliss...

Represents Figure 1.1

8/18/2021

Rightslink® by Copyright Clearance Center



Home

Help ▾

Email Support

Sign in

Create Account

110th Anniversary: Mixed Matrix Membranes with Fillers of Intrinsic Nanopores for Gas Separation



Author: Yanan Wang, Xiaoyao Wang, Jingyuan Guan, et al

Publication: Industrial & Engineering Chemistry Research

Publisher: American Chemical Society

Date: May 1, 2019

Copyright © 2019, American Chemical Society

Represents Figure 1.4

CCC | Marketplace™

This is a License Agreement between Harpreet Atwal ("User") and Copyright Clearance Center, Inc. ("CCC") on behalf of the Rightsholder identified in the order details below. The license consists of the order details, the CCC Terms and Conditions below, and any Rightsholder Terms and Conditions which are included below. All payments must be made in full to CCC in accordance with the CCC Terms and Conditions below.

Order Date	17-Aug-2021	Type of Use	Republish in a thesis/dissertation
Order License ID	1141294-1	Publisher	Royal Society of Chemistry
ISSN	2050-7496	Portion	Chart/graph/table/figure

LICENSED CONTENT

Publication Title	Journal of materials chemistry. A, Materials for energy and sustainability	Publication Type	e-Journal
Article Title	Two-Dimensional Nanosheet-based Gas Separation Membranes	Start Page	23169
Author/Editor	Royal Society of Chemistry (Great Britain)	End Page	23196
Date	01/01/2013	Issue	46
Language	English	Volume	6
Country	United Kingdom of Great Britain and Northern Ireland	URL	http://pubs.rsc.org/en/journals/journaliss...
Rightsholder	Royal Society of Chemistry		

Represents Figure 1.5

This is a License Agreement between Harpreet Atwal ("User") and Copyright Clearance Center, Inc. ("CCC") on behalf of the Rightsholder identified in the order details below. The license consists of the order details, the CCC Terms and Conditions below, and any Rightsholder Terms and Conditions which are included below.

All payments must be made in full to CCC in accordance with the CCC Terms and Conditions below.

Order Date	17-Aug-2021	Type of Use	Republish in a thesis/dissertation
Order License ID	1141296-1	Publisher	Royal Society of Chemistry
ISSN	2050-7496	Portion	Chart/graph/table/figure

LICENSED CONTENT

Publication Title	Journal of materials chemistry. A, Materials for energy and sustainability	Publication Type	e-Journal
Article Title	Two-Dimensional Nanosheet-based Gas Separation Membranes	Start Page	23169
Author/Editor	Royal Society of Chemistry (Great Britain)	End Page	23196
Date	01/01/2013	Issue	46
Language	English	Volume	6
Country	United Kingdom of Great Britain and Northern Ireland	URL	http://pubs.rsc.org/en/journals/journaliss...
Rightsholder	Royal Society of Chemistry		

Represents Figure 1.6

License Details

This Agreement between Ms. Harpreet Atwal ("You") and Elsevier ("Elsevier") consists of your license details and the terms and conditions provided by Elsevier and Copyright Clearance Center.

[Print](#) [Copy](#)

License Number	5135490344271
License date	Aug 24, 2021
Licensed Content Publisher	Elsevier
Licensed Content Publication	Current Opinion in Colloid & Interface Science
Licensed Content Title	Graphene oxide: a surfactant or particle?
Licensed Content Author	Thomas M. McCoy, Geosmin Turpin, Boon Mian Teo, Rico F. Tabor
Licensed Content Date	Feb 1, 2019
Licensed Content Volume	39
Licensed Content Issue	n/a
Licensed Content Pages	12
Type of Use	reuse in a thesis/dissertation
Portion	figures/tables/illustrations
Number of figures/tables/illustrations	1
Format	both print and electronic
Are you the author of this Elsevier article?	No
Will you be translating?	No
Title	Inherently Porous Atomically Thin Membranes for Gas Separation
Institution name	Western University
Expected presentation date	Sep 2021
Portions	Figure 1

Represents Figure 1.7

This is a License Agreement between Harpreet Atwal ("User") and Copyright Clearance Center, Inc. ("CCC") on behalf of the Rightsholder identified in the order details below. The license consists of the order details, the CCC Terms and Conditions below, and any Rightsholder Terms and Conditions which are included below. All payments must be made in full to CCC in accordance with the CCC Terms and Conditions below.

Order Date	17-Aug-2021	Type of Use	Republish in a thesis/dissertation
Order License ID	1141293-1	Publisher	ROYAL SOCIETY OF CHEMISTRY
ISSN	1364-548X	Portion	Chart/graph/table/figure

LICENSED CONTENT

Publication Title	Chemical communications	Rightsholder	Royal Society of Chemistry
Article Title	Porous graphenes: two-dimensional polymer synthesis with atomic precision.	Publication Type	e-Journal
Author/Editor	Royal Society of Chemistry (Great Britain)	Start Page	6919
Date	01/01/1996	Issue	45
Language	English	Volume	0
Country	United Kingdom of Great Britain and Northern Ireland		

Represents Figure 1.8 and Scheme 3

License Details

This Agreement between Ms. Harpreet Atwal ("You") and Springer Nature ("Springer Nature") consists of your license details and the terms and conditions provided by Springer Nature and Copyright Clearance Center.

[Print](#) [Copy](#)

License Number	5131540762061
License date	Aug 17, 2021
Licensed Content Publisher	Springer Nature
Licensed Content Publication	Nature Nanotechnology
Licensed Content Title	Fundamental transport mechanisms, fabrication and potential applications of nanoporous atomically thin membranes
Licensed Content Author	Luda Wang et al
Licensed Content Date	Jun 6, 2017
Type of Use	Thesis/Dissertation
Requestor type	academic/university or research institute
Format	print and electronic
Portion	figures/tables/illustrations
Number of figures/tables/illustrations	2
High-res required	no
Will you be translating?	no
Circulation/distribution	1 - 29
Author of this Springer Nature content	no
Title	Inherently Porous Atomically Thin Membranes for Gas Separation
Institution name	Western University
Expected presentation date	Sep 2021
Portions	Figure 1A, 2D

Represents Figure 1.10 and 1.11

License Details

This Agreement between Ms. Harpreet Atwal ("You") and Elsevier ("Elsevier") consists of your license details and the terms and conditions provided by Elsevier and Copyright Clearance Center.

[Print](#) [Copy](#)

License Number	5134840180506
License date	Aug 23, 2021
Licensed Content Publisher	Elsevier
Licensed Content Publication	Elsevier Books
Licensed Content Title	Encyclopedia of Spectroscopy and Spectrometry
Licensed Content Author	Allan Maccoll†
Licensed Content Date	Jan 1, 1999
Licensed Content Pages	8
Type of Use	reuse in a thesis/dissertation
Portion	figures/tables/illustrations
Number of figures/tables/illustrations	1
Format	electronic
Are you the author of this Elsevier chapter?	No
Will you be translating?	No
Title	Inherently Porous Atomically Thin Membranes for Gas Separation
Institution name	Western University
Expected presentation date	Sep 2021
Portions	Figure 7

Represents Figure 2.3



This is a License Agreement between Harpreet Atwal ("User") and Copyright Clearance Center, Inc. ("CCC") on behalf of the Rightsholder identified in the order details below. The license consists of the order details, the CCC Terms and Conditions below, and any Rightsholder Terms and Conditions which are included below. All payments must be made in full to CCC in accordance with the CCC Terms and Conditions below.

Order Date	23-Aug-2021	Type of Use	Republish in a thesis/dissertation
Order License ID	1142390-1	Publisher	ROYAL SOCIETY OF CHEMISTRY
ISSN	1466-8033	Portion	Chart/graph/table/figure

LICENSED CONTENT

Publication Title	CrystEngComm	Publication Type	e-Journal
Article Title	Porous aromatic frameworks: Synthesis, structure and functions	Start Page	17
Author/Editor	Royal Society of Chemistry (Great Britain)	End Page	26
Date	01/01/1999	Issue	1
Language	English	Volume	15
Country	United Kingdom of Great Britain and Northern Ireland	URL	http://www.rsc.org/Publishing/Journals/c...
Rightsholder	Royal Society of Chemistry		

Represents Figure 3.6A

License Details

This Agreement between Ms. Harpreet Atwal ("You") and Elsevier ("Elsevier") consists of your license details and the terms and conditions provided by Elsevier and Copyright Clearance Center.

[Print](#) [Copy](#)

License Number	5134631223399
License date	Aug 23, 2021
Licensed Content Publisher	Elsevier
Licensed Content Publication	Journal of Organometallic Chemistry
Licensed Content Title	Mechanism of C-C coupling reactions of aromatic halides, promoted by Ni(COD) ₂ in the presence of 2,2'-bipyridine and PPh ₃ , to give biaryls
Licensed Content Author	Takakazu Yamamoto, Shoichiro Wakabayashi, Kohtaro Osakada
Licensed Content Date	Apr 28, 1992
Licensed Content Volume	428
Licensed Content Issue	1-2
Licensed Content Pages	15
Type of Use	reuse in a thesis/dissertation
Portion	figures/tables/illustrations
Number of figures/tables/illustrations	1
Format	both print and electronic
Are you the author of this Elsevier article?	No
Will you be translating?	No
Title	Inherently Porous Atomically Thin Membranes for Gas Separation
Institution name	Western University
Expected presentation date	Sep 2021
Portions	Scheme 1

Represents Figure 3.6B

License Details

This Agreement between Ms. Harpreet Atwal ("You") and Elsevier ("Elsevier") consists of your license details and the terms and conditions provided by Elsevier and Copyright Clearance Center.

[Print](#) [Copy](#)

License Number	5131530444716
License date	Aug 17, 2021
Licensed Content Publisher	Elsevier
Licensed Content Publication	Elsevier Books
Licensed Content Title	Engineered Biomimicry
Licensed Content Author	Raúl J. Martín-Palma, Akhlesh Lakhtakia
Licensed Content Date	Jan 1, 2013
Licensed Content Pages	16
Type of Use	reuse in a thesis/dissertation
Portion	figures/tables/illustrations
Number of figures/tables/illustrations	1
Format	both print and electronic
Are you the author of this Elsevier chapter?	No
Will you be translating?	No
Title	Inherently Porous Atomically Thin Membranes for Gas Separation
Institution name	Western University
Expected presentation date	Sep 2021
Portions	Figure 15.1

Represents Figure 3.12

8/17/2021

Rightslink® by Copyright Clearance Center



Home

Help ▾

Live Chat

Harpreet Atwal ▾

**Two-Dimensional Polyphenylene Networks with Tunable Micropores for Hydrogen Storage**

Author: Chong Xu, Zhen Xu, Qingqing Lu, et al

Publication: ACS Sustainable Chemistry & Engineering

Publisher: American Chemical Society

Date: Nov 1, 2019

Copyright © 2019, American Chemical Society

Represents Figure 3.13

From graphyne to cata-condensed (Acenographynes) and peri-condensed PAHs-graphyne derivatives

Author: Franco Cataldo, , et al

Publication: Fullerenes, Nanotubes, & Carbon Nanostructures



Publisher: Taylor & Francis

Date: Sep 2, 2018

Rights managed by Taylor & Francis

Thesis/Dissertation Reuse Request

Taylor & Francis is pleased to offer reuses of its content for a thesis or dissertation free of charge contingent on resubmission of permission request if work is published.

BACK

CLOSE

Represents Figure 4.2

Curriculum Vitae

Name: Harpreet Atwal

**Post-secondary
Education and
Degrees:** University of Toronto
Mississauga, Ontario, Canada
2015-2019 BSc. in Chemistry.

The University of Western Ontario
London, Ontario, Canada
2019-2021 MEng. in Chemical and Biochemical Engineering.

**Related Work
Experience** Teaching Assistant
The University of Western Ontario
Jan 2020 – Dec 2020

Publications:

Atwal, Harpreet K.; Wong, Anika O.K.; Boutilier, Michael S.H. 2021. Mass advection-diffusion in creeping flow through an orifice plate. Manuscript submitted for publication.